

**Direct laser bonding of transparent materials
using ultrashort laser pulses
at high repetition rates**

Dissertation

zur Erlangung des akademischen Grades
doctor rerum naturalium (Dr. rer. nat.)

vorgelegt dem Rat der Physikalisch-Astronomischen Fakultät
der Friedrich-Schiller-Universität Jena

von Dipl.-Phys. Sören Richter,
geboren am 25.01.1983 in Magdeburg

1. Gutachter: Prof. Dr. Andreas Tünnermann, Jena
2. Gutachter: Prof. Dr. Hartmut Bartelt, Jena
3. Gutachter: Prof. Dr. Réal Vallée, Laval (Kanada)

Tag der Disputation: 06. März 2014

Contents

1	Introduction	1
2	Current State of Knowledge	5
2.1	Glass: Fundamentals and properties	5
2.2	Absorption of ultrashort laser pulses	7
2.3	Laser induced modifications	8
2.3.1	Isotropic refractive index change	10
2.3.2	Birefringent refractive index modification	10
2.3.3	Void formation	11
2.4	Laser induced structural changes	12
2.5	Heat accumulation effects	13
2.6	Common bonding techniques	15
3	Laser induced temperature distribution	17
3.1	Simulation of the heat accumulation and temperature distribution	17
3.1.1	Spherical heat diffusion	19
3.1.2	Cylindrical heat diffusion	21
3.2	Direct Temperature measurement	25
3.2.1	<i>In situ</i> Raman temperature measurement	26
3.2.2	Background signal	29
3.2.3	Heat accumulation of various glasses	32
3.2.4	Spatial and temporal temperature distribution	33
4	Direct Laser Bonding - Fundamentals	41
4.1	Processing window for laser bonding	41
4.2	Absorption of successive ultrashort laser pulses	44
4.3	Laser induced structural changes	48

4.4	Laser induced disruptions	51
4.4.1	Shape and inner structure of laser induced disruptions	51
4.4.2	Model of disruption formation	54
4.4.3	Simulation of beam propagation inside molten fused silica	55
4.4.4	Periodic formation of disruptions	59
4.5	Laser induced stress	61
5	Direct Laser Bonding of fused silica	65
5.1	Experimental approach	65
5.2	Measurement of bonding strength	67
5.3	Laser Bonding of fused silica	69
5.4	Tailored energy deposition	71
5.5	Annealing	76
5.6	Chevron Notch Test	77
6	Bonding of different materials	81
6.1	Homogeneous glass combinations	81
6.1.1	Borofloat 33	81
6.1.2	BK7	82
6.1.3	ULE	83
6.1.4	Zerodur	85
6.2	Bonding of dissimilar glasses	85
6.2.1	Structural analysis	88
6.2.2	Annealing	90
6.3	Bonding of opaque materials	91
6.4	Application examples	93
7	Conclusion and Outlook	97
	References	115
	Acknowledgements	116
	Ehrenwörtliche Erklärung	118
	Lebenslauf	119

1 Introduction

Transparent materials surround us everywhere in our daily life. Especially glass has a dominant role due to its excellent optical, mechanical and chemical properties. For the processing of glass numerous techniques are well known, some of them are more than several hundred years old. In contrast, the reliable and stable bonding of two different glasses is still a demanding problem. Most of the developed glass bonding techniques are adapted from well known silicon waver techniques [1, 2]. All the established methods e.g. optical contacting, direct bonding or anodic bonding exhibit certain disadvantages as these methods were not designed for the bonding of glasses [3, 4]. For example, optical contacting - were two ultraclean glass samples are pressed together and adhere due to the van der Waals forces between their surface atoms - yields only weak bonds.

Alternatively, laser pulses can be used to weld the glass samples together. Commonly high average power cw-lasers are used for laser welding. However for the absorption of cw-laser radiation an opaque material is required. Alternatively, ultrashort laser pulses have proven to be a powerful tool for the processing of transparent materials within the last two decades. The extremely short pulse duration allow nonlinear processes that fundamentally differ from traditional light-matter interaction mechanisms. Nonlinear absorption induced by ultrashort pulses leads to an extremely non-equilibrium state in a confined volume resulting in a variety of different material modifications [5, 6]. Due to the highly localized energy deposition machining of sub micron features and full three dimensional processing of transparent materials become feasible [5, 7]. In fused silica three different types of modifications can be induced: isotropic and anisotropic index changes [5, 6, 8, 9, 10] and the generation of small cavities [11, 12]. Promising applications include the realization of photonic circuits [13, 14, 15, 16], birefringent elements [17, 18], microfluidic channels [19] or data storage devices [20].

In addition, numerous ultrashort laser pulses with a short temporal distance yield the possibility to locally melt the processed material [21], where the laser pulses act as a thermal point source increasing the temperature of the irradiated volume stepwise. Due to heat dif-

fusion also the temperature of the surrounding material is increased leading to the melting of the focal region and a well-defined vicinity [22]. This so-called heat accumulation of ultrashort laser pulses provides thus a powerful tool to locally bond transparent materials. Although the first reports about locally induced heat accumulation and melting of transparent materials are published almost one decade ago [21, 23, 24], there are still demanding issues. While the theoretical background about the stepwise increased temperature and the subsequent heat diffusion is established [25], the real temperature distribution within the modified area is still unknown. Most of the simulations assume constant material parameters leading to temperatures of more than 20000 K in the focal center. In addition, the existing experimental data show only partial results of the induced temperature distribution and are difficult to interpret [26, 27].

Another issue implies the interaction of numerous successive pulses and the extremely hot material exhibiting material properties which differ from the surrounding material. The occurring phenomena - e.g. dark spots within the traces of molten fused silica or the absorption mechanisms - are not fully understood and require further investigation.

For the measurement of the stability of the laser bonded samples different tests have been invented from blade tests [28], shear or tensile tests [29, 30, 31, 32]. All these tests yield certain results about different materials properties whereas a comparison between the results and especially to the values of the pristine bulk material ranges from difficult to impossible [33]. In addition, previous works investigate mainly the bonding of two identical glasses preferring samples with low softening points [31, 34]. Thus, all the capabilities of ultrashort pulse induced laser bonding are far from entirely explored.

The goal of this thesis is the investigation of the interaction processes between multiple laser pulses and the transparent material during the laser welding. In addition, the bonding process itself is characterized in order to achieve strong bonds in different glasses and even in different material combinations.

Structure of this Thesis

This work is divided into seven chapters. After this brief introduction the present state of knowledge about ultrashort pulse induced processing of transparent materials is presented in Chapter 2.

In the subsequent Chapter 3 the laser induced temporal and spatial temperature distribution is investigated. At first, a theoretical model is developed to calculate the size of the laser modified area. Afterwards, an *in-situ* micro Raman setup is presented allowing the direct measurement of the induced temperature distribution during the laser processing. Chapter 4 presents the optimal processing parameters for laser bonding. Furthermore, additional modifications which accompany the bonding process as structural changes of the glass network or laser induced stress are investigated. Great attention was paid to the formation mechanism of laser induced disruptions - which appear within the traces of the molten fused silica - as only a few reports mention these modifications so far and no reliable explanation for their formation exists.

The laser bonding of fused silica is described in detail in Chapter 5. Two different approaches are shown to measure the laser induced bonding strength and compare these results with unmodified bulk material. Beside the geometry of the laser inscribed bonds especially the temporal deposition of laser pulses can be changed to increase the breaking strength of the bonded material. In addition, thermal annealing results are presented exhibiting a possibility to reduce the amount of induced stress.

The results for the bonding of different glasses, glass combinations and even bonding of opaque materials to glass are given in Chapter 6. In this chapter, Raman measurements are conducted to highlight the induced network rearrangements and the generation of strong bonds between the initially separated materials. Last but not least, some potential applications are briefly explained.

Finally, the conclusion of this thesis and an outlook to possible future developments in the field of direct laser bonding are presented in Chapter 7.

2 Current State of Knowledge

2.1 Glass: Fundamentals and properties

Glass is an amorphous solid material without a long range order. The most widely used glasses are silica based. The pure silica glass is known as fused silica consisting of a network of undistorted and relatively rigid SiO_4 tetraeder [35]. These tetraeder are connected at their corners by bridging oxygen atoms. Thus, usually each silicon is surrounded by 4 oxygen atoms and each oxygen is connected with two silicon atoms. The tetrahedral arrangement is the reason for the extraordinary stability of fused silica [36]. The crystalline structure of silicon oxide is named Quartz, being a regular trigonal crystal with a 6- fold ring structure, as shown in Figure 2.1 (a). In contrast, the atoms within the network struc-

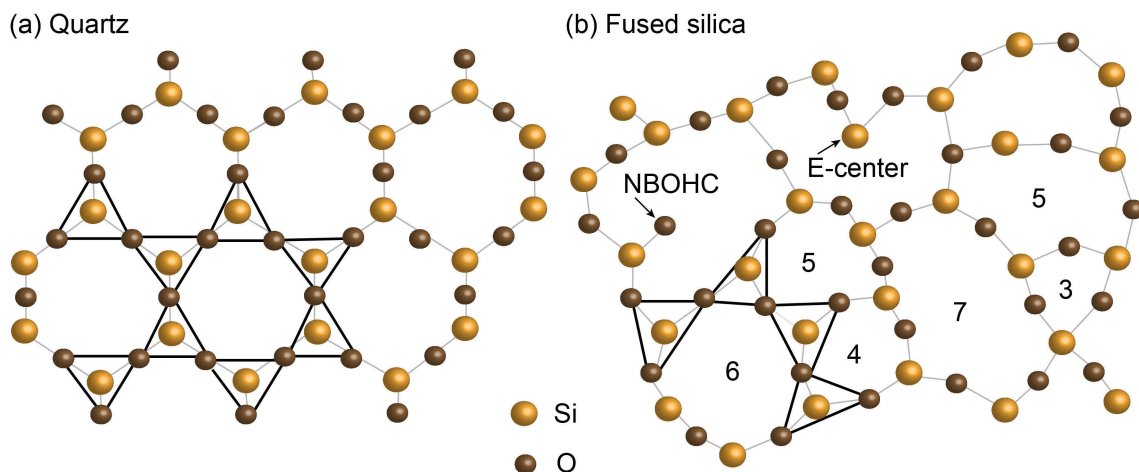


Fig. 2.1: Schematic presentation of the regular, crystalline structure of quartz (a) and the irregular network structure of fused silica (b). The coordination number of silicon atoms in fused silica is written in the network ring. Dangling bonds type defects (dangling Si-bond: E' center and dangling O-bond: NBOHC) are also inscribed. Only three of the four oxygen atoms of each SiO_4 tetraeder are shown. The fourth oxygen atom is located perpendicular to the plane of projection.

ture of fused silica are randomly arranged, predominantly coordinated into 5- and 6- fold ring structures, but also smaller and even larger rings exist [37, 38]. Figure 2.1 (b) shows a scheme of the network structure of fused silica. The valence of the different ring structures is indicated by numbers. Only three of the four oxygen atoms of each SiO_4 tetraeder are shown. The fourth oxygen atom is located perpendicular to the plane of projection. One very well known group of defects are the dangling bond type defects (also shown in Figure 2.1). Dangling Si bonds ($\equiv\text{Si}\cdot$), are called E'-center, whereas an oxygen dangling bond ($\equiv\text{Si}-\text{O}\cdot$) is called NBOHC (non bridging oxygen hole center) [35, 39, 40].

The second fundamental aspect of glasses is their time-dependent glass transformation behavior [41]. Glasses are traditionally formed by cooling of a melt. The important factor for the production of glass is to avoid crystallization and crystal growth, which is normally achieved by a relative high cooling rate. During the cooling the liquid can be cooled below the melting temperature without crystallization and becomes a supercooled liquid. The enthalpy (or volume) of the system decreases continuously without any abrupt decrease, in contrast to a crystalline material. Simultaneously the viscosity increases and eventually hinders the rearrangement of the atoms into the equilibrium liquid structure. Thus, the enthalpy of the system deviates from the equilibrium line of a liquid evolving into the enthalpy of the final glass. The temperature region between the equilibrium liquid state and the frozen solid (glass state) is called the glass transformation region. The fictive temperature is defined as the temperature, at which the glass and supercooled liquid line intersect [41]. With other words, the final structure of the glass is considered to be the frozen structure of the equilibrium liquid at the fictive temperature [38, 42].

The temperature at which the enthalpy departs from the equilibrium state is controlled by kinetic factors such as the cooling rate. Thus, rapidly cooled glass exhibits a higher fictive temperature than slowly cooled glass. Consequently, glasses with different fictive temperatures also exhibit different network structures. For instance, the number of 3- and 4- fold rings increases with increasing fictive temperature [43, 44], which can be investigated with Raman spectroscopy [45].

By adding network modifiers (e.g. K, Na, Ba) into the melt the glass structure gets more complex as these atoms disturb the initial SiO_4 tetraeder resulting in different material properties, as a reduced viscosity or softening point. For instance, the structure of borosilicate glasses (e. g. Borofloat 33 or BK7) is similar to fused silica, with boron atoms replacing some silicon. In this work, a variety of silica glasses was investigated. Some of their important material properties are listed in Table 2.1. The annealing temperature and

softening temperature of a glass is defined over the viscosity of the glass, e.g. the viscosity at the softening temperature is $10^{7.6}$ Pa · s whereas the viscosity at the annealing temperature is 10^{12} Pa · s. Zerodur and ULE™ are so-called low expansion glasses, exhibiting a thermal expansion coefficient close to zero over a distinctive temperature range. Zerodur is a glass ceramic with a crystalline phase (crystal size about 50 nm) and a large content of Al_2O_3 , Li_2O , P_2O_5 and TiO_2 [46]. The Ultra Low Expansion (ULE™) glass from Corning is a titanium silicate glass with about 7.5 % TiO_2 [47, 48].

Tab. 2.1: Thermal and mechanical material properties of different glasses for room temperature [47, 49].

	Fused silica	Borofloat 33	BK7	ULE	Zerodur
thermal exp. coeff. α [10^{-6} K $^{-1}$]	0.5	3.25	7.1	≤ 0.001	≤ 0.1
thermal conductivity κ [W/(m·K)]	1.31	1.2	1.114	1.31	1.46
mean specific heat c_p [J/(g·K)]	0.79	0.83	0.86	0.77	0.82
annealing temperature T_A [°C]	1080	560	557	1000	970
softening temperature T_S [°C]	1600	820	719	1490	≈ 1000
density ρ [g/cm 3]	2.2	2.2	2.51	2.21	2.53
Young's modulus E [GPa]	72	64	82	67	90

2.2 Absorption of ultrashort laser pulses

The density of free electrons in the conduction band of glasses at room temperature is mainly induced by defects and thus rather low (about $10^8 - 10^{10}$ cm $^{-3}$) [50]. In comparison, the free electron density of silicon is $\sim 10^{15}$ cm $^{-3}$ and for metals even $\sim 10^{22}$ cm $^{-3}$ [51]. For this reason as well as the large bandgap, the linear absorption of photons in the visible and near infrared spectral range is very weak. However, ultrashort laser pulses with a pulse duration of about 500 fs and a pulse energy of 200 nJ as used within this thesis can be easily focused to intensities of $\geq 10^{13}$ W/cm 2 using objectives with numerical aperture (NA) ≥ 0.1 . These high intensities induce nonlinear absorption processes, which bridge the bandgap and enable the excitation of electrons into the valence band.

There are two relevant mechanisms for the initial generation of free electrons: multiphoton absorption and field ionization [52]. Multiphoton absorption is the simultaneous absorption of multiple photons by one electron. The sum of the photon energy exceeds the band gap and a quasi-free electron, i.e. an electron in the conduction band, is gener-

ated [53, 54]. At field ionization, the strong laser field distorts the Coulomb-potential of the atom and electrons may tunnel through the potential barrier [53, 54]. To distinguish between these two mechanisms the Keldysh parameter is used [55]. In this work, the processing parameters yield a Keldysh parameter of nearly one, indicating an intermediate regime where both processes contribute, as can be seen in Figure 2.2 (a).

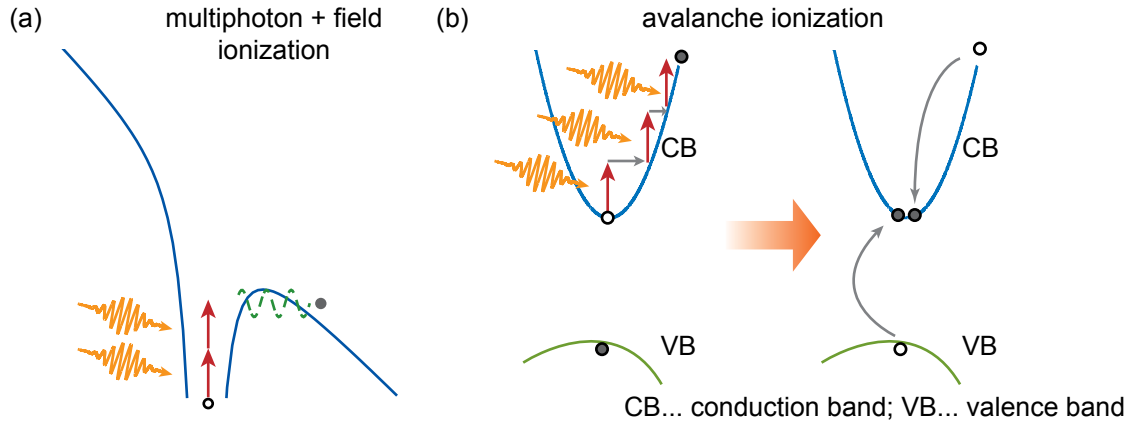


Fig. 2.2: (a) Illustration of simultaneous contribution of multiphoton and field ionization to the generation of a free electron. b) Schematic sketch of avalanche ionization.

In addition, an electron already in the conduction band can sequentially absorb multiple laser photons, finally exhibiting an energy which exceeds the conduction band energy by more than the band gap energy. By impact ionization, an inelastic collision process, an electron of the valence band can be promoted into the conduction band, while the formerly excited electron returns into a lower level of the conduction band. This process results in two excited electrons near the conduction band minimum. Both electrons can repeat this process to form an avalanche of excited electrons [52, 53]. A schematic sketch is shown in Figure 2.2 (b). The contribution of avalanche ionization to the free carrier generation increases with the pulse duration, due to the time required for the collisions [56]. Thus, for longer pulse durations avalanche ionization dominates photoionization and produces a sufficient electron density to cause material modifications [53, 54].

2.3 Laser induced modifications

For illumination with fs-laser pulses, the (nonlinear) absorption occurs on a time scale much shorter than the time required for the energy transfer from the electrons to the

lattice. Thus, electrons in the conduction band are excited by the laser pulse much faster than they relax by electron-phonon scattering, resulting in a non-equilibrium state: excited electrons surrounded by a cold lattice.

The electron density of the excited material grows continuously until its plasma frequency ω_P approaches the laser frequency ω_L [53]. The plasma frequency ω_P is defined as

$$\omega_P = \sqrt{\frac{e^2 N}{\epsilon_0 m_e}}, \quad (2.1)$$

where e denotes the elementary charge, N is the electron density in the conduction band, ϵ_0 is the electric permittivity of free space, and m_e the mass of an electron. It is commonly assumed that a critical density plasma ($\omega_P = \omega_L$, occurring at $N \sim 10^{20} \text{cm}^{-3}$ for a laser wavelength of 515 nm) must be formed to produce material damage [52, 53, 54, 57]. At this point the plasma becomes strongly absorbing, allowing a significant fraction of the laser pulse energy to be deposited into the material. After the absorption, the highly excited electrons thermalize with the ions and induce structural modifications. Depending on the degree of excitation refractive index change, cracking, void formation or localized melting occurs [5, 6, 8]. Although the nonlinear absorption is well understood, the subsequent physical mechanisms for material modifications are still subject of intensive research.

A typical ultrashort pulse writing setup can be seen in Figure 2.3 (a). The laser pulses are

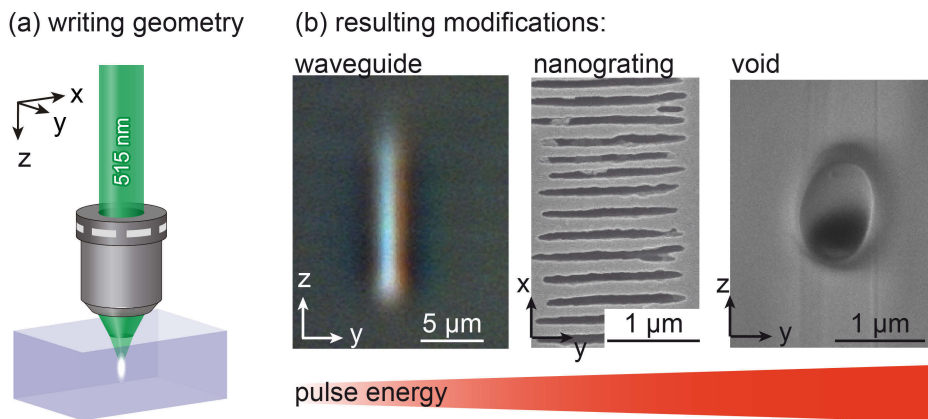


Fig. 2.3: (a) Typical setup to induce modifications in transparent bulk material using ultrashort laser pulses. b) For a certain pulse duration several modifications can be obtained in fused silica. With increasing pulse energy waveguides, nanogratings and voids are formed.

focused via a high NA-objective into the material. Laser parameters, sample properties as well as fabrication techniques define the type of structure modification induced. By translating the sample with respect to the laser focus arbitrary geometries of modifications can be written.

Overall, three different modifications can be distinguished: a smooth and isotropic refractive index change, a birefringent index change and the generation of voids. In fused silica, for a certain pulse duration and focusing condition each of these modifications can be induced, depending on the pulse energy [58]. Figure 2.3 shows typical images of the modifications. In the following, the three different modifications obtained in fused silica are briefly explained.

2.3.1 Isotropic refractive index change

Tightly focused femtosecond laser pulses may induce permanent refractive index changes in glasses [5, 59]. Due to the large temperature difference between the focal volume and the surrounding material, the material cools rapidly after irradiation and the heated glass is quenched at a higher fictive temperature. Depending on the material parameters the refractive index of the processed material can increase or decrease. For fused silica the laser irradiation leads to an increase of the number of the 3- and 4 fold ring structures within the processed material [37, 38, 60]. Consequently, the number of 5- and 6- fold rings decrease, resulting in a decreased overall bond angle of the silicon atoms and a densification of the material yielding an increased refractive index of typically up to 10^{-3} [8, 61, 62, 63, 64]. This so modified material can be used for guiding light [8, 53, 63]. A typical front view of an inscribed waveguide is shown in Figure 2.3 (b). The bright color indicates the guiding region.

2.3.2 Birefringent refractive index modification

With increasing pulse energy the induced modifications become birefringent. Starting in 1999, these previously unknown birefringent modifications in fused silica became the focus of intense research [9, 65, 66, 67]. The origin of this birefringence was revealed by Shimotsuma et al. in 2003 to be a result of laser induced periodic nanostructures. The modified material exhibits an almost periodic density change leading to a modulation of the refractive index and form birefringence [17, 68]. The density change can be made visi-

ble by selective etching with hydrofluoric acid [58, 69, 70]. A top view of such a so-called nanograting is shown in Figure 2.3 (b). The period of these nanogratings scales with the laser wavelength [71, 72] and their orientation is always perpendicular to the polarization of the writing beam.

Different explanations for the formation of nanogratings inside the bulk of fused silica have been proposed [68, 69, 73]. So far, the favored model considers the formation of nanoplanes induced by nanoplasmonic effects. A three-step evolution is predicted: (1) inhomogeneous dielectric breakdown and formation of nanoplasmas, (2) growth of modifications in the material with a size of a few nanometer and evolution to nanoplanes and (3) self organization of these nanoplanes due to their semi-metallic properties and their interaction with the electrical field of the laser pulses [69, 68]. This model predicts a grating pitch of $\lambda/2n$, with the laser wavelength λ and the refractive index n . Also, the grating period should be roughly independent of the pulse energy and duration [58]. However, still there are several problems with this model: First of all, the plasma lifetime in the glass (about 150 fs [74, 75]) is much too short to be responsible for the pulse-wise formation of nanogratings. Furthermore, the self organization into a homogeneous grating is still not understood. Last but not least, it has been observed that the period of the nanogratings scales with the number of irradiated pulses [10, 17, 76], which disagrees to the proposed model. Besides the still unknown formation mechanism, nanogratings might be used for numerous potential applications. Several groups reported on the generation of nanocapillaries, three-dimensional structuring by selective etching and the development of integrated polarization optical and microfluidic devices [17, 73, 77, 78].

2.3.3 Void formation

At extremely high laser intensity the formation of small voids with a diameter of less than a micrometer is possible (see Figure 2.3) [79, 80]. Due to the high electron densities in the focal region, a localized plasma is formed, causing a charge separation [12, 79, 80]. The resulting high pressure causes a so-called microexplosion. The generated shock wave transports energy and matter from the focal region, leading to a compressed surrounding and a focal region devoid of any material [81]. For low pulse energies (several hundred nJ) these voids can be obtained under strong focusing conditions with a high numerical

aperture ($NA \approx 1$) [12, 82]. These voids can be seized and translated [20] or aligned for data storage purposes [79].

2.4 Laser induced structural changes

Pristine amorphous silica has a 3D network of SiO_4 tetrahedra sharing their oxygen atoms and forming Si–O–Si bridges, leading to a well-defined vibrational signature. Strong covalent-bonded structures have Raman signatures that are orders of magnitude larger than those of ionic ones. Thus, the Raman spectrum of a silicate consists basically of the signature of the Si–O network (Si–O stretching, bending and collective modes). Consequently, the different tetrahedral arrangements (different membered ring structures as well as the different number of linkages of a SiO_4 tetrahedra) have characteristic Raman signatures [83, 84].

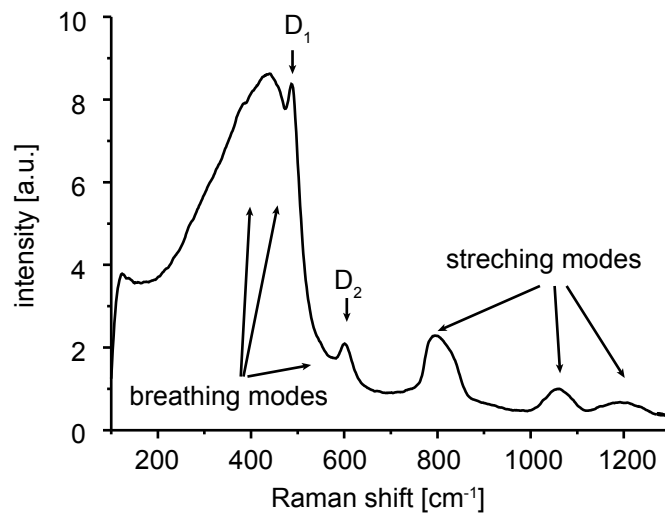


Fig. 2.4: Raman spectra of pristine fused silica

Figure 2.4 shows a typical Raman spectrum of pristine fused silica. The broad band around 440 cm^{-1} is due to the Si–O–Si breathing modes of multiple silica rings. The main peak at 440 cm^{-1} is most likely due to the six-membered rings, while the presence of five-, seven- and even higher member rings broadens this band [85]. The two peaks at 495 cm^{-1} and 605 cm^{-1} are called defects-lines D_1 and D_2 . These lines are associated with breathing modes of four (D_1) and three (D_2) planar silicon-oxygen rings [43]. The peaks starting from 800 cm^{-1} in Figure 2.4 are due to stretching modes of Si–O–Si network. The multiple

peaks are due to the different connection grades of the silicon tetrahedra [84, 83].

Thermal investigations yielded, that the intensity of the defect-lines increase with the fictive temperature of the glass [43]. Chan et al. measured also an increase of the peak intensity of the defects lines after irradiation with ultrashort laser pulses, indicating that laser treatment induces serious network rearrangements and network states connected with higher fictive temperatures [38, 86, 87]. The stretching modes however, showed no significant change of the peak intensity after thermal or laser treatment. In addition, intensive laser irradiation induces multiple defects and vacancies [74, 88]. One very well known group of defects are the dangling bond type defects (also shown in Figure 2.1). To investigate the formation of defects in glasses after the irradiation with ultrashort laser pulses, absorption spectroscopy can be used [35].

2.5 Heat accumulation effects

The time required for the dissipation of the deposited energy out of the focal volume (diffusion time t_D) is given by $t_D = \omega_0^2/2D$, with ω_0 the focal radius and D the diffusivity of the material [89]. The diffusivity is defined as: $D = \kappa/\rho c_p$, with κ the thermal conductivity, c_p the specific heat and ρ the density of the material. For a focusing with a NA of about 0.5 (wavelength of 515 nm), the width of a single pulse modification in fused silica is about 1 μm , resulting in a diffusion time of about 1 μs . If the time between two successive pulses is shorter than this relaxation time, the temperature inside the focal volume is increased stepwise by each pulse. This process is called heat accumulation [21, 22, 30, 52]. Figure 2.5 shows the calculated temperature rise for different repetition rates at a fixed pulse energy of 200 nJ in fused silica in a distance of 2 μm from the focal center (pulse duration 450 fs, NA of 0.5). The model used to calculate the temperatures is explained in Section 3.1.

Directly after the absorption of a laser pulse the temperature rises very fast and cools down until the next pulse arrives. This can be especially seen for repetition rates below 1 MHz. For fused silica, a repetition rate of 100 kHz and 500 kHz is insufficient to induce a temperature rise, exceeding the softening point (dashed line). At 100 kHz almost no heat accumulation is observed, whereas for higher repetition rates the successive laser pulses increase the temperature stepwise. With increasing repetition rate the intermittent cooling period is shortened, consequently the decline of the temperature is less pronounced and

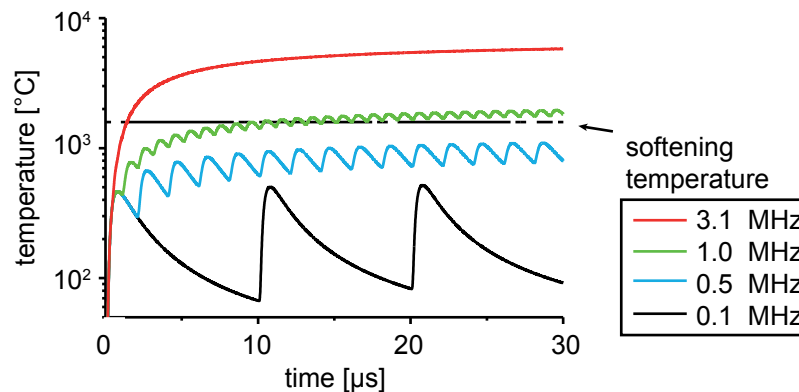


Fig. 2.5: Calculated temperature $2\ \mu\text{m}$ from the focal center due to heat accumulation of successive pulses for different pulse repetition rates (single pulse energy $200\ \text{nJ}$).

higher temperatures are achieved. Eventually the temperature saturates, when the energy transfer from the laser pulses equals the heat diffusion into the surrounding material.

Due to thermal diffusion the molten zone is much larger than the focal volume, leading to a much larger modified volume than for laser machining without heat accumulation [31, 90]. After laser irradiation the molten material cools rapidly, leading to a non-uniform resolidification [91]. This generic prediction can be experimentally verified. Figure 2.6 shows a front view on laser induced modifications in fused silica for different repetition rates. The sample was translated at $20\ \text{mm/min}$, leading to several thousand laser pulses incident per μm . Because of the large heat conductivity of fused silica, heat accumulation sets in at a repetition rate of $1\ \text{MHz}$, using a pulse energy of $120\ \text{nJ}$. For lower repetition rates, no melting occurred outside of the focal volume. The molten volume increases with the repetition rate due to the heat accumulation. For a repetition rate of $9.4\ \text{MHz}$ the modification yields an elliptical shape with a size of about $50\ \mu\text{m}$ times $100\ \mu\text{m}$, i.e. significantly larger than the focal volume.

As heat accumulation leads to the melting of the material, the subsequent resolidification can be used to bond transparent materials [23, 92, 93]. To this end, the laser focus has to be located slightly beneath the interface between two adjacent samples. Here, the laser pulses pose a thermal point source which allows localized heating of the interface, resulting in strong covalent bonds between the samples. This process is called laser bonding or laser welding [92, 93]. Depending on the glass, laser induced melting may reduce the transparency of the processed material. However, as the laser focus can be moved arbitrary, various geometries of molten material can be realized. This is extremely useful

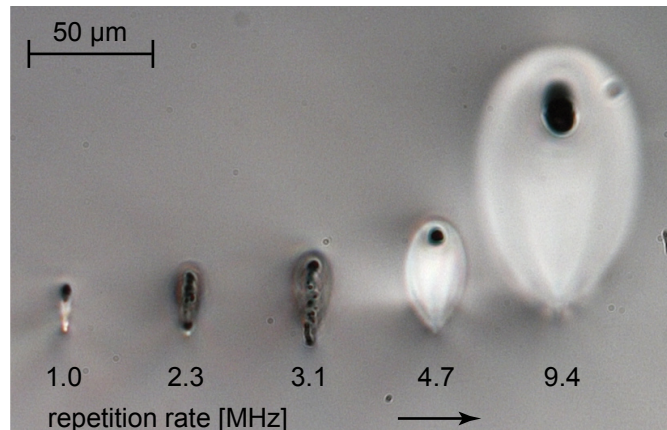


Fig. 2.6: Front view on the laser induced modifications in fused silica for different repetition rates at a pulse energy of 120 nJ (NA 0.5, pulse duration 450 fs) and a translation velocity of 20 mm/min. Focusing depth was 250 μm below the sample surface.

when bonding optical devices (e.g. lenses). Here, only the outer part of the device can be bonded and the inner part remains unmodified. In principle, it is possible to join even dissimilar materials [94, 95]. However, the size and the structure of the laser induced modifications depend on the utilized glass and on the processing parameters, as the thermal properties differ between the glasses (see Table 2.1). Therefore, a detailed analysis of the optimal laser bonding techniques for a variety of parameters and materials is performed in this thesis. Within Chapter 3 simulations as well as experimental results are presented, dealing with the actual temperatures induced during the heat accumulation of successive laser pulses.

2.6 Common bonding techniques

Most of the existing bonding techniques for transparent materials are adapted from well known silicon wafer bonding techniques [1, 2]. The most simplest one is called optical contacting. At this adhesive-free process, two ultraclean and ultraflat samples are pressed together. Afterwards they adhere together due to the van-der-Waals forces of their surface atoms. To this end, the surface roughness has to be below 2 nm rms and a flatness below 125 nm is required [93]. This technique yields only weak bonds (several kPa), which can be strengthened by a subsequent annealing process, producing strong covalent bonds [96, 97]. Alternatively one can use binders or a glass frit to bond two samples together [98,

99]. Unfortunately adhesives tend to aging or gas emission [3, 4, 100]. Techniques as the low pressure plasma surface activation (called Direct Bonding [101]) or anodic bonding requires numerous fabrication steps or even a clean room environment. Therefore, these techniques are time-consuming and expensive, although they yield stable bonds with a stability of about 50 % of the bulk material. With the exception of the adhesive methods, none of the conventional techniques allow the selective bonding of only specific areas of the interface while leaving the remaining area unaffected [102]. In addition, it is possible to melt the interface of the two samples by laser irradiation [30, 34, 103]. To obtain linear absorption directly at the interface an absorbing material or layer is required, reducing the transparency of the sample [104, 105, 106].

Some of these techniques achieve bondings strength of up to 70 % of the bulk material, whereas most of the techniques apply an additional annealing step to achieve these high values. However, annealing induces additional stress in the material, which is especially true for the bonding of dissimilar materials.

In contrast, bonding of transparent materials using ultrashort laser pulses at high repetition rates offer multiple advantages. First of all, it is a very localized bonding process. The laser acts as thermal point source modifying only the material in the vicinity of the laser focus. Thus, the induced stress is reduced. In addition, by using a positioning system arbitrary 3D geometries can be bonded, whereas the rest of the sample remains unattached. In one part of thesis (Chapter 5 and 6) the influence of the processing parameters on the achievable breaking strengths is investigated. Thereby, homogeneous glass combinations as well as different materials can be bonded.

3 Laser induced temperature distribution

This Chapter is dedicated to the calculation and measurement of the temperature distribution induced by the heat accumulation of ultrashort laser pulses. In Section 3.1 a thermal diffusion model is introduced to simulate the heat accumulation and the resulting temperature. In the following the calculation results are compared to experimental results. Section 3.2 presents a method to directly measure the induced temperature distribution using *in-situ* Raman spectroscopy. These results were obtained in collaboration with the group of Prof. K. Itoh at the Graduate School of Engineering of the Osaka University.

3.1 Simulation of the heat accumulation and temperature distribution

To estimate the processing parameters for the bonding of different materials it is important to establish a model of the laser induced temperature distribution. Especially information about the onset of heat accumulation and the expected size of the molten region is required. Such a comprehensive model of the heat distribution is necessary to weld different glasses without an interminable study of the required processing parameter .

For the heat transport, three principal mechanisms can be considered: thermal radiation, heat convection and heat diffusion. Radiative heat transport can be neglected due to the small size of the laser-heated volume [107, 108]. The influence of a thermal shock to the heat transport is only important at very short timescales (≤ 10 ns) as shown by Carr et al. [107] and can thus be neglected where thermal diffusion dominates. In glasses, phase transition from the solid state to the liquid state requires no latent heat and can thus be neglected [109]. In addition, different groups [31, 108] have shown that heat diffusion is sufficient to describe the heat distribution in ultrashort pulse excited glasses. The laser

pulse energy is initially absorbed by electrons, leading to an extremely high electron temperature and a cold lattice [6]. The time for the subsequent electron-phonon coupling is in the ps-range, resulting in an equilibrium state after several tens of ps [6]. Thermal diffusion requires a few μs , see Section 2.5. The time between two laser pulses is determined by the repetition rate of the laser system, which is maximal 9.4 MHz (resulting in a temporal pulse separation of ~ 100 ns) in the present work. As the time required to reach an equilibrium between electrons and lattice is about 4 orders of magnitude shorter than the time between the individual pulses, for the simulation a two temperature model, taking electron as well as lattice temperature into account [110] is not necessary. In addition, for a two temperature model a short temporal step size is required, resulting in a very time consuming and extensive simulation when considering thousands of successive laser pulses. Thus, the model used in this work is based on a simple thermal diffusion model, assuming an excitation of the material with a Gaussian pulse shape [22].

The governing fundamental equation to calculate the temperature distribution is the heat diffusion equation [111, 112]:

$$\rho c_p \frac{\partial T(\vec{r}, t)}{\partial t} = \vec{\nabla} \cdot (\kappa \cdot \vec{\nabla} T(\vec{r}, t)) , \quad (3.1)$$

where $T(\vec{r}, t)$ is the temperature distribution as a function of space and time, κ denotes the thermal conductivity, ρ the material density and c_p the specific heat capacity at constant pressure. Most models consider a constant thermal conductivity [21, 22, 25] and introduce the diffusivity D as:

$$D \equiv \frac{\kappa}{\rho c_p} , \quad (3.2)$$

this simplifies equation (3.1) to

$$\frac{\partial T(\vec{r}, t)}{\partial t} = D \vec{\nabla}^2 T(\vec{r}, t) . \quad (3.3)$$

Our simulations have shown, that for high repetition rates (above 1 MHz) and translation velocities v of a few mm/s the influence of a moving heat source can be neglected, due to the already large number of laser pulses per spot. Thus, a stationary sample is considered, introducing an effective number of laser pulses irradiating the sample: $N_{eff} = 2\omega_0 \cdot R/v$, with ω_0 the focal radius of the laser spot, and R the repetition rate of the laser. To determine the spot size d_s ($d_s = 2\omega_0$), SEM images of laser induced nanogratings are used.

Here, no heat accumulation occurs and the width of a nanograting directly reflects the spot diameter. In accordance to theoretical values the spot size d_S is about $1 \mu\text{m}$. As the pulse duration is much shorter than a time step within the simulation, the thermal excitation with a laser pulse is assumed to be instantaneous and results in a temperature rise of $\Delta T(\vec{r}) = \mathcal{E}(\vec{r})/(\rho c_p)$, with $\mathcal{E}(\vec{r})$ the energy volume density of a laser pulse. Within this thesis, the temperature distribution $T = T(\vec{r}, t)$ was calculated with an explicit finite difference model.

3.1.1 Spherical heat diffusion

After the excitation with a point source the initial deposited energy diffuses according to Equation 3.1. For isotropic media, the resulting temperature distribution is spherical. Thus, thermal diffusion with a spherical symmetry is considered as a first approach. The appropriate thermal diffusion partial differential equation is then:

$$\frac{D}{r^2} \frac{\partial}{\partial r} \left(r^2 \frac{\partial T(r, t)}{\partial r} \right) = \frac{\partial T(r, t)}{\partial t} . \quad (3.4)$$

The energy volume density of a laser pulse is treated as a spherical Gaussian distribution: $\mathcal{E}(r) = E_0 \exp(-r^2/\omega_0^2)$, where the factor E_0 depends on the absorbed laser pulse energy and the size of the absorbing volume [113]. The absorptivity depends strongly on the processing parameters, especially on the laser wavelength. For the simulations an absorptivity of 75 % was used, which fits to the results presented in [25].

Figure 3.1 shows the calculated temperature distribution for a single and 50 successive pulses with a repetition rate of 1 MHz (temporal distance $1 \mu\text{s}$) and pulse energies of 200 nJ. The red dashed line indicates the softening point (1600°C) of fused silica. For both conditions it can be seen that the deposited heat diffuses into the surrounding material. The molten volume (temperature higher than the softening point) exceeds the focal area even for the single pulse excitation. The irradiation with numerous pulses leads to heat accumulation. Thus, the absolute temperatures is increased and an area of almost $5 \mu\text{m}$ in diameter is molten. The temporal decay of the temperature can be seen, too. For the single pulse irradiation the temperature drops within $1 \mu\text{s}$ below 1500°C , whereas for the heat accumulation regime the temperature is still above 3000°C .

The general trend of the heat diffusion calculated by this model in good agreement with experimental results [31, 114]. As shown in Figure 2.6, heat accumulation sets in at a

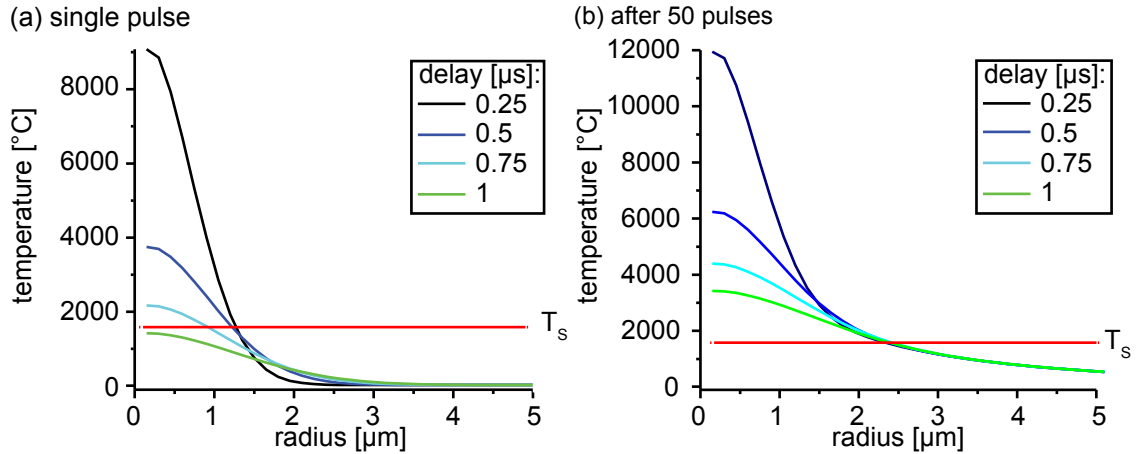


Fig. 3.1: Calculated temperature distribution for different delay times after the irradiation with (a) one single pulse (b) 50 successive pulses (temporal distance 1 μs , pulse energy of 200 nJ and NA of 0.5).

repetition rate of 1 MHz, leading to a molten volume, which exceeds the focal volume. However, the absolute temperatures close to the center are questionable. A temperature of about 12000 °C 250 ns after the last excitation [dark line in Figure 3.1 (b)] is very high and presumably not very reliable. For this model the temperature dependence of the material parameters were neglected. Thus, the real temperature is expected to be much lower than the simulations, as will be shown in Section 3.2.

Nevertheless, these simulations can be used to estimate the onset of heat accumulation for different processing and especially material parameters. Here, the absolute temperatures close to the center are not interesting. Instead of that, the temperature outside of the focal area (distance of 2 μm from the center) was calculated and it was determined for which processing parameters the softening point is exceeded. Figure 3.2 shows the temporal evolution of the induced temperature for fused silica and borosilicate glass using different repetition rates. The pulse energy was set to 200 nJ. Figure 3.2 (a) was already shown in Section 2.5 to explain the mechanism of heat accumulation. Borosilicate exhibits a lower thermal conductivity and softening point than fused silica, see Table 2.1. Thus, melting can be expected already at a repetition rate of 500 kHz whereas for fused silica a repetition rate of 1 MHz is required to exceed the softening point. This behavior agrees to the results obtained by Eaton et al. [90]. Due to the different material properties, the calculated values of the temperature in borosilicate are slightly higher than in fused silica, e.g. at a repetition rate of 9.4 MHz a temperature of about 15000 °C is reached.

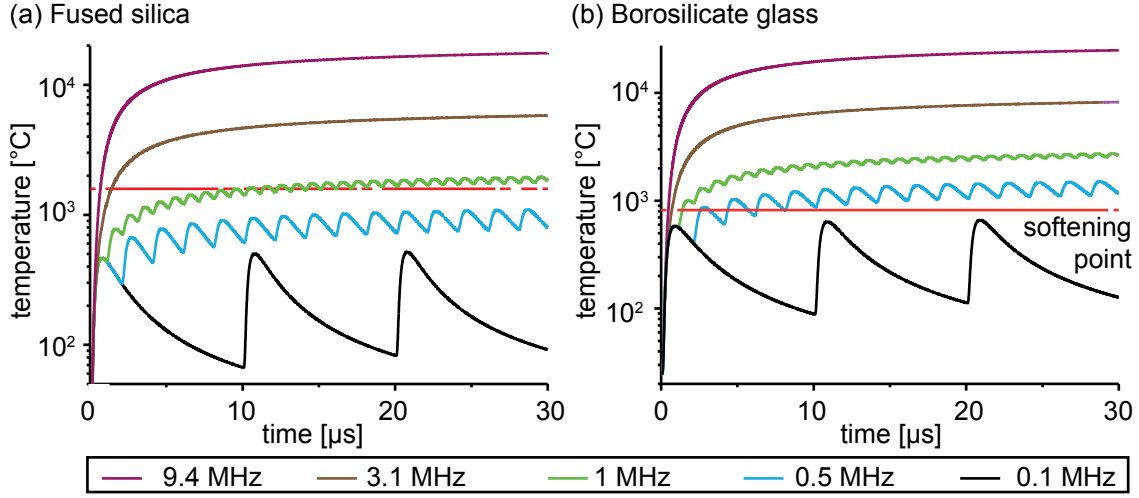


Fig. 3.2: Calculated temporal temperature evolution using different repetition rates for (a) fused silica and (b) borosilicate glass 2 μm from the focal center (pulse energy of 200 nJ and NA of 0.5). The red dashed line indicates the softening points of the glasses.

3.1.2 Cylindrical heat diffusion

Besides the information about the required processing parameters to induce heat accumulation a prediction of the size of the molten area is important. The actual geometry of ultrashort pulse induced molten material exhibits an elliptical shape extended along the optical axis, as shown in Figure 2.6 [31, 90, 93]. The extension along the optical axis has primarily two reasons: an upward shift of the absorption point due to the generation of free electrons and the focusing deep into the glass resulting in an elongation of the laser focus due to aberrations. Taking the asymmetry into account, the temperature diffusion model has to be expanded into a two-dimensional model with cylindric coordinates: $T = T(r, z)$ with $r = \sqrt{x^2 + y^2}$. The resulting heat diffusion equation is:

$$\frac{1}{D} \frac{\partial T(r, z, t)}{\partial t} = \left\{ \frac{1}{r} \frac{\partial}{\partial r} \left(r \frac{\partial}{\partial r} \right) + \frac{\partial^2}{\partial z^2} \right\} T(r, z, t) \quad (3.5)$$

The simplest way to account for an elongated shape of the induced modification is the assumption of a rectangular heat source, as it was shown by Miyamoto et al. [25, 31, 115]. The aspect ratio of their heat source depends on the processing parameters [25]. A more sophisticated approach is the approximation of a Gaussian heat source with constant width (ω_0) along the radial axis and a Lorentzian distribution along the beam propagation:

$$\mathcal{E}(r, z) = \frac{E_0}{1 + \left(\frac{z}{z_R}\right)^2} \exp\left(-\left(\frac{r}{\omega_0}\right)^2\right) \quad (3.6)$$

where z_R denotes the Rayleigh length of the focused pulse. Figure 3.3 shows the calculated temperature distribution for an irradiation with a single pulse (a) and with 50 pulses (b) at a repetition rate of 1 MHz. Here, a snapshot of the temperature evolution is given for 1 μ s after the last pulse has irradiated the sample. The elongation along the optical axis (z-axis) can be seen for both cases. As it was already shown for the 1-D calculation the heat accumulation of 50 pulses leads to much higher temperatures than the irradiation with just a single pulse. The maximal temperature for the single pulse irradiation is about 5000 K whereas after the irradiation with 50 pulses a maximal temperature of 15000 K is obtained. Consequently, the heat affected zone in both cases varies resulting in a different size of the molten area.

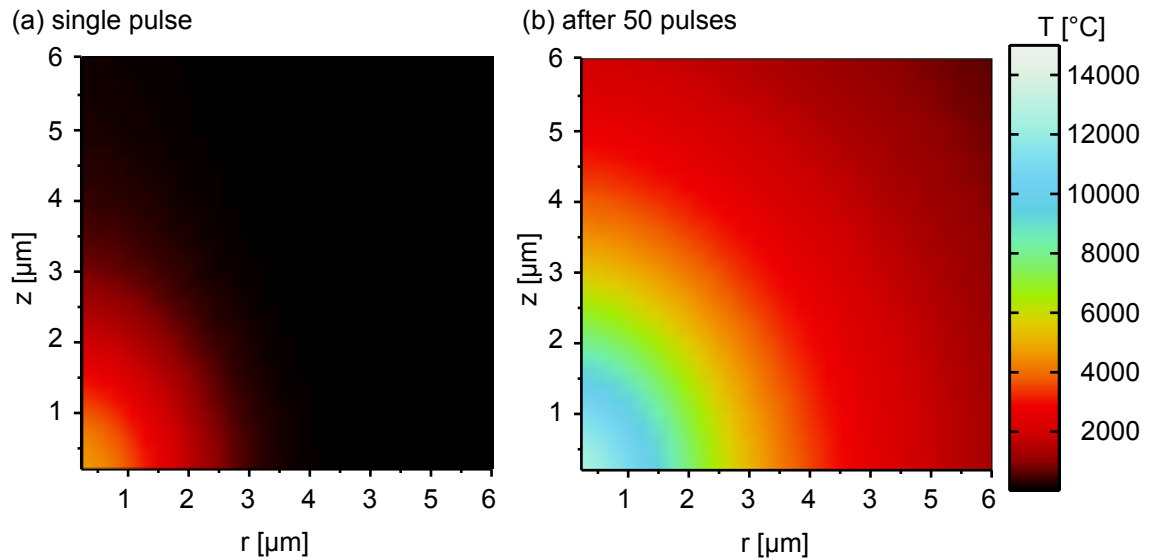


Fig. 3.3: Calculated temperature distribution in fused silica 1 μ s after the irradiation with (a) 1 pulse and (b) 50 pulses at a repetition rate of 1 MHz. Pulse energy is 200 nJ and NA 0.5.

These calculations can be used to determine the size of the molten material when considering the region where the local temperature exceeds the softening point of the material. However, this approach yields much smaller values than the actual experimental results especially for high applied laser powers, as can be seen in Figure 3.4.

Here, repetition rates of 4.7 MHz and 9.4 MHz were considered. The pulse energy was 100 nJ. The large deviation of the calculation from the experimental results is due to the

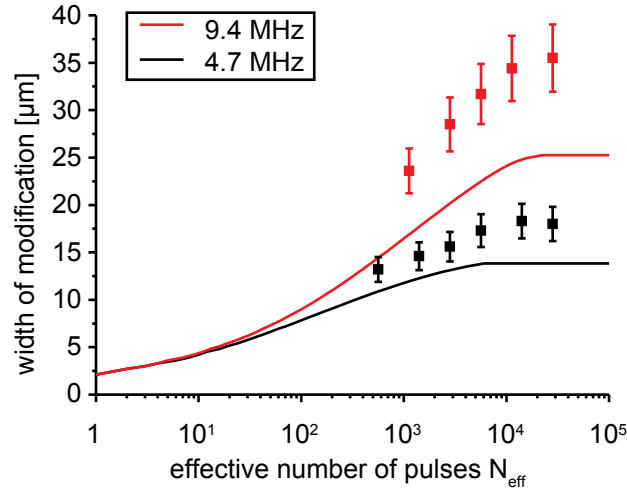


Fig. 3.4: Simulation of the width of the molten material, assuming a constant diffusivity (continuous lines) and experimental results (points) in fused silica. Pulse energy was 100 nJ and NA 0.5.

simplification that material parameters as the thermal conductivity are independent of the temperature [21]. However, it is known that the thermal conductivity decreases with increasing temperatures [51]. For temperatures above the Debye temperature the number of phonons is proportional to the temperature. With increasing temperature, phonon scattering increases, reducing the thermal conductivity [21]. The lower conductivity results in an increased temperature within the modified volume and a larger actual molten volume. The dependence of the thermal conductivity on the temperature can be expressed as [51, 116]:

$$\kappa(T) = \frac{1}{1/\kappa_0 + bT} \quad (3.7)$$

where κ_0 is the thermal conductivity at room temperature. The free parameter b was set to $1.9 \cdot 10^{-6}$ m/W to affect the temperature distribution only at high temperatures, which are reached only for large applied laser powers. This value yields a good accordance between simulations and experimental results. In Figure 3.5 the calculated size of the molten material [(a) width, (b) length] with respect to the number of irradiating laser pulses for different repetition rates can be seen. The points state experimental results which were obtained in a focusing depth of 250 μm inside a fused silica sample. The pulse energy was 100 nJ.

The size of the molten material increases with increasing number of laser pulses and eventually saturates when the heat diffusion balances the energy deposition of the laser

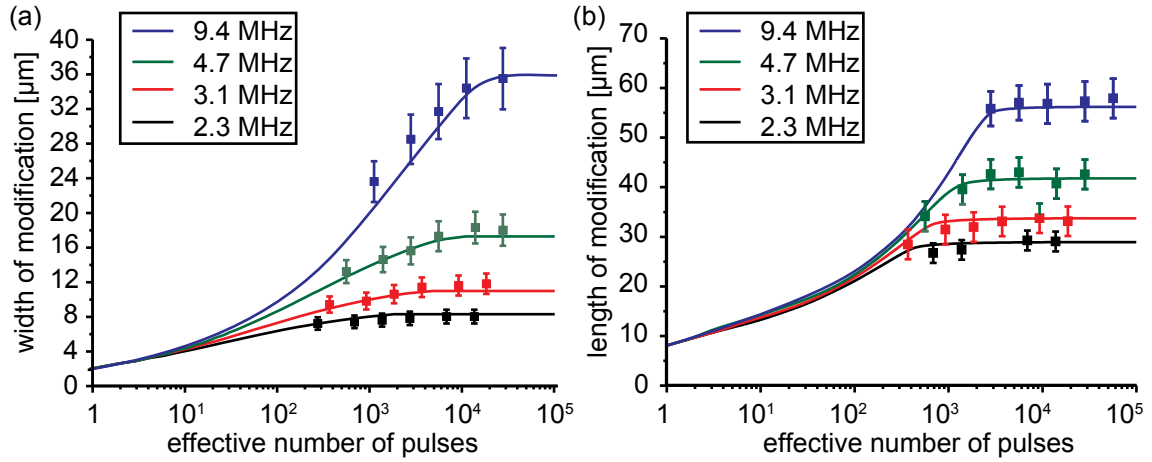


Fig. 3.5: Comparison between simulations (continuous lines) and experimental results (points) in fused silica. (a) Width and (b) length of the molten material. Pulse energy was 100 nJ and NA 0.5.

pulses. The size of the structures increases with the repetition rate due to the larger heat accumulation, when the time between successive laser pulses decreases.

The knowledge about the size of the laser induced molten structure is important for laser welding. For example, the length of the modification determines the tolerable error for the positioning of the focus along the beam propagation direction as the interface of the two adjacent samples has to be molten to bond these samples. It was shown, that the minimal distance between two samples may not exceed 200 nm to facilitate optical contacting [25]. However, it is also possible to bond samples which are not optically contacted over their entire interface [24, 117]. Here, large modifications are favored as more material is molten in order to bridge the gap between the samples. To obtain high breaking strengths, it is important to structure almost the entire interface of the samples. To this end, numerous welding seams have to be placed next to each other, whereas their minimal distance is given by their widths. From an economical point of view it is also reasonable to use high translation velocities to minimize the processing time. For example, at a repetition rate of 4.7 MHz a translation velocity of 200 mm/min (~2800 pulses per spot) yields a melt width of 28 μm. Although slower translation velocities yield larger modifications (up to 36 μm) the benefit in the processing time to structure the entire interface is almost a factor of eight in comparison to a translation velocity of 20 mm/min. As the maximal usable translation velocity is limited by the positioning system, for most of the experiments a translation velocity of 200 mm/min was used.

3.2 Direct Temperature measurement

The simulations of the previous section showed that the softening point of the material can be used to determine the size of the molten structure (see Figure 3.5). The calculated width fits to the experimental result, if one considers a temperature dependent conductivity. However, the calculated absolute temperatures close to the focal point are far too high. For example, temperatures of about 20000 K at a distance of 2 μm from the center were calculated for repetition rates of 9.4 MHz. At shorter distances to the center the calculated temperature is even higher. Several reasons account for these high values: One is the uncertainty of the thermal material coefficients. In addition, the reduction of the viscosity of the material with increasing temperature will facilitate heat convection and enable hydrodynamic processes. Thus, the real temperature will be lower than the simulated one.

To get deeper insight into the real temperature dynamic of ultrashort pulse induced heating of transparent materials additional experiments are required. So far, only a few experiments are reported, which are capable to measure some parts of the temperature distribution [108, 118]. In the transient lens method, the spatial deformation of a probe beam which passes through the laser-induced refractive index change is measured [108]. As a change in temperature causes a refractive index change, the temperature distribution due to thermal diffusion can be detected by this transient lens method. In a zinc borosilicate glass they measured a laser induced temperature rise of 1800 K [108]. Shimizu et al. presented a method to calculate the temperature distribution within a special glass after the laser irradiation by changing the ambient temperature during the laser irradiation [27]. The increase of the width of the molten structure can be used to calculate the spatial temperature distribution. However, this method is limited to some special glasses and yields no information about the temperature dynamics.

Another very promising technique is to use the temperature dependent ratio between Stokes and Anti-Stokes Raman scattering [114]. This method was used to directly measure the spatio-temporal dynamics of heat in fused silica after the excitation with single femtosecond laser pulses [114, 119]. Here, this technique is employed to directly measure the induced temperature distribution after the absorption of multiple ultrashort laser pulses at high repetition rates.

3.2.1 *In situ* Raman temperature measurement

For the *in situ* Raman temperature measurement femtosecond pulses for the processing (processing pulse) and nanosecond pump pulses are spatially and temporally synchronized and focused inside a sample. The nanosecond pulses (Raman pump pulses) are used to generate a Raman signal at the focal spot. The backscattered Raman signal is detected by a time-gated polychromator, consisting of a grating and an intensified charge-coupled (ICCD). In order to map the temporal evolution of the temperature distribution, the Raman pump pulse can be delayed with respect to the processing pulse. Furthermore, the gate of the ICCD is synchronized with the Raman pump pulse allowing the acquisition of time-resolved Raman signals. A sketch of the principle idea is shown in Figure 3.6 (a).

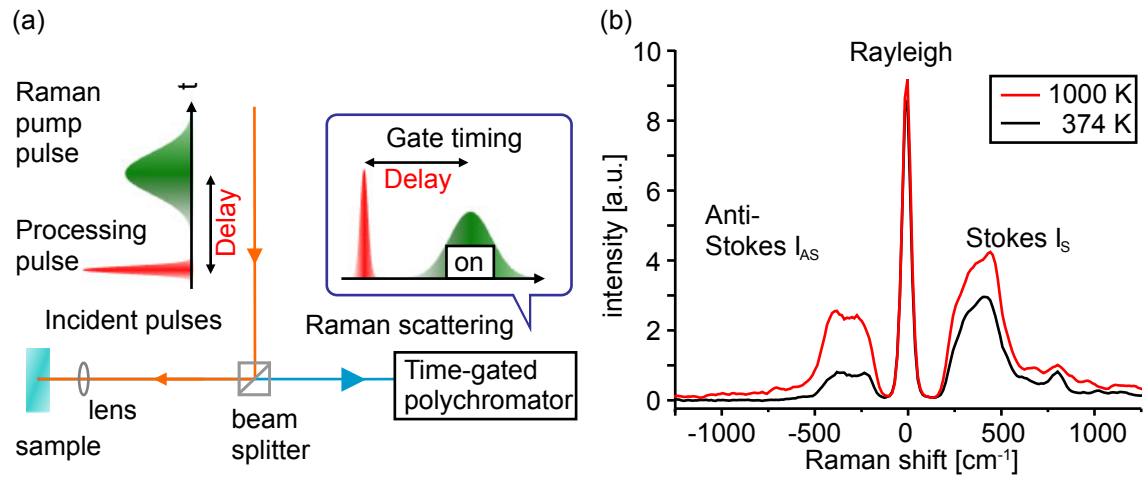


Fig. 3.6: Principle of *in-situ* Raman microscopy. (b) Raman spectra of a glass sample at room temperature (black line) and at increased temperature (red line)

The Raman shift $\Delta\omega$ is typically given in wavenumbers $\bar{\nu}$ (unit: cm^{-1}) and is calculated as the difference between the inverse wavelength of the excitation wavelength λ_0 and the Raman signal wavelength λ_S :

$$\Delta\omega = \bar{\nu}_0 - \bar{\nu}_S = \left(\frac{1}{\lambda_0} - \frac{1}{\lambda_S} \right) \quad (3.8)$$

The intensities of the Stokes I_S and Anti-Stokes I_{AS} Raman scattering signal are given by [120]:

$$I_S \approx \frac{(\nu_0 - \nu_R)^4}{1 - \exp\left(-\frac{h\nu_R}{k_B T}\right)} \quad (3.9)$$

$$I_{AS} \approx \frac{(\nu_0 + \nu_R)^4}{\exp\left(\frac{h\nu_R}{k_B T}\right) - 1} \quad (3.10)$$

where h is the Planck constant, ν_0 is the frequency of the excitation, ν_R is the frequency of the internal Raman transition (equals $c \cdot |\Delta\omega|$ with c the speed of light), and k_B is the Boltzmann constant. At room temperature, only a few phonons are excited, leading to a weak Anti-Stokes signal and a more intense Stokes signal. With increasing temperature especially the intensity of the Anti-Stokes signal increases. Exemplary Raman spectra can be seen in Figure 3.6 (b). The ratio between Stokes I_S and anti-Stokes I_{AS} Raman signal depends basically on the temperature, which reflects the Boltzmann distribution of thermally excited phonons [120, 121]:

$$\frac{I_{AS}}{I_S} = \left(\frac{\nu_0 + \nu_R}{\nu_0 - \nu_R}\right)^4 \exp\left(-\frac{h\nu_R}{k_B T}\right). \quad (3.11)$$

To calculate the temperature based on the Stokes and anti-Stokes signal, the Raman spectra between 200 cm^{-1} and 560 cm^{-1} were analyzed. Beside the temperature, Equation 3.11 also depends on the Raman transition ν_R . Thus, to estimate the temperature a least square fitting method was used. For an assumed temperature the anti-Stokes Raman spectrum was calculated by Equation 3.11 from an experimentally measured Stokes spectrum. The actual temperature is determined by minimizing the deviation between the calculated and measured anti-Stokes Raman spectra.

To measure the intensities of the Stokes- and Anti-Stokes signal during the processing with ultrashort laser pulses an appropriate setup was designed, as shown in Figure 3.7. An amplified Ytterbium fiber laser system (IMRA μ Jewel) delivering 600 fs pulses at a wavelength of 1044 nm and a repetition rate of 1 MHz was used to induce heat accumulation in the material. The maximal pulse energy was 1100 nJ. For the Raman pump, a frequency-doubled Nd:YAG laser was used to generate 10-ns pulses with a repetition rate of 1 kHz at a wavelength of 532 nm (maximal pulse energy of 300 nJ). Pump and processing pulse were electronically synchronized by a pulse delay generator (DG535; Stanford Research

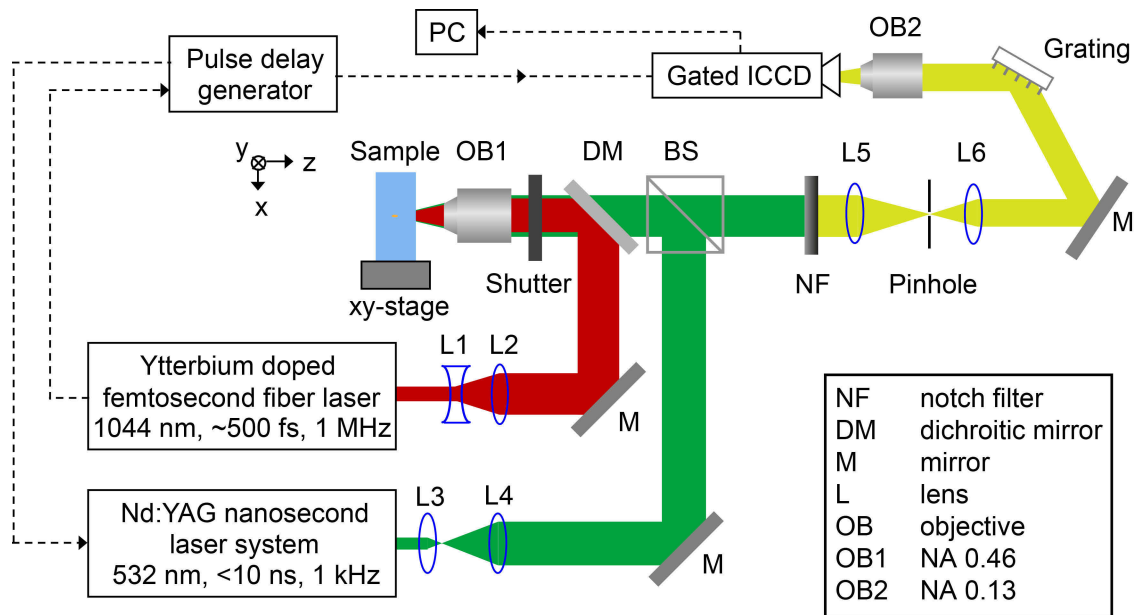


Fig. 3.7: Setup of the Raman temperature measurement. The numerical apertures (NA) of the objectives are stated in the figure. The diameter of the pinhole is $25\ \mu\text{m}$.

Systems) and then focused by a $20\times$ microscope objective (OB1, NA 0.46) $200\ \mu\text{m}$ below the sample surface. The back-scattered Stokes and anti-Stokes Raman signals from the focus were detected by an ICCD camera through a confocal pinhole followed by a reflective blazed grating with 600 lines per mm. The gating time of the ICCD was set to 10 ns to match the length of the Raman pump pulse. As the Raman signal of glass is very weak the spectra were accumulated over 20000 pulses. A 532-nm notch filter (NF) was used to eliminate the Raman pump pulses. Irradiation of already processed material distort the temperature measurements. Thus, the sample was translated with a computer-controlled xy-stage to prevent multiple irradiations. In addition, different velocities can be used to measure the influence of the spatial pulse overlap on the induced temperature. Lens L2 can be aligned in all three dimensions to correct the chromatic aberrations of the focusing objective (OB1) and to change the position of the processing pulse with respect to the Raman pulse. This allows the spatial mapping of the temperature distribution. The shift of the processing pulses was conducted perpendicular to the scanning direction to avoid probing of already processed material. To calibrate the setup, the temperature of the sample was measured without any excitation. The measured temperature was $305 \pm 15\ \text{K}$ in good agreement with the room temperature (295 K).

3.2.2 Background signal

To calculate the temperature a clear spectrum with detectable Stokes and Anti-Stokes Raman signal is required. In a distance of $\leq 2 \mu\text{m}$ to the central position and for short delay times (a few hundred ns) however, the measured spectra are overlaid by a large background signal. Generally the background signal increases with increasing pulse energy and with decreasing distance between measuring point and central processing position. Figure 3.8 (a) shows the background signal and its temporal decay. These spectra were measured $1 \mu\text{m}$ from the central excitation. The low intensity around $0 \pm 100 \text{ cm}^{-1}$ is due to the notch filter. Here, no Raman laser was used, thus the detected signal originates solely from the fs-processing pulse (pulse energy 940 nJ at a wavelength of 1044 nm). The times given (different colors) state the delay between the processing pulse and the gating of the ICCD, identifying the dynamic decay of the background signal.

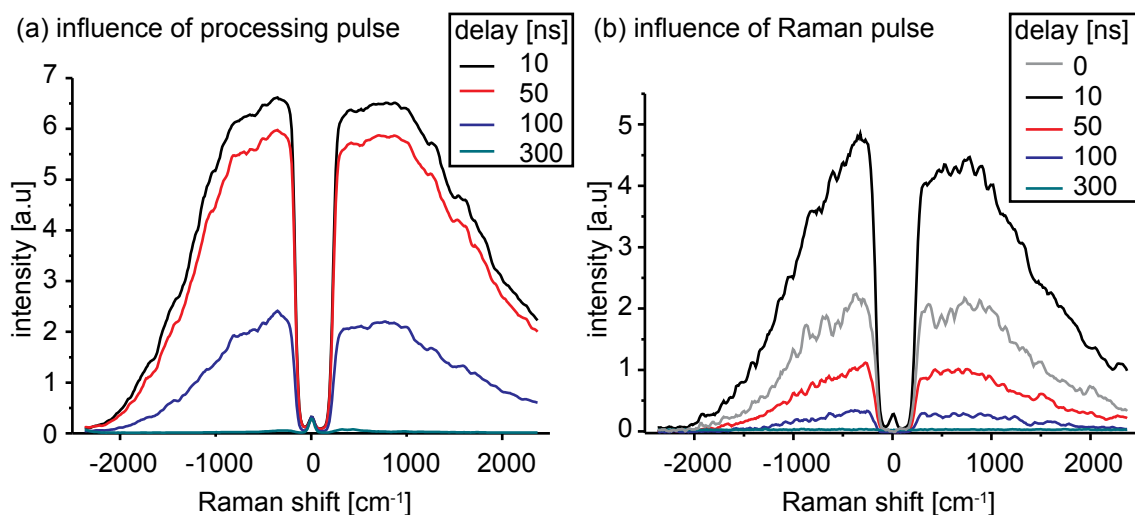


Fig. 3.8: Dynamic of background signal: (a) Background signal induced solely by the fs-processing pulse (b) Background signal after the ns-Raman pulse has irradiated the sample. The delay between the processing pulse and the Raman pulse was fixed to 100 ns. For both conditions a processing pulse energy of 940 nJ and a notch filter was used.

Directly after the excitation the background signal is very strong and much more intense than any possible Raman signal. With increasing delay the background signal decreases and eventually vanishes after about 300 ns. In addition, the ns-Raman pulse can induce a background signal, too [see Figure 3.8 (b)]. The delay between processing and Raman pulse was fixed to 100 ns. Here, the delay times given indicate the delay between the Raman pulse and gating of the ICCD. At a delay of 0 ns no Raman pulse was used and

the detected background signal (gray curve) originates solely from the processing pulse. After the Raman pulse excited the sample (delay of 10 ns) the background signal increases again (black line). Afterwards the signal decreases (e.g. red curve), showing a decay time of less than 300 ns. This measurement shows, that ns and fs pulses give rise to a large background signal, requiring about 300 ns to decay. However, without an initial excitation with ultrashort laser pulses, no background signal was observed, as the intensity of the ns-pulse is too weak to induce non-linear absorption.

To analyze the spectral composition of the background signal, the emission spectrum was measured during the excitation (pulse energy 1100 nJ) of a borosilicate (B33) sample, using a commercial spectrometer, which allows no time gating. Figure 3.9 shows the detected signal as a function of the wavelength. To compare the background signal with the spectral range required for the Raman analysis (200 cm^{-1} - 560 cm^{-1}), the upper axis shows the Raman Shift for an excitation wavelength of 532 nm. The emission spectrum of the processed area (Figure 3.9) exhibits an intense and broad signal detectable over the entire spectral range. Furthermore, additional distinctive peaks atop the broad emission band can be found.

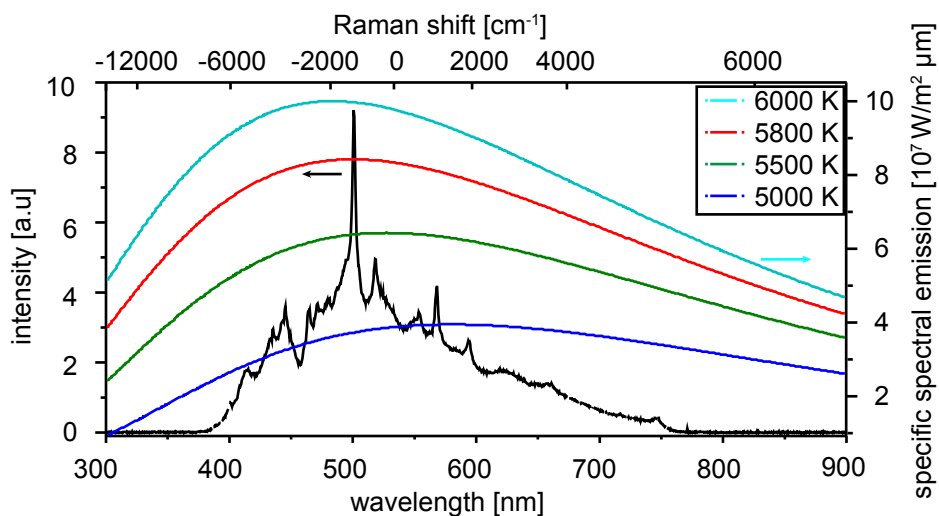


Fig. 3.9: Time integrated emission spectrum of laser excited borosilicate glass. The dashed lines indicate the spectral emission of a black body at different temperatures. For the Raman Shift an excitation wavelength of 532 nm was used.

The background signal is most likely due to three different sources. First of all, black body radiation of the processed volume: Following Wien's displacement law, the blackbody radiation which features a maximum at a wavelength of 500 nm has to exhibit a temper-

ature of 5800 K. With decreasing temperature the wavelength maximum shifts towards higher wavelengths and thus away from the detectable spectral range of the setup used. Furthermore, the power radiated from a black body is directly proportional the fourth power of the black body's temperature, resulting in weak black body radiation for low temperatures. The spectral emission of a black body is plotted in Figure 3.9 for different temperatures. In general, the black body emission for temperatures around 5800 K fit to the measured emission spectra of the laser excited borosilicate glass. The main differences between the black body emission spectra and the measured one occurring for high and low wavelengths, are due to the insensitivity of the spectrometer for wavelengths below 400 nm. In addition, an 800 nm shortpass filter was used to eliminate the processing pulse. Furthermore, the detected signal has to be an integration of multiple black bodies at different temperatures, depending on the heat diffusion of the excited material, as the spectrum analyzer allowed no temporal informations. However, the measured emission spectra decrease for high wavelengths much faster than the black body emissions spectra. Thus, additional effects have to contribute to the background signal.

Sharp emission peaks atop of a broad emission spectrum of local heated glass have not been reported so far. A possible explanation is the emission of a line spectrum of the induced plasma. However, the assignment of the emissions lines to exact transitions is difficult, as Borosilicate consists of multiple components, which also can occur in different ionization states. A third contribution to the background signal is fluorescence of defects and color centers induced in the Borosilicate glass [38, 122]. These defects were initially induced by the first processing pulses. The excitation by subsequent pulses give rise to a broad fluorescence signal. With increasing distance from the processing center the amount of defects decreases and consequently the background signal is reduced, too. For Borosilicate the formation of numerous color centers is well known [38, 122, 123]. Color centers normally exhibit broad fluorescence peaks, e.g. one also centered at 500 nm [122]. Furthermore, self trapped excitons in fused silica exhibit a fluorescence band at about 540 nm [124] whereas NBOHCs show a fluorescence band centered at 650 nm [125]. In addition, Stathis et al. reported a photoluminescence decay time in fused silica, which is comparable to the presented results [88].

The detected background signal is a combination of all three effects mentioned. Thus, the background signal can not be avoided, hindering the detection of an analyzable Raman signal under certain conditions. Thus, it is impossible to measure the highest temperatures, which are expected close to the center of the modification, for short delay times and

for high applied pulse energies. Therefore, the absolute temperatures in the center and for short delay times have to be interpolated from the results obtained in the surrounding area and for longer time delay. One possible way is presented in Section 3.2.4.

3.2.3 Heat accumulation of various glasses

Different samples have been investigated: Fused silica, BK7, Borofloat 33 (B33), ULE and Zerodur. All of them show the mentioned background signal under certain processing conditions, whereas most of these glasses show no measurable laser induced temperature change. This is due to the limited repetition rate of 1 MHz and pulse energy of 1100 nJ at rather long pulse duration (600 fs) and wavelength (1044 nm).

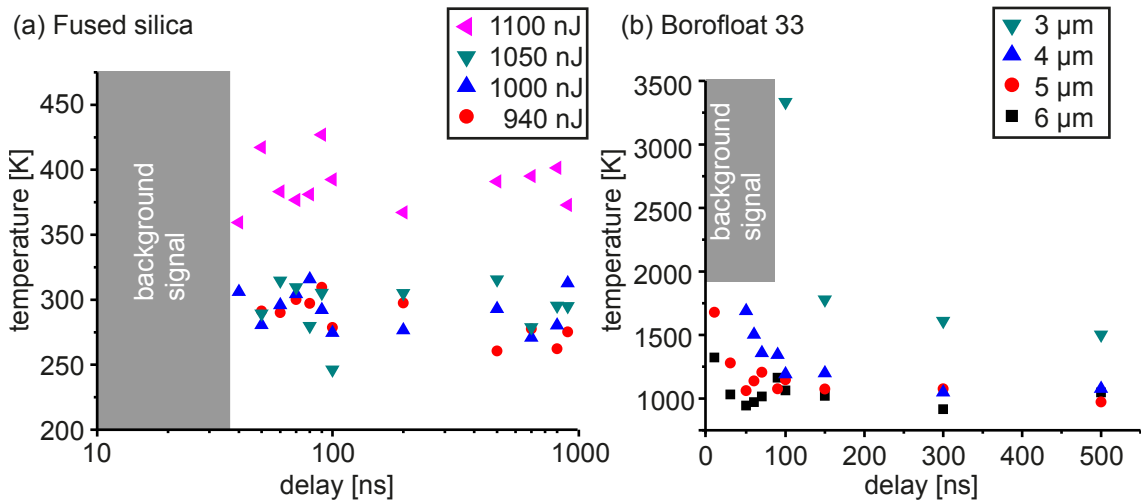


Fig. 3.10: (a) Laser induced temperature in fused silica for different pulse energies in the center of the modification. (b) Laser induced temperature in B33 for different distances from the center using a processing pulse energy of 1100 nJ.

Figure 3.10 shows the laser induced temperature distribution obtained from the Anti-Stokes/Stokes ratio for different samples: (a) fused silica and (b) Borofloat 33. In fused silica, only the highest pulse energy of 1100 nJ induces a slight temperature increase of about 100 K (for delay times ≥ 40 ns after irradiation). Although the background signal hinders the detection of a Raman signal for delay times below 30 ns a temporal decay due to heat diffusion of the induced temperature should occur for longer delay times. Thus, the measured "temperature" rise in fused silica can not be attributed to a laser induced temperature change. Instead, laser induced structure changes might have changed the Raman signal.

On the contrary, B33 shows an increasing temperature with decreasing distance to the center. Furthermore the measured temperature decreases with the delay time as one would expect for thermal diffusion. In conclusion, only the borosilicate glasses (BK7 and B33), showed a measurable temporal heat distribution. However, the irradiation with pulse energies of at least 950 nJ fractured the BK7 glass, leaving only B33 as possible sample.

3.2.4 Spatial and temporal temperature distribution

It was shown in Figure 3.10 that it is possible to measure the temporal and spatial temperature dynamics in borosilicate glass. Due to the technical limitations, fused silica was not suited for these Raman experiments. Nonetheless, borosilicate glass may serve as a model system to investigate the temperature distribution after excitation with multiple laser pulses. For these experiments the repetition rate was fixed to 1 MHz and for most experiments a translation velocity of 1 mm/s was used.

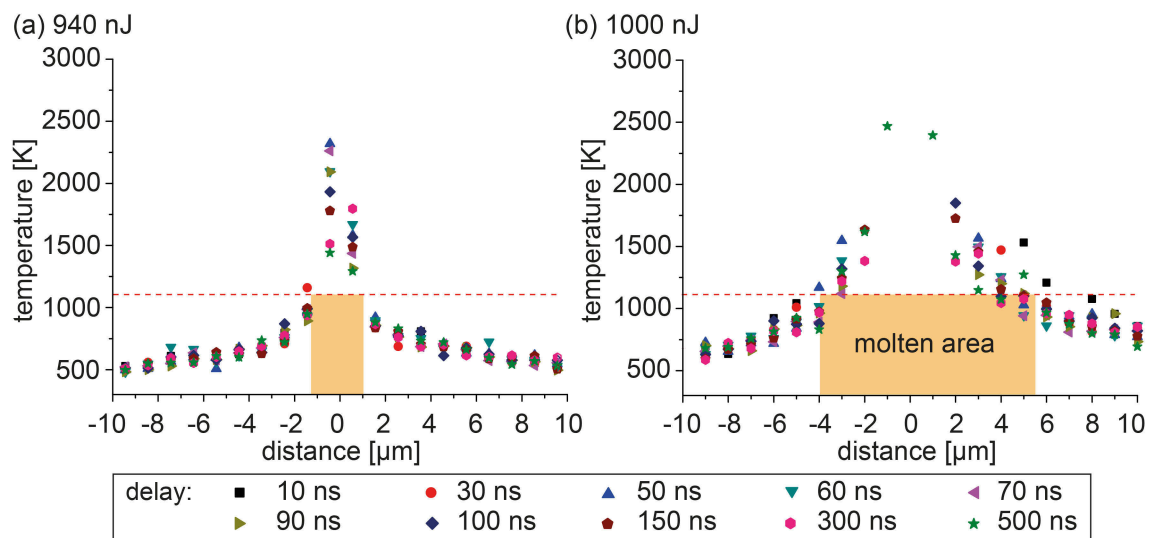


Fig. 3.11: Measurements of temperature as function of the distance to the central position for a processing pulse energy of (a) 940 nJ and (b) 1000 nJ. The red dashed line indicates the softening point of Borofloat 33. The translation velocity was 1 mm/s. The orange shaded area highlights the region where the softening point is exceeded, indicating the size of the molten area.

Figure 3.11 depicts the temperature evolution for two different processing pulse energies. As x-axis the distance of the measuring point to the central position is used. The red dashed line indicates the softening point T_S of Borofloat 33. The emission of the men-

tioned background signal hinders the temperature measurement within the central area and particularly for short delay times. In general, both temperature distributions show a similar shape, although the absolute values are different. For both pulse energies the measured temperature decreases with increasing distance to the center. At a distance of $10\ \mu\text{m}$ the temperature is still above the ambient temperature (300 K), indicating a large area affected by the heat accumulation. If one compares the same measurement points, the temperature obtained by a processing pulse energy of 940 nJ is lower than for 1000 nJ. At a pulse energy of 940 nJ [(Figure 3.11 (a))] only a region with a diameter of $2\ \mu\text{m}$ (red shaded area) exhibits a temperature above the softening point of Borofloat 33. In comparison, the molten area should have a diameter of almost $10\ \mu\text{m}$ for a pulse energy of 1000 nJ [Figure 3.11 (b)]. Here, within the close vicinity of the center ($\pm 1\ \mu\text{m}$) the temperature is about 2500 K even for a delay time of 500 ns (green stars), indicating the extremely high temperatures within this central area.

To obtain additional information about the dynamic of the central temperature for short delay times a careful interpolation of the measured data points is required. For this, a spatial Gaussian temperature distribution was assumed, as it solves the heat diffusion equation (Equation 3.3). However, this simple approach does not fit to the measured data, see Figure 3.12.

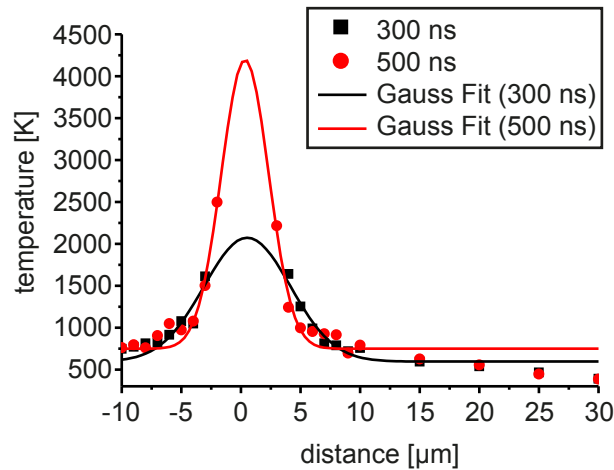


Fig. 3.12: Measured temperature distribution (points) for two different delay times induced by a pulse energy of 1000 nJ and appropriate fits assuming a simple Gaussian distribution.

This approach leads to several deviations from the experimental data: The background temperature (at large distances) is not correctly fitted. Furthermore, the wings of the Gaus-

sian temperature rise underestimate the measured data. Most importantly, the maximal temperature fitted for a delay time of 500 fs is much higher, than for a delay of 300 fs. This contradicts the heat diffusion and is due to the lack of information in the central region. To solve this problem one has to consider the time dependence of the temperature evolution, too. The large background temperature and the deviation at wings of the Gaussian distribution, is due to the heat accumulation of the multiple successive pulses. It was shown in [114] that a Gaussian fit agrees very well to the temperature distribution induced by a single pulse. However, in this experiment multiple pulses excite the sample in a short temporal distance, resulting in heat accumulation. Thus, the resulting heat distribution is the accumulation of all the previous processing pulses. The spatial and temporal temperature distribution after photoexcitation can be expressed as [126]:

$$T(t, r, z) = Q \frac{(w_{th}/2)^2}{(w_{th}/2)^2 + 4Dt} \cdot \left[\frac{(l_z/2)^2}{(l_z/2)^2 + 4Dt} \right]^{1/2} \exp \left[-\frac{(r+B)^2}{((w_{th}/2)^2 + 4Dt)} - \frac{z^2}{((l_z/2)^2 + 4Dt)} \right] \quad (3.12)$$

where D is the thermal diffusivity of the material and w_{th} and l_z are the widths of the distribution in the radial direction and in the beam propagation direction, respectively. Q is a scaling factor and B reflects the spatial offset. If one considers the accumulation of N pulses at $z=0$, Equation 3.12, can be written as:

$$T(t, r, z = 0) = A \sum_{n=0}^N \left[\frac{(l_z/2)^2}{(l_z/2)^2 + 4D(t + n/f_{rep})} \right]^{1/2} \cdot \frac{(w_{th}/2)^2}{(w_{th}/2)^2 + 4D(t + n/f_{rep})} \times \exp \left[-\frac{(r-B)^2}{((w_{th}/2)^2 + 4D(t + n/f_{rep}))} \right] \quad (3.13)$$

Here, f_{rep} is the repetition rate of the laser pulses. A is a free fitting parameter. Note that this model neglects the temperature dependence of the diffusivity. In addition, it is assumed that the width w_{th} of the initial heat distribution is the same for each pulse. Thus, additional cumulative effects - as a decrease of the absorption threshold for multiple pulse irradiation - are neglected, too.

Equation 3.13 was used to fit the measured temperature for all time delays and distances at a fixed pulse energy and translation velocity. The parameters A , B , D , w_{th} and l_z were used as fitting parameters, but were kept constant in space and time. A least mean square

fitting was used to minimize the difference between the measured data and fitting curve assuming Equation 3.13. With increasing number of pulses N the difference between experimental result and the fitting curve decreases. Assuming that the diameter of the initial excitation is about $2\ \mu\text{m}$ for a scan velocity of $1\ \text{mm/s}$ one has to consider the accumulation caused by 2000 pulses (i.e. $N = 2000$).

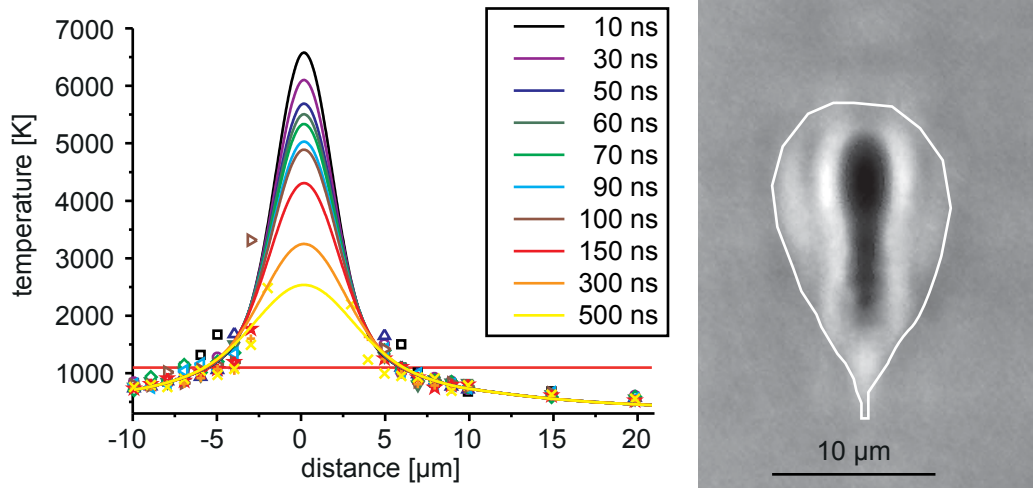


Fig. 3.13: Measured temperature distribution induced by a pulse energy of $1100\ \text{nJ}$. As fit the accumulation of multiple pulses (Equation 3.13) was used. The microscope image shows the corresponding induced modification. The dotted line in the microscope image retraces the molten area.

Figure 3.13 shows the measured temperature distribution and the appropriate fitting curve for a pulse energy of $1100\ \text{nJ}$. Here, the temperature decreases with respect to the distance from the central position and for increasing delay times. The background temperature fits to the measured results and also the deviations at the wings of the fitting curves are reduced. Nevertheless there are still some disagreements as can be seen in Figure 3.13. The origin of this discrepancy could be the temperature dependence of D and the constant w_{th} for all pulses. However, this figure gives the first comprehensive overview about the temperature dynamics of glass excited by multiple ultrashort pulses. A maximal temperature of about $7000\ \text{K}$ is reached directly after the excitation ($10\ \text{ns}$). This central temperature drops within $500\ \text{ns}$ to about $2500\ \text{K}$, which is still above the softening point. Within a diameter of $12\ \mu\text{m}$ the temperature is above the softening point, in good agreement to the microscope image of the modified region, see right part of Figure 3.13.

In this experiment, the pulse energy strongly influences the induced temperature. Figure 3.14 (a) shows the induced temperatures for a delay of $10\ \text{ns}$ directly in the center. For a

pulse energy of 1100 nJ temperatures of up to 7000 K are obtained, whereas a pulse energy of 970 nJ yields only a temperature of 1500 K. With increasing translation velocity, i. e. with decreasing number of pulses, the induced temperature decreases, in agreement to the simulations in Section 3.1.

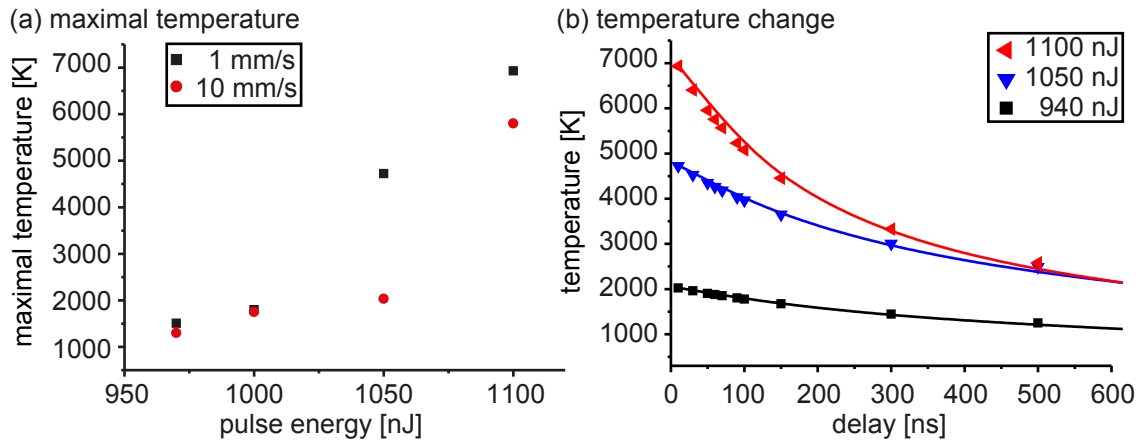


Fig. 3.14: (a) Maximal laser induced temperature with respect to the pulse energy. (b) Temporal decay of the induced temperature within the central position. Here, the translation velocity is 1 mm/s.

For the pulse energies investigated the temporal decay of the induced temperature occurs within a few hundred ns, see Figure 3.14 (b). The curves were fitted by the following equation:

$$T = \frac{a}{b + t} + c, \quad (3.14)$$

where a , b , c are constants. Equation 3.14 is the theoretical time evolution of the temperature for a cylindrical heat source with an infinite length [114]. This approximation was also done by Miyamoto et al. to calculate the temperature distribution in borosilicate glass [31]. The time constant b denotes the time at which the temperature is decreased by its half. This decay time of the induced temperature is in the range of a few hundred ns, for all pulse energies investigated. For example, at a pulse energy of 1100 nJ the temperature decay time is about 200 ns, whereas a pulse energy of 940 nJ yields a temperature decay time of 400 ns.

Beside the information about the evolution of the induced temperatures, the results of the Raman measurements can be used to estimate the size of the induced modification.

To this end, the region where the temperature exceeds the softening point of Borofloat 33 was considered, as shown in Figure 3.11. Here, especially for high pulse energies the uncertainty of the width of the molten region is relatively large [see Figure 3.11 (b)]. In addition, the widths of the modifications were measured with a microscope. Within this measurement the error bars are due to the low contrast between the molten (slightly bright region) and non-modified region.

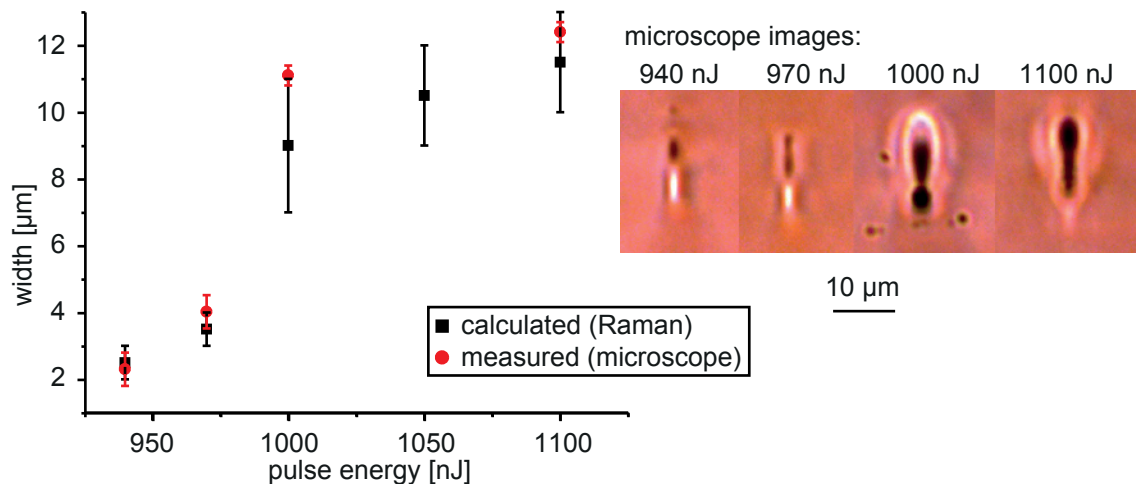


Fig. 3.15: Width of the laser induced modification calculated based on the temperatures determined from the Raman measurements and measured using microscope images. The microscope images show the front view of the appropriate modifications.

The calculated widths of the Raman results (black points) and the measured (red points) widths of the molten area for different pulse energies are shown in Figure 3.15. The appropriate microscope images are shown, too. For a pulse energy of 940 nJ, the induced modification is very thin with a diameter of a few μm , whereas with increasing pulse energy the width increases up to a diameter of 12 μm at a pulse energy of 1100 nJ. The length increases, too. The central dark modification, visible in the microscope images originates from a region with high temperatures, higher than the working point of the glass [27, 127]. Both techniques, *in-situ* Raman measurement and post-processing microscopy yield comparable results, proving the capability of the *in-situ* Raman measurement. Direct temperature measurements using micro-Raman spectroscopy proved that the temperature induced by heat accumulation of successive pulses exceeds the softening point of the material in a large region. For a repetition rate of 1 MHz temperatures up to 7000 K were observed. The measured life time of the temperature was in the range of a few hundred ns. The results obtained by the *in-situ* Raman measurements are the first comprehensive ex-

perimental results concerning the temporal and spatial temperature distribution induced by heat accumulation of ultrashort laser pulses. The measurements were conducted in borosilicate glass whereas a direct transfer of the results to e.g. fused silica was not possible due to the limited parameters of the laser system used here. An extrapolation of the results obtained for borosilicate glass to fused silica is not possible due to their different material properties. In glasses, no latent heat is required to perform the phase transition from the solid phase to the liquid one [109]. However, with increasing temperature the heat capacity will change. Furthermore, the temperature dependence of other material properties as the heat conductivity for high temperatures are unknown and depend on the individual equilibrium values at room temperature. In addition, the different viscosity of the two glasses hinders an extrapolation of the results obtained. Thus, for an estimation of a temperature distribution in fused silica more experimental results about the temperature dependence of the material properties are necessary.

4 Direct Laser Bonding - Fundamentals

Before the results of the bonding experiments are presented, at first fundamentals about the required processing parameters and the absorption process of the laser pulses are investigated. During the bonding process of glass, multiple other effects occur. The heating and fast quenching of the material induces structural changes within the glass network. To analyze this, Raman spectroscopy and IR-Absorption spectroscopy was used. Furthermore, the laser induced melting of fused silica is accompanied by the formation of large disruptions, exhibiting a diameter of up to 12 μm . Their shape, occurrence and possible formation mechanism will be explained in the following. Both, the induced structural changes as well as the disruptions induce stress fields surrounding the modifications. These stress fields limit the stability of laser bonded samples. A possible way to reduce the laser induced stress is presented in the final section of this chapter.

4.1 Processing window for laser bonding

A fundamental processing parameter to induce heat accumulation and thus bond two transparent materials is the laser repetition rate, since it determines the cooling time of the material between the individual pulses, as shown in Section 3.1.1. In addition, the absorbed energy of a laser pulse sets the induced temperature rise. By changing these two parameters, heat accumulation can be obtained in several glasses. To evaluate the required processing parameters for laser bonding of fused silica, a detailed experimental study of their influence on the induced material modification was conducted. To this end, an ultra-short pulse oscillator delivering pulses with a pulse duration of 450 fs and an aspheric lens with NA of 0.5 was used. The inscription process was repeated for different translation velocities between 1 and 1000 mm/min for every repetition rate and pulse energy. In do-

ing so, the parameter set was determined at which the processed material showed melting due to heat accumulation. Figure 4.1 shows the resulting modifications with respect to the processing parameters. The square spots indicate measured data points. For low average power (blue shaded area) no visible modifications were obtained. This parameter set was not further analyzed, although some of these modifications may exhibit an isotropic index shift. When using average laser powers of about 100 mW (green shaded area), the induced modifications become birefringent, indicating the formation of nanogratings. Interestingly, it is possible to induce birefringent modifications with repetition rates up to 9.4 MHz, allowing the efficient and rapid inscription of nanogratings at high translation velocities.

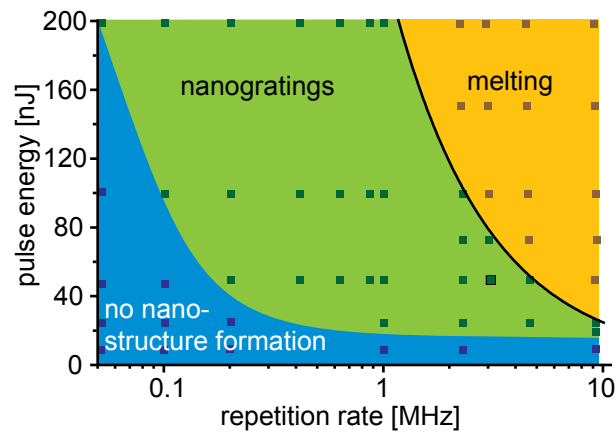


Fig. 4.1: Laser induced modification in fused silica with respect to the processing parameters. A pulse duration of 450 fs and NA of 0.5 was used. The inscription process was repeated for different translation velocities between 1 and 1000 mm/min. Melting due to heat accumulation was only observed for high laser powers (yellow shaded area).

Heat accumulation and thus melting of the material occurs within a well-defined range of processing parameters. The minimal usable repetition rate is inversely proportional to the pulse energy (dashed line in Figure 4.1), indicating the average laser power as crucial parameter. In the experiments, the minimal average power to induce melting in fused silica was 230 mW (dashed line). Starting at this average power, the birefringent structures vanish, due to the heat accumulation of subsequent laser pulses and the accompanied homogeneous melting of the material [22].

In Chapter 3 it was shown that the size of the molten material can be increased by using higher average power. The simulations considered a fixed absorption of 75 %, neglect-

ing the influence of the pulse duration. However, the absorptivity depends on the pulse duration. For very short laser pulses (below 200 fs [56]), photoionization can dominate avalanche ionization and produce sufficient free electrons to induce material modifications [53]. Here, the photoionization rate increases with decreasing pulse duration [55]. With increasing pulse duration photoionization provides only a few seed electrons while avalanche ionization is the dominant process for the generation of free electrons [57]. The described mechanisms are based on simplified models and highly non linear. Thus, to verify the influence of the pulse duration on the absorptivity and on the amount of molten material additional experimental results are required. To this end, a tunable ultra-short pulse oscillator (Femtsource XL 50, Femtolasers GmbH) was used. This systems delivers pulses at a wavelength of 800 nm, a repetition rate of 5.1 MHz and a pulse energy of 500 nJ. By tuning the position of the compressor prisms the pulse duration can be varied between 40 fs and 400 fs. The pulse duration was measured by a FROG (Grenouille, Swamp Optics). Continuous lines were written at different translation velocities 170 μm below the surface of fused silica with an objective with a NA of 0.55. Subsequently, the width of the inscribed lines was measured.

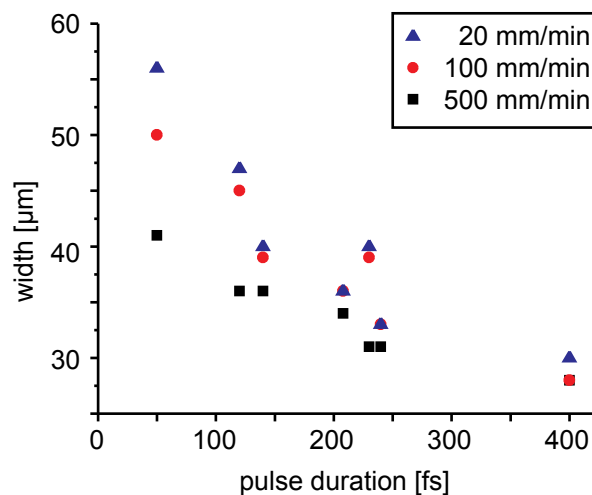


Fig. 4.2: Width of laser inscribed lines in fused silica with respect to the pulse duration of the laser pulses, using different translation velocities. The repetition rate was 5.1 MHz, pulse energy was 500 nJ and NA was 0.55.

Figure 4.2 shows the width of the induced modifications for three translation velocities with respect to the pulse duration. In general, the width of the molten material increases with decreasing translation velocity, due to the larger spatial pulse overlap and a larger av-

erage power per laser spot, in accordance to Section 3.1.2. With increasing pulse duration the melt width decreases from initially 56 μm to about 30 μm , confirming that the absorptivity of ultrashort laser pulses decreases with increasing pulse duration [53]. Thus, the application of very short laser pulses (about 100 fs) is more efficient in terms of processing speed. However, the results presented in Chapter 5 were conducted with an oscillator delivering pulses with a pulse duration of 450 fs, due to technical reasons.

4.2 Absorption of successive ultrashort laser pulses

As discussed in the previous chapters, successive pulses with a temporal distance of below 1 μs are required to induce heat accumulation in fused silica. Although the different non-linear absorption mechanisms (Section 2.2) are well known and the principle model about the stepwise increase of the temperature in the modified area is established (Section 2.5), there are still some open questions concerning the absorption process.

As shown before, the absorptivity depends on the pulse duration. In addition, the absorptivity of pristine and already processed material is different enabling the formation multiple effects in material processing, e.g. the formation nanogratings [10, 76]. Rajeev et al. measured a feedback mechanism in the nonlinear absorption of fused silica and accounted therefor chemical changes [128]. However, the mediating effect between isolated pulses is still not fully resolved.

The irradiation of glass with numerous pulses at high repetition rates increase the temperature and generate free electrons leading to an increased linear absorption. To exclude the attribution of the heat accumulation to the absorption mechanism of ultrashort laser pulses a double pulse experiment was designed, at which the double pulses had a repetition rate of 100 kHz. At these repetition rates (and pulse energies below 1 μJ) no heat accumulation in fused silica occurs. A very convenient method to quantify laser induced modifications in fused silica is to analyze the formation of nanogratings. The number of laser pulses required to form a homogeneous nanograting depends also on the absorbed pulse energy [76]. Thus, if there is a difference in the absorbed laser pulse energy of successive pulses the formation state of the nanogratings will depend on the temporal separation of the laser pulses. The formation state of a nanograting is linearly connected with its form birefringence [17, 129]. The retardation δ for values of $\delta \lesssim \pi/4$ is roughly proportional to the polarization contrast intensity (*PCI*) $PCI \sim \sin \delta$, at which the *PCI* can be determined

by placing a nanograting between two crossed polarizers and measuring the transmission of this setup [17, 130]. To realize different pulse delays a Mach-Zehnder interferometer was designed, generating symmetric double pulses with a defined pulse delay τ between 500 fs and 1 ns [131]. Here, a regeneratively amplified Ti:sapphire laser system (150 fs, 800 nm, 100 kHz) was used. With the designed Mach-Zehnder interferometer birefringent lines were inscribed, using a translation velocity of 12 mm/min. At first, the *PCI* of the induced structure was measured and plotted against the temporal separation τ of the double pulses, see Figure 4.3.

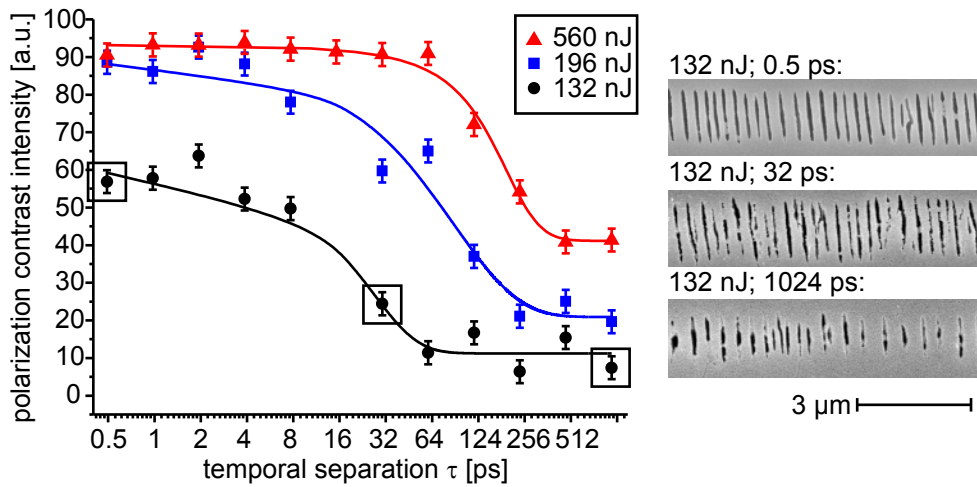


Fig. 4.3: Polarization contrast intensity of inscribed nanogratings with respect to the temporal pulse delay of the irradiating double pulses (repetition rate of 100 kHz). The solid lines serve as guide to the eye. The SEM images correspond to the marked data points.

The stated pulse energies refer to the energy of one pulse within the double pulse train. Generally, the *PCI* increases for higher pulse energies and is enhanced for pulse separations shorter than 100 ps and about 20 ps for a pulse energy of 560 nJ and 132 nJ, respectively. After these delay times the *PCI* decreases significantly. The SEM pictures at the right side of Figure 4.3 correspond to the marked points within the graph. Using 132 nJ pulses the formation of a homogeneous grating can only be found for a pulse separation of 0.5 ps while with increasing delay time (e.g. 1024 ps) the nanostructure obtained exhibits unmodified areas and an increasing grating period, indicating that the formation process is still in its early stages [76]. When using the same processing condition in a single pulse experiment (same number of irradiating pulses) the *PCI* is similar to the value obtained for the double pulse setup at a delay of 1024 ps.

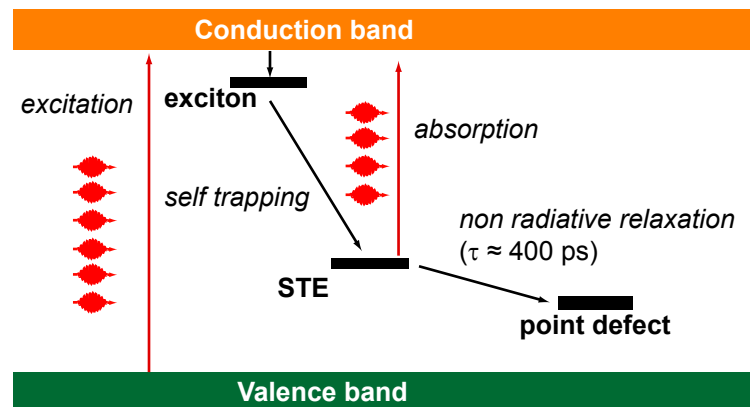


Fig. 4.4: Schematic band diagram of fused silica with laser induced Self Trapped Excitons (STEs).

The observed dependence of the pulse separation may be explained by the laser induced formation of Self Trapped Excitons (STEs) and their subsequent decay into point defects within several hundred ps [131]. After the nonlinear absorption of the laser pulse excitons are formed [132]. An exciton can be trapped by its own distortion field at a lattice site initially free of defects [133]. The result of this localization is called Self Trapped Exciton. Also the interaction with small lattice distortions like an atomic displacement may lead to a trapped exciton [134]. At room temperature, the STEs relax to permanent point defects like E'-centers and non-bridging oxygen hole centers (NBOHCs) [74, 88, 135]. The decay time for this relaxation was deduced by Wortmann et al. to about 400 ps [132]. A schematic sketch of the appropriate band diagram is shown in Figure 4.4. For pulse separations shorter than the decay time the presence of STEs increase the absorptivity of the modified material. Thus, the absorption of the following laser pulse is increased and consequently more energy is coupled into the material, enhancing the formation of nanogratings and leading to a more pronounced *PCI* signal. If the pulse delay exceeds the lifetime of the STEs this mechanism ceases lowering the efficiency of the cumulative action. Using a pulse energy of 560 nJ, the *PCI* decreases significantly for a temporal separation of 500 ps in good agreement with the STE decay time of 400 ps reported by Wortmann et al. [132]. The generally reduced *PCI* for lower pulse energies is explained by the energy dependent formation of STEs as reported in [136].

Typical pulse separation used for nanograting inscription is about 10 μ s. Furthermore, nanogratings can be realized even by using a temporal pulse delay of a few ms. Here, (semi)-permanent defects are responsible for the coupling of the individual pulses. As briefly explained above, STEs decay into point defects. In addition, multiple authors re-

ported about the formation of point defects in glasses after the irradiation with intensive laser pulses [86, 128, 137]. One very important group of defects in silicate glasses are the dangling bond type defects (e.g. E'-center or NBOHCs) as they exhibit different absorption bands. To verify the presence of such defects inside the laser modified fused silica the absorption spectra of the sample was measured with a commercially available spectrometer (Perkin Elmer Lambda 950).

To this end two $5 \times 5 \text{ mm}^2$ patterns of parallel lines with $5 \mu\text{m}$ and $1 \mu\text{m}$ spacing were written with a repetition rate of 4.7 MHz and 100 kHz yielding a sample with molten lines and another one containing nanogratings. The applied pulse energy was 200 nJ (pulse duration of 450 fs). The corresponding absorption spectra are shown in Figure 4.5 showing features of dangling bond type defects. In contrast, pristine fused silica (red dashed curve) shows no significant absorption peaks in the spectral range investigated. For the sample containing nanogratings (blue curve) three distinct peaks were observed. The first peak at 212 nm (5.85 eV) is characteristic for E'-centers, whereas the peaks at 248 nm (5.08 eV) and 652 nm (1.9 eV) correspond to NBOHCs inside the glass [35]. In contrast, the sample containing molten lines (black line) exhibits only the peak of the E'-centers. Here, NBOHCs have not been found, most likely due to the high temperatures during the melting of the material resulting in thermal annealing of this defect. In general, the absorption bands of defects are within the band gap of fused silica (9 eV). Therefore, the absorption of laser pulses is enhanced at these defects sites. The measured dependence of the *PCI* on

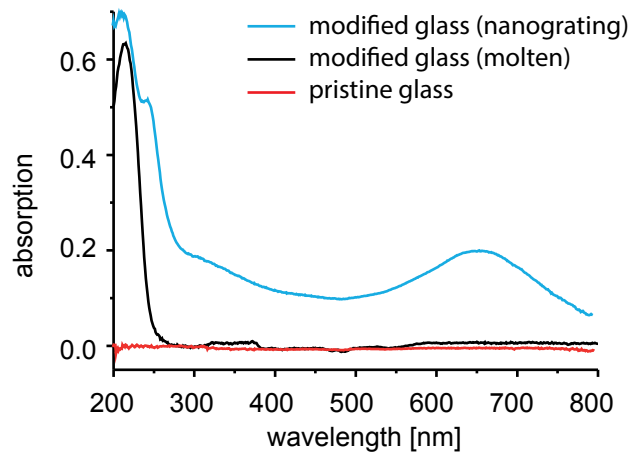


Fig. 4.5: Absorption spectra of modified fused silica. The peaks originate from E'-centers (216 nm) and NBOHCs (248 nm). As reference pristine fused silica is shown [dashed line].

the pulse separation can be explained by partial recombination of the defects with dissociated hydrogenous species [40].

To conclude, two different effects enhance the absorptivity of laser processed glass. Directly after the absorption STEs are formed. These STEs decay within several hundred ps in dangling bond type defects which locally enhance the absorptivity of the material. Defects are responsible for an altered network structure as they reduce the valence of the SiO₂ ring structure. For laser induced bonding of glasses it is important to induce new bonds between the two initially separated samples. Hence, it is interesting to analyze the laser induced structural changes in the modified material.

4.3 Laser induced structural changes

By the fast quenching from a high-temperature melt glass exhibits a higher fictive temperature [44, 86]. For fused silica an increase in fictive temperature is associated with an increase of the density and the refractive index [61]. This principle is used for the inscription of waveguides in fused silica. The accompanied rearrangement of the network can be studied e. g. by Raman spectroscopy [86, 124]. Most of the present knowledge of laser induced structural changes in fused silica were obtained with repetition rates below or at 1 MHz [86, 124, 138]. Here, an increase of the fictive temperature of about 500 K was reported while using pulse energies below 250 nJ [86]. In contrast, the application of higher pulse energies induces a much higher fictive temperature leading to large changes in the density or even the formation of damage in the glass [79, 86].

The principal goal of this thesis is to study the interaction of ultrashort laser pulses with glasses to melt glass and obtain stable bonds using repetitions rates up to 10 MHz and pulse energies below 200 nJ. To avoid processing regimes at which the glass network is heavily damaged Raman microscopy can be utilized to study the laser induced network rearrangements. Figure 4.6 (a) shows a microscope image of the front view of a laser modified region. The repetition rate was 4.7 MHz, pulse energy was 150 nJ and translation velocity was 100 mm/min. The black and red spots in the microscope image indicate the origins where the corresponding Raman spectra of Figure 4.6 (b) were taken. The Raman spectra were measured at an excitation wavelength of 473 nm using an objective with a NA of 0.75 (magnification 50×) with a commercially available Raman Spectrometer (Renishaw, inVia Raman Spectrometer). The notch filter had a transmission cut off at

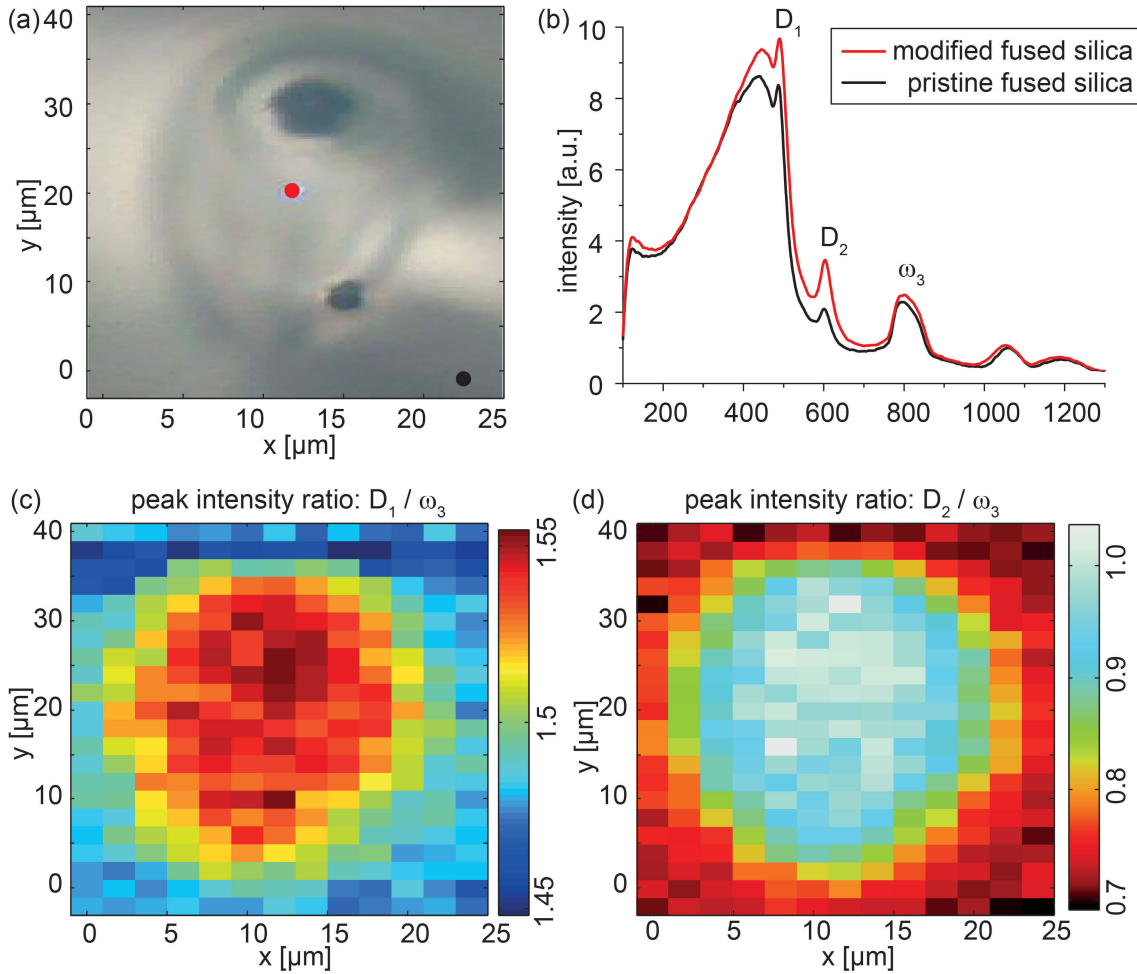


Fig. 4.6: (a) Front view of a laser induced modification. The spots indicate the origin of the corresponding Raman spectra. (b) Raman spectra of modified and pristine fused silica. The laser processing leads to an increase of intensity of the D₁ and D₂ peaks whereas the ω₃ peak stays practically constant. (c), (d) Calculated ratio between the peak intensities of D₁ to ω₃ and D₂ to ω₃, respectively.

100 cm⁻¹. The laser molten area depicts a Raman signal which is different to the signal of the unprocessed glass, see Figure 4.6 (b).

The relative intensity of the defect lines (D₁ and D₂) increases with respect to the intensity of the overall Raman spectra indicating an increasing concentration of 3- and 4-fold silicon-oxygen rings after laser treatment [38, 44]. In agreement to prior publications, no significant change of the ω₃-peak (correlated to stretching modes of Si-O-Si network) was observed [45, 86, 124]. In addition, no other intense changes in the Raman spectra were measured showing that the network structure is still intact. To investigate the change

of the network structure for the entire modified volume [Figure 4.6 (a)] a mapping was conducted. To this end, Raman spectra were recorded with a spacing of $2\ \mu\text{m}$ and the measured spectra were fitted. In a next step, the peak intensities of the D_1 and D_2 were normalized with respect to the ω_3 -peak (at $800\ \text{cm}^{-1}$). The ratio of D_1 to ω_3 increases slightly from 1.45 to 1.55 [Figure 4.6 (c)]. In contrast, the value of D_2/ω_3 increases about 50 % [Figure 4.6 (d)] indicating a large increase of the amount of three-fold rings. Reichmann et al. measured the same relative increase for the inscription of waveguides using a repetition rate of 1 MHz and pulse energy of 115 nJ. An increase of the 3- and 4-fold ring structures leads to a decrease in the overall bond angle and a densification of the glass. These results confirm that new bonds are formed in the entire modified volume.

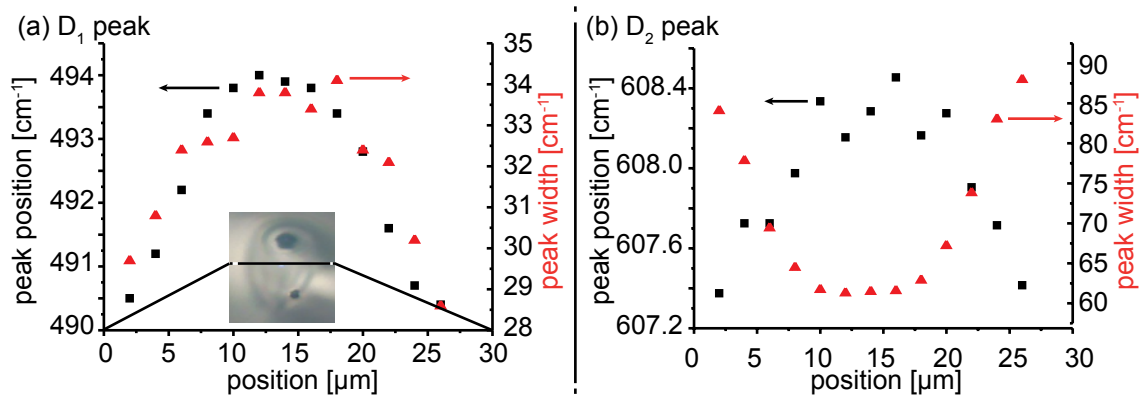


Fig. 4.7: Peak position and peak width of the (a) D_1 peak and (b) D_2 peak. The Raman spectra were measured along the dashed line in the inset.

In a next step, the position and width of the D_1 and D_2 peaks within the modified volume were analyzed. Figure 4.7 shows the corresponding values for both peaks along a horizontal line of the laser modification [see inset in Figure 4.7 (a)]. Within the processed area peak position and peak width of the D_1 and D_2 peaks change significantly. The position of a Raman peak in glass is correlated with an average bond angle within the ring structure. The increasing peak position of the D_1 peak from $490.5\ \text{cm}^{-1}$ to $494\ \text{cm}^{-1}$ corresponds to a decreasing average bond angle of the 4-fold rings within the modified area [60]. Here, also the peak width increases indicating a broader distribution of bond angles. This can be explained by a deviation of the former planar geometry of the 4-fold rings [60]. The peak position of the D_2 peak shifts only slightly from $607.2\ \text{cm}^{-1}$ to $608.4\ \text{cm}^{-1}$. Interestingly, the width of the D_2 peak decreases within the modified volume [see Figure 4.7 (b)]. It was shown in Figure 4.6 that the total number of 3-fold rings increases within the modified

volume. A narrower distribution of bond angles might thus be due to the generation of new planar 3-fold rings.

Agarwal et al. deduced a correlation between the fictive temperature of a glass and its IR reflection peak (at $\approx 8.9 \mu\text{m}$) [139]. The IR-reflection peak of the unmodified fused silica sample corresponds to a fictive temperature of about 1000°C . After the laser treatment the position of the IR reflection peak shifts according to a fictive temperature of $\approx 1700^\circ\text{C}$. Chan et al. deduced a fictive temperature of about 1500°C of fused silica which was processed with a repetition rate of 1 kHz and a pulse energy of $\leq 250 \text{ nJ}$ (800 nm, 130 fs) yielding an isotropic index change [86]. They also stated that destruction of the overall bond integrity occurs at much higher fictive temperature [86, 79]. Thus, the processing of fused silica at rather low pulse energies ($\leq 200 \text{ nJ}$) at high repetition rate results in network rearrangements - especially densification - without a heavy destruction of the entire bond integrity. Instead new bonds are generated.

4.4 Laser induced disruptions

As discussed in the previous chapter, the network structure of fused silica stays intact after the processing with ultrashort laser pulses at high repetition rates. However, in Figure 2.5 and Figure 4.6 (a) dark spots within the modified area can be seen. These modifications are formed only while operating in the heat accumulation regime. The formation of these so-called "micro-bubbles" or "disruptions" appears periodically under certain irradiation conditions [140, 141, 142] indicating a deterministic and self-induced process. While Bellouard et al. investigated the transition between chaotic and periodic formation [140] a comprehensive explanation of the formation of these micro-bubbles is not yet known. As these structures might impose limitation in the achievable bonding strength, the occurrence of these modifications is investigated and a possible formation mechanism proposed.

4.4.1 Shape and inner structure of laser induced disruptions

The formation of small voids with a volume below $1 \mu\text{m}^3$ in fused silica for strong focusing conditions is well known (see Section 2.3.3). In addition, when using low-NA objectives and low pulse energies large disruptions can be found within the traces of the

molten material, too. In micrographs [see Figure 4.8] these disruptions appear as dark spots with a size of several micrometer within the molten material.

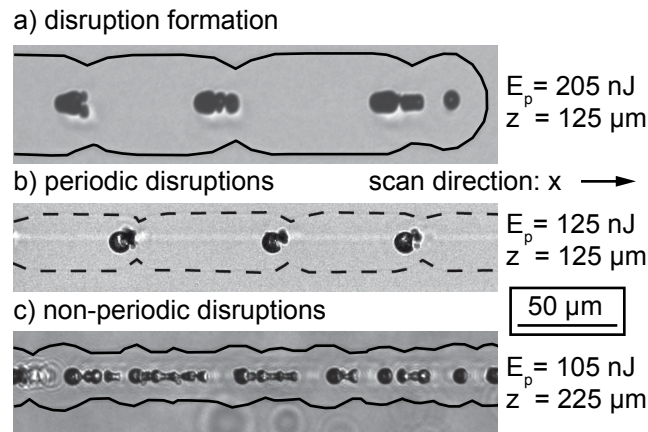


Fig. 4.8: Formation of disruptions within molten fused silica. (a) At the end of the line a disruption is formed, too. The occurrence of disruptions within the molten material occurs either periodically (b) or non-periodically in a chaotic manner (c). The dashed lines retrace the molten region. The applied pulse energies E_p and focusing depth z are listed beside the micrographs (200 mm/min translation velocity, 0.55 NA, 9.4 MHz repetition rate)

Figure 4.8 (a) - (c) show typical micrographs of laser inscribed molten lines in fused silica. The applied pulse energy E_p and focusing depth z are stated beside the pictures. To inscribe the lines the sample was translated along the x axis. For the inscription pulse duration of 450 fs, NA of 0.55, repetition rate of 9.4 MHz and translation velocity of 200 mm/min were used. The molten regions - retraced by dashed lines - possess a width of up to 50 μm . Within each trace of molten material disruptions can be found in different sizes and quantity as dark spots. With the laser system used (Amplitude t-pulse 500) it was not possible to inscribe molten lines without any disruptions. Furthermore, disruptions were always generated at the end of a molten line [an example can be seen at the end of the line in Figure 4.8 (a)] regardless of the irradiation conditions. In agreement with prior publications [140, 141] these so called "pearl-chains" or "micro-bubbles" appear almost periodically with a distance of several tens of μm [Figure 4.8 (b)] or may be close together in a non-periodic manner [Figure 4.8 (c)]. The transition between periodic and non-periodic formation of disruptions depends on the processing parameters. In the measurements periodic formation of disruptions occurs while focusing close to the surface ($\leq 300 \text{ } \mu\text{m}$ below the surface) and using pulse energies $\geq 120 \text{ nJ}$. In this process-

ing regime the distance between two periodic disruptions depends on the applied laser power and translation velocity of the sample. With decreasing laser power the formation of disruptions becomes non-periodically as can be seen in Figure 4.8 (c). When focusing in large depths ($\geq 500 \mu\text{m}$ below the surface) or using higher NA disruptions are formed non-periodically, too. In addition, the adjustment of the focusing optic plays a critical role as misalignment leads to accumulation of disruptions. As can be seen in Figure 4.8 (a) the occurrence of disruptions also affects the width of the molten region. After a disruption is formed the heat affected zone narrows and widens after several μm again. This behavior can be explained by the disruption itself scattering the laser pulses and interrupting the laser heating after its formation. When the scattering object is moved out of the laser focus the absorption process and subsequent melting of the material resumes.

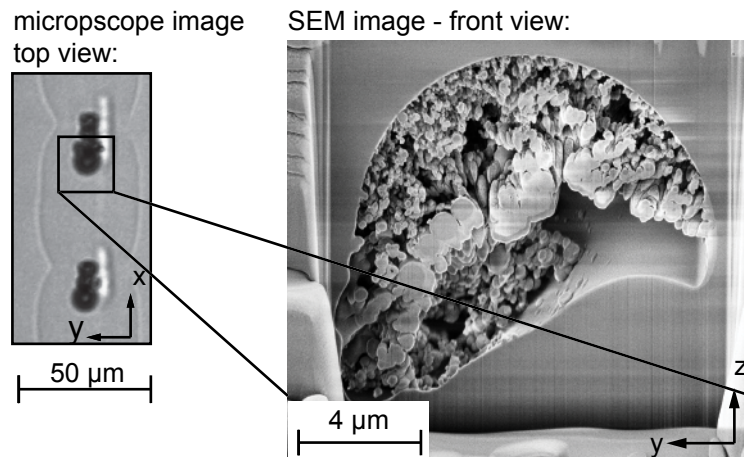


Fig. 4.9: SEM images of the internal structure of a laser induced disruption within the traces of molten material. On the left, the microscope image shows the appropriate modification.

So far, the exact composition of these disruptions was unknown as measurements were limited to their outer boundaries. To resolve this, a commercial Focused Ion Beam (FIB) milling device (Zeiss Neon 60, current 50 pA, accelerating voltage 30 kV) was used to dissect the interior of a disruption. The obtained image of a periodically formed disruption is given in Figure 4.9. For the inscription a repetition rate of 9.4 MHz, pulse energy of 150 nJ, translation velocity of 20 mm/min and focusing NA of 0.55 was used. Focusing depth was 100 μm . The SEM image reveals a very complex structure inside the disruption. In contrast to a simple microexplosion [12, 80, 82] this modification is partially filled with material and simultaneously consists of small cavities in various shapes. The outer boundary of the modifications possesses an almost circular shape with a diameter of about

11.3 μm . The inner modifications exhibit a foam-like structure consisting of solidified material. The structure size of the material within the outer boundary ranges from several hundreds of nm up to two μm .

4.4.2 Model of disruption formation

The results obtained may be used to explain the formation of disruptions within the traces of molten material. The formation of disruptions at the end of a modification trace implies that disruptions appear as consequence of the resolidification process induced by the interruption of the laser heating. The softening point of fused silica is about 1800 K whereas temperatures above 3000 K can be reached easily (see Section 3.2.4) while processing in the heat accumulation regime. On the other hand, the surrounding material exhibits room temperature. In comparison to the small heated zone (about 10^{-4} mm^3) the volume of the cool material is quasi infinite. If the laser heating stops the stated proportions result in a very rapid quenching process, much faster than any other glass cooling process. Consequently, the frozen glass exhibits a higher fictive temperature (see Section 4.3) and appropriate density [86, 143]. Thus, different densities and resulting intensive tensions are induced within the laser irradiated volume [144]. When the heating process stops the solidification front propagates from the outer boundary to the location with the highest temperature which is normally the central region. Rapid quenching of molten fused silica changes the glass network structure, accompanied by a densification of the material [38]. Hence, the material in the outer region is densified by the cooling. Due to the conservation of mass the inner zone undergoes a rarefaction. In addition, the central region exhibits a large accumulation of stress induced by the heating and fast quenching. Fused silica exhibits a very high viscosity of about $10^8 \text{ Pa} \cdot \text{s}$ at $2000 \text{ }^\circ\text{C}$ (e.g. borosilicate glasses have $\approx 10^2 \text{ Pa} \cdot \text{s}$) [145] hindering a complete relaxation of the induced stress and a homogeneous reflow of material in contrast to the mechanisms reported for borosilicate glasses [146]. As a consequence, the central region is not completely filled during the solidification process. This thesis is supported by the structure shown in Figure 4.9.

Disruptions appear also under permanent laser irradiation. In this case, an additional mechanism has to interrupt the laser heating. A possible reason is a self-induced refractive index change due to the increasing temperature. This shift of the refractive index in the processed region induces additional aberrations reducing the peak intensity in the focal region. If the intensity drops below the absorption threshold the laser heating stops and a

disruption is formed. After the quenching the laser irradiates unprocessed material again and the absorption and subsequently melting resumes.

On the contrary, ultrashort pulse processing of glass also decreases the absorption threshold due to the induction of defects and thermally excited electrons (see Section 4.2). Thus, the interruption of the laser heating induced by an index modification will be a competition between a decrease of the intensity distribution and the reduction of the absorption threshold. This proposed formation process is completely different to the well known micro-explosion of small voids [12, 82]. Here, voids are obtained for strong focusing conditions, whereas the formation of disruptions occurs in the heat accumulation regime as a result of a self-induced change of the refractive index.

4.4.3 Simulation of beam propagation inside molten fused silica

In order to obtain an estimation of the effect of self-induced index change by the local temperature increase, the influence of a refractive index change on the intensity distribution in the focal region will be discussed. At first, the influence of different refractive index changes with a maximal Δn of 0.04 induced by a temperature rise within the modified area are investigated. The shape of the refractive index change was assumed to possess a Gaussian distribution along the y and z direction. Along the x direction a constant refractive index change due to the translation of the laser focus was assumed. The size of the modifications was taken from experimental data.

The intensity distribution of ultrashort laser pulses near the focus of the optic used was simulated according to [147]. To this end, a combination of ray-tracing and wave optical propagation as suggested by Stamnes [148] was applied. Ray tracing was conducted to calculate the propagation through the focusing optics up to a reference plane and the subsequent propagation of the optical wave into the focal region was carried out using diffraction theory. Figure 4.10 illustrates the simulation strategy.

The focusing optic (Newport Asphere 5722, NA = 0.55) was modeled in ZEMAX according to the optical design data provided by the manufacture [149]. The exit pupil of the optics provides the z -position of the reference plane which is curved corresponding to a converging spherical wave with the focus at the z -position and the smallest spot radius in the image plane. The deviations from this perfect spherical wave were exported from ZEMAX and added to the phase of the spherical wave at the reference sphere. The wave optical propagation into the focal region was implemented in MATLAB using the

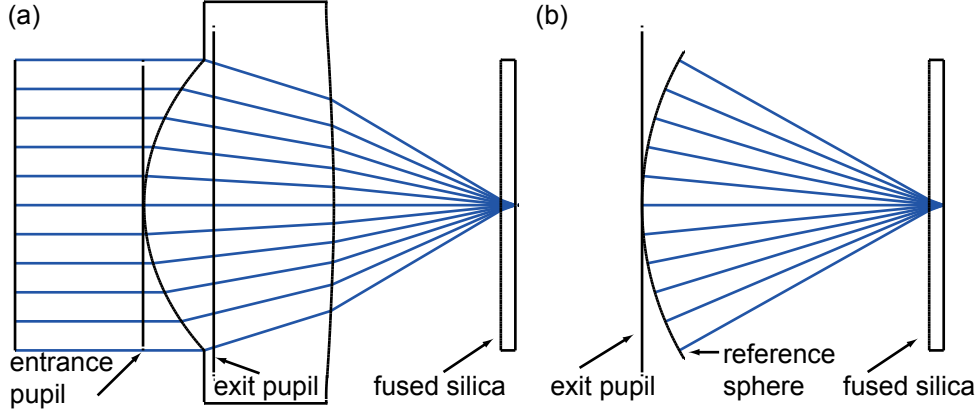


Fig. 4.10: Schematic of the simulation strategy. (a) The focusing optic (Newport Asphere 5722, NA = 0.55) is modeled in ZEMAX to determine the wavefront of the incoming laser-beam at a reference sphere located in the exit pupil of the optics. (b) The optical wave is propagated from the reference sphere into the focal region using the angular spectrum operator.

angular spectrum operator [150]. The propagation of an optical wave at a source plane $U_1(x_1, y_1, 0)$ to an observation plane $U_2(x_2, y_2, z)$ is calculated by

$$U_2(x_2, y_2, z_2) = \mathcal{F}^{-1} \left\{ \mathcal{F} \{U_1(x_1, y_1, z_1)\} H(f_x, f_y) \right\}, \quad (4.1)$$

with the angular spectrum operator

$$H = \exp \left(ik_0 n z \sqrt{1 - \frac{\lambda f_x}{n} - \frac{\lambda f_y}{n}} \right), \quad (4.2)$$

where \mathcal{F} denotes the two-dimensional Fourier transform, \mathcal{F}^{-1} its inverse transform, f_x and f_y the spatial frequency coordinates, k_0 the wave vector in vacuum, n the refractive index, z the propagation distance and λ the central wavelength of the laser pulses. The propagation of the optical wave into the material was carried out by splitting the propagation from the reference sphere to the air-glass interface and from the air-glass interface to the focal region using Equation 4.1 and 4.2 with the respective refractive index. Beam Propagation Method (BPM) was applied to model the Gaussian shaped refractive index modification [151]. The propagation of the optical wave for a discrete step Δz was calculated using Equation 4.1 and 4.2 assuming a homogeneous refractive index distribution. The additional phase shift according to the laser induced refractive index modification was added using

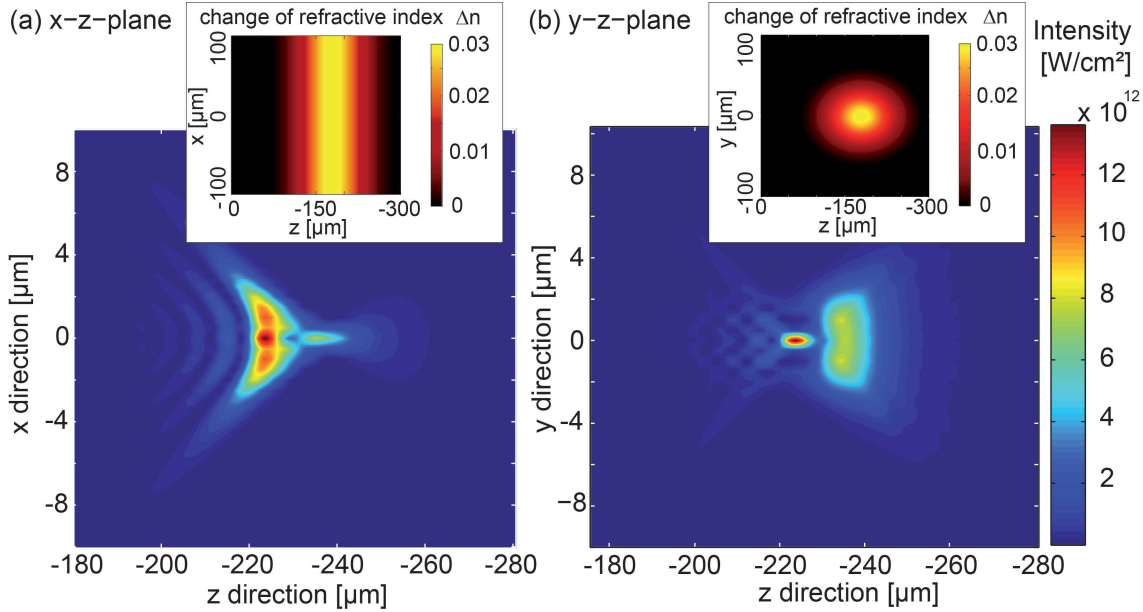


Fig. 4.11: Simulated intensity distribution inside the fused silica sample for a focusing depth of 225 μm in the (a) x-z plane and (b) y-z plane. The insets indicate the area of the laser induced refractive index modification with a length of 93 μm and a width of 50 μm in x. The index modification acts as a cylindric lens focusing the incoming laser beam only in the y-z plane.

$$U_2(x_2, y_2, z_1 + \Delta z) = \mathcal{F}^{-1} \{ \mathcal{F} \{ U_1(x_1, y_1, z_1) \} H(\Delta z) \} \exp \{ i \Delta z k_0 \Delta n(x_1, y_1, z_1) \}. \quad (4.3)$$

For the refractive index modifications different Gaussian distributions were considered according to the experimental results. The temperature at the boundary of a modification is given by the softening point of fused silica (1600 $^{\circ}\text{C}$). For a repetition rate of 9.4 MHz and a pulse energy of 200 nJ a modification size of 92 μm (along the z axis) times 52 μm (along the y axis) was considered. As a start, a central temperature of 3300 $^{\circ}\text{C}$ resulting in a maximal index shift of 0.03 was assumed. This temperature is still below the measured maximal temperature for heat accumulation for a repetition rate of 1 MHz in Borosilicate glass, as shown in Section 3.2.4. As the sample is translated in x direction a constant value along this axis was considered. The respective refractive index changes are shown in the insets of Figure 4.11.

Figure 4.11 shows the calculated intensity distribution for a focusing depth of 225 μm in the x-z plane and y-z plane. The simulations were carried out for the central wavelength of

the laser pulses of 515 nm, a pulse energy of 200 nJ, a pulse duration of 450 fs and a beam waist of 3.5 mm at the entrance pupil of the focusing optic. The index modification acts as a cylindric lens caused by its translation symmetry along the x axis. A distinct focus can only be found in the y-z plane [Figure 4.11 (b)], whereas the intensity distribution in the x-z plane [Figure 4.11 (a)] is broadened and depicts a width of about 2 μm . In addition, the focus is slightly shifted towards the surface due to the focusing action of the Gaussian index modification. This asymmetric focusing leads to a significant drop of the peak intensity along the optical axis. Figure 4.12 shows the intensity distribution along the optical axis ($x=y=0$) with and without different index modifications. Without an index modification (black line) a maximal intensity of $4.5 \cdot 10^{13} \text{ W/cm}^2$ in the focal region is obtained. The existence of even slight index modification leads to a decrease of the maximal intensity by almost a factor of 4. Here, different maximal temperatures T_{Max} were investigated while keeping the length of the respective molten material fixed to 92 μm . With increasing maximal temperature the intensity distribution is reduced. The red line corresponds to a large index modification induced by a maximal temperature rise of 4000 K. This large modification reduces the peak intensity to about 20 %.

But even for a rather low temperature rise of 2000 K (blue line) the peak intensity drops to about 35 % of the initial value. Beside the maximal temperature the shape of the index modification and especially the slope of the refractive index change affects the intensity distribution in the focal region. For the simulations shown in Figure 4.12 (b), a maximal temperature rise of 2000 K ($\Delta n=0.02$) was assumed. Different widths of the modifica-

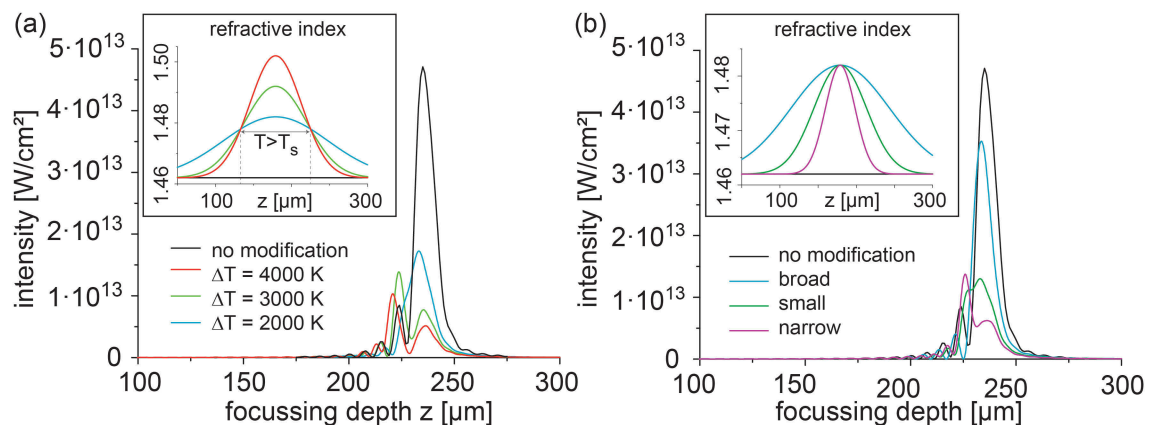


Fig. 4.12: Simulation of the intensity distribution along the optical axis for various index modifications: (a) influence of the maximal refractive index shift; (b) influence of the width of the index modification. The insets show the refractive index modifications considered.

tions were investigated. It can be seen that a broad refractive index distribution (blue line) yields only a reduction to 73 %. Narrower index modifications (red and green line) yield a much higher reduction of the peak intensity. The exact intensity distribution depends on the shape of the refractive index modification. For example the narrow refractive index modification (red line) leads to a slightly higher intensity distribution than the small index modification (green line). The considered refractive index changes are assumptions based on experimental results. However, additional experimental data are required to verify the exact induced refractive index change in fused silica. The temperature distributions obtained by the micro-Raman measurements yield large temperatures of up to 7000 K. However, these results were obtained in Borofloat 33 and with another laser system as used here for the laser bonding of fused silica (see Section 4.1). In addition, for the simulation only the thermally induced refractive index change was considered. Melting of the glass will change the refractive index, too. Nevertheless, the principal trend is obvious. A temperature rise induces a change of the refractive index which is asymmetric due to the translation of the sample. Such an index modification decreases the laser intensity in the focal area. Depending on the exact index modification a reduction of the peak intensity up to 20 % of the initial value is possible. Due to this reduction the laser absorption will decrease or may even interrupt. Consequently, the previously heated focal region will cool down and the nonuniform solidification will lead to the formation of the disruptions as described in Section 4.4.2.

4.4.4 Periodic formation of disruptions

In general, disruptions are adverse for the bonding of glasses as they interrupt the welding seams and consist of damaged and hollow glass. Thus, the amount of disruptions has to be reduced. To this end, the periodic formation of disruptions is investigated and their periodicity with respect to the applied processing parameters is measured. Here, only the periodically formed disruptions were considered neglecting the smaller ones which appear in the vicinity of an initial disruption. The error (standard deviation) of the measured distances lies between 10 % and 20 % decreasing slightly with increasing pulse energy, i.e. the periodicity of the disruptions increases with higher pulse energies. Figure 4.13 (a) shows an increasing distance D_D between two adjacent disruptions with increasing pulse energy E_p . In addition, the distance increases with increasing repetition rate R and thus generally with increasing laser power. Although a higher translation velocity equals a

lower deposited laser power per spot the distance between two disruptions increases with the translation velocity [see Figure 4.13 (b)]. However, the average distance increases only by a factor of 5 while changing the translation velocity from 1 mm/min to 500 mm/min. The highest translation velocity (500 mm/min) yields the largest distance between the disruptions of 92 μm . In a next step, the number of pulses N irradiating the laser sample between two disruptions was calculated, using the formula $N = D_D \cdot R/v$. This means in terms of the proposed model (Section 4.4.2) that N pulses are required to accumulate sufficient aberrations to interrupt the laser absorption and to form a disruption. With increasing pulse energy the number of pulses required to form a disruption increases as shown in Figure 4.13 (c). For slower translation velocities the number of pulses required to form a disruption increases, too.

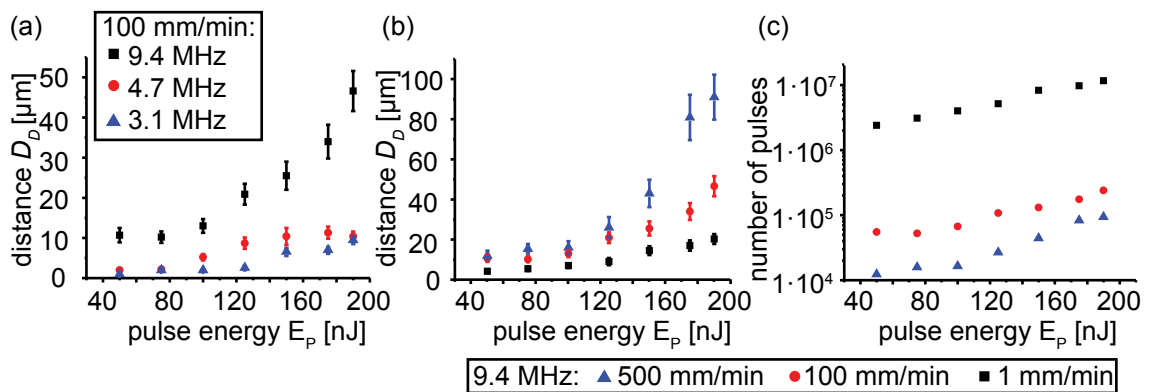


Fig. 4.13: The distance between periodically formed disruptions as a function of the pulse energy for different (a) repetition rates and (b) translation velocities. (c) The number of pulses required to form a disruption with respect to the processing parameters.

These results fit to the proposed model. At large pulse energies larger aberrations are required to decrease the energy density below the threshold, in contrast to low pulse energies. It was also shown in Section 4.4.3 that the shape of the index modification also affects the final peak intensity. An index modification induced by a high translation velocity (e.g. 500 mm/min) is much smaller than for slow translation velocities [31, 126]. In addition, a narrow index modification induces a large reduction of the intensity distribution (see Figure 4.12). Consequently, less pulses are required to form a disruption at higher translation velocities. Thus, generally the number of laser pulses required to form a disruption increases with increasing applied laser power per spot.

To conclude this section, disruptions are a general consequence of the laser induced heat-

ing of fused silica. Due to its large viscosity disruptions can not be avoided so far. In other glasses (e.g. borosilicate) the viscosity of the molten material is lower. Consequently, induced tensions and density gradients may relax and laser induced melting without disruptions is possible. Best processing parameters to induce a minimum number of disruptions are high translation velocities and large average laser powers. The application of high average laser power suppresses the formation of disruptions as more pulse are required to accumulate sufficient aberrations. With increasing laser power the laser induced temperature increases. The temperature of the surrounding material however stays almost constant resulting in a faster quenching process with increasing laser power. This indicates that the amount of induced stress will increase with the average power, too. As stress within a material reduces its stability an optimization between the induction of stress and suppression of disruptions is necessary.

4.5 Laser induced stress

Ultrashort pulse induced modifications are surrounded by large stress fields [144]. The heating of the focal area leads to thermal expansion of the material inducing stress into the surrounding material. In addition, the induced structural changes lead to densifications. Due to the rapid quenching not all of these stress fields can relax. Stress in a transparent material induces birefringence which can be analyzed by polarization contrast microscopy. To analyze the laser induced stress a commercial stress analyzer (Ilis StrainMatic M4/60.13) was used. Within this setup the glass sample is illuminated with linear polarized quasi-monochromatic light (587 nm). The initial linear polarized light is transformed into an elliptical polarization state by passing through the stressed material. With a retarder the optical path difference between waves parallel and perpendicular to the optical axis can be measured. The detected optical path difference ϕ can be converted into normed stress $\Sigma = \phi / (d_m \cdot \beta)$ where d_m is the size of the modified region and β is the photoelastic coefficient of the material ($\beta = 3.6 \text{ TPa}^{-1}$ for fused silica [152]). The error of the measured path difference is 0.1 nm.

Figure 4.14 (a) shows the front view of a molten line and a map of the measured optical path differences. The modification was written with a repetition rate of 9.4 MHz and pulse energy of 200 nJ (NA 0.4, 450 fs). The stress surrounding the modification exhibits a large distribution with a size much larger than the initial modification. The width of the stress

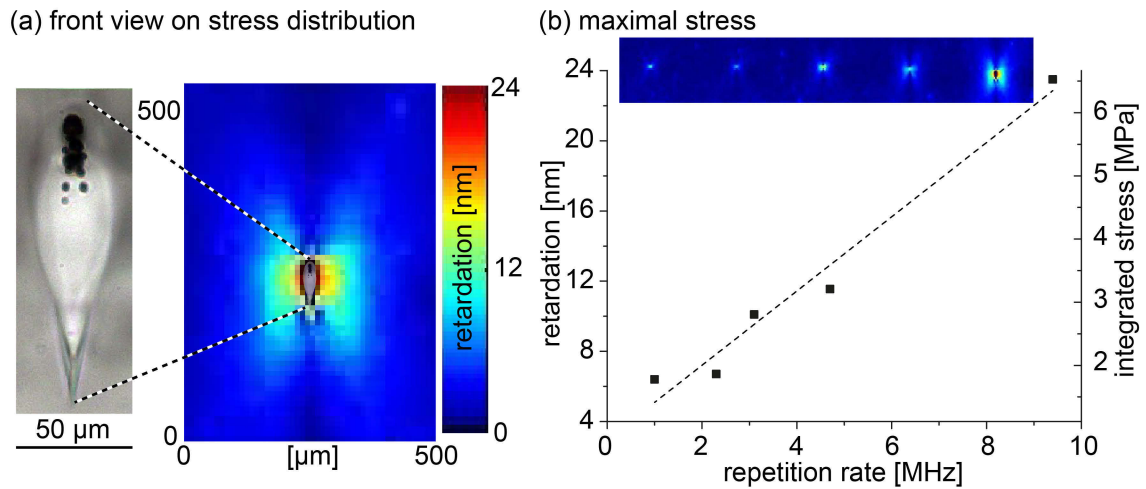


Fig. 4.14: (a) Microscope image of laser induced modification and corresponding stress distribution. Here, the repetition rate was 9.4 MHz (200 nJ, NA 0.4, 450 fs). Focussing depth was 500 μm below the surface. (b) Maximal stress induced retardation and calculated integrated stress for different repetition rates. The insets show the appropriate stress distribution. The written lines have a length of 1 mm (200 nJ, NA 0.4, 450 fs).

field is several tens of μm . Therefore, stress fields can disturb other modifications located in their vicinity [153]. In a next step the maximal optical path difference (i.e. retardation) was measured with respect to the repetition rate [see Figure 4.14 (b)]. To this end, continuous lines with a length of 1 mm were inscribed. The resulting calculated stress is thus an integration of the entire line. The insets in Figure 4.14 (b) show the appropriate stress distributions. In general, the induced stress increases with the repetition rate. The same measurements were conducted for different pulse energies confirming that the induced stress increases with the applied power. To reduce the amount of stress the modification can be annealed [27] as the higher ambient temperatures support the relaxation of stress [42, 154]. For viscoelastic materials the induced stress relaxes for temperatures well below the softening point [27]. To quantify this the stress induced retardation of different modifications in fused silica and borosilicate glass before and after annealing was measured. The modifications had a length of 2 mm and were inscribed using pulse energy of 200 nJ and repetition rate of 9.4 MHz (450 fs, 515 nm). For the annealing a furnace with a controllable heating and cooling rate (200 K/h) was used. The annealing temperature was kept constant for 2 h for each sample.

Figure 4.15 shows a decreasing retardation with increasing annealing temperature for both glasses. After 2 hours at 600 $^{\circ}\text{C}$ the stress induced retardation in fused silica was re-

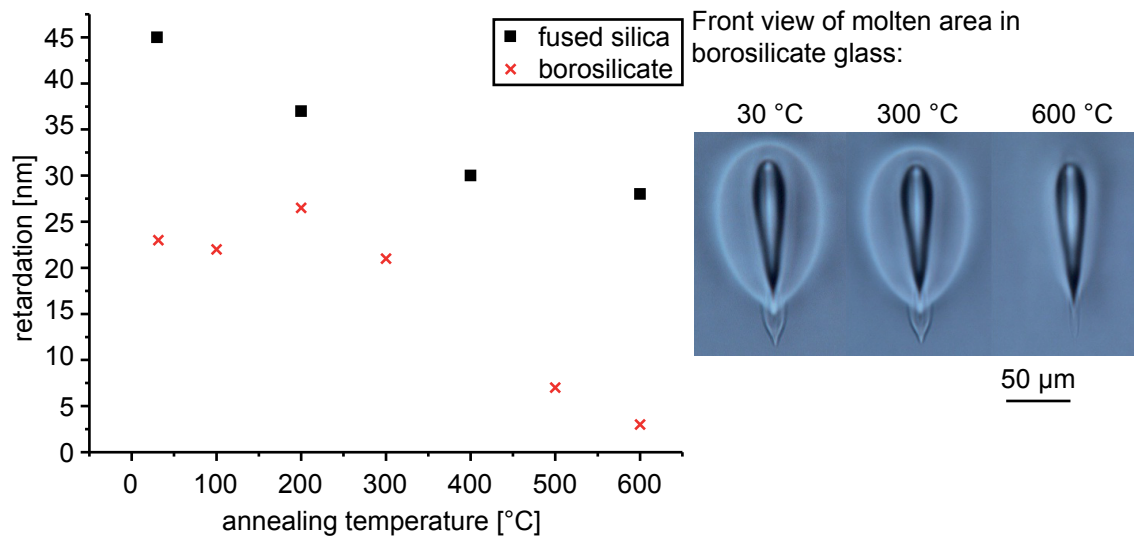


Fig. 4.15: Retardation of stress induced birefringence in laser processed fused silica and borosilicate samples after annealing for two hours at a certain annealing temperature. Corresponding microscope images of the molten area in borosilicate glass are shown on the right. The inscribed modifications had a length of 3 mm and were inscribed using a pulse energy of 200 nJ and repetition rate of 9.4 MHz.

duced from initially 45 nm to 28 nm. In general, the measured retardation in borosilicate is much lower than in fused silica, e.g. without annealing the stress induced retardation in borosilicate is only 23 nm whereas fused silica yields almost twice that value (45 nm). The difference in the induced stress values can be explained by the different viscosity of the glasses. The lower viscosity of borosilicate glass facilitates an increased relaxation of laser induced stress during the quenching of the glass. In addition, the annealing point of borosilicate glass is at 560 °C (see Table 2.1). At this stress-relief point the glass is not yet deformed but internal stress can relax completely within several minutes. Consequently, after annealing at 600 °C the retardation in borosilicate glass is almost zero. On the right of Figure 4.15 corresponding microscope images of non-annealed and annealed modifications in borosilicate glass are shown. The laser induced modification appears unaltered for an annealing temperature of 300 °C. However, after heating to 600 °C the external region is completely vanished leaving only the internal region which is connected with a much higher processing temperature [25, 27].

In general, post-processing annealing can be utilized to reduce the laser induced stress and strengthen the welding seams between the sample. Annealing is also a well known technique to strengthen the bonds after optical contacting. Here, the initial van-der-Waals

bonds are transformed into covalent bonds resulting in larger bonding strengths [32]. However, due to the heating of the entire sample this technique is limited to samples with almost the same thermal expansion coefficient.

5 Direct Laser Bonding of fused silica

The final two chapters deal with the laser bonding of transparent materials. In this chapter the bonding of fused silica is investigated. After a brief description of the experimental approach the setup to determine the breaking strength is presented. With the three point bending test, the influence of the welding geometry is investigated. Afterwards two possibilities to enhance the breaking strength are explained. Finally, fracture mechanical material properties of laser bonded fused silica are determined with a Chevron Notch test.

5.1 Experimental approach

Tamaki et al. demonstrated the general possibility to bond glasses with high repetition rate laser systems [23, 30]. First measurements of laser bonded glass were conducted with a tensile test yielding a bonding strength of about 10 MPa for non alkali glasses [24]. For Foturan and borosilicate glass it was shown that the stability of bonded glasses can be significantly enhanced by laser welding with ps-pulses in comparison to optically contacted samples [25, 29, 117]. In their experiments, a shear test was used to determine an increase of the shear strength of about 55 MPa for laser bonded borosilicate glass [117]. In addition, Hélie et al. presented similar results when using filaments of ultrashort laser pulses instead of heat accumulation [94, 155]. In most of these experiments, shear tests were applied which are difficult to compare to the bulk material. In addition multiple different glasses were investigated. Thus, the achievable bonding strength with respect to the bonding parameters are unknown. In the subsequent study fused silica was used as it is the most pristine glass and results obtained here can be assigned to other glasses, too.

For all the results presented here a femtosecond oscillator providing pulses at a wavelength of 1030 nm, repetition rate of 9.4 MHz, an average output power of 5 W and pulse duration of 450 fs (Amplitude Systems, t-Pulse 500) was utilized. The repetition rate and pulse energy were varied by an external acousto-optic modulator and a halfwave

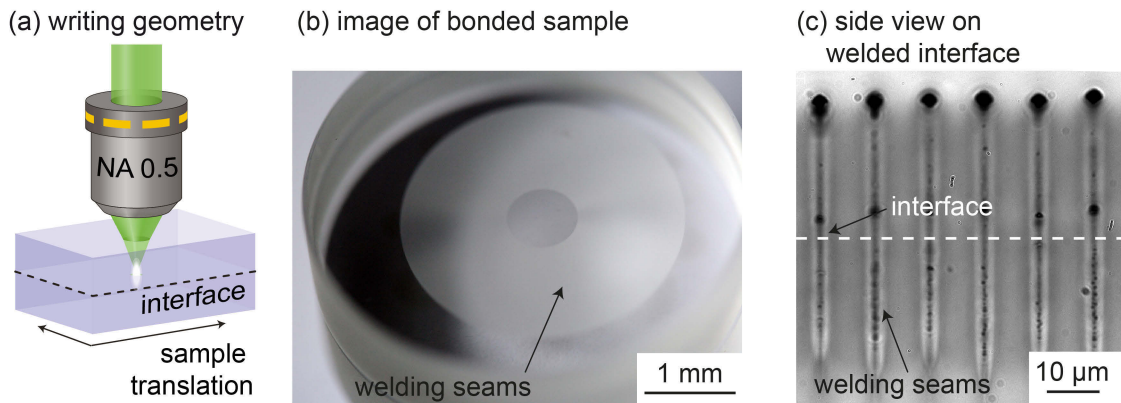


Fig. 5.1: (a) Writing geometry (b) Image of two laser bonded circular blanks of fused silica. (c) Side view on the welding seams located in the interface of two glass samples.

plate followed by a polarizer, respectively. For all experiments an LBO crystal was used to generate the second harmonic (515 nm). Commercially available fused silica circular blanks (Hellma Optics) with a diameter of 50 mm and a thicknesses of 6 mm were used as glass samples. As the height of the molten and ejected material is only in the range of a few hundred nanometer [31] the samples were optically contacted before the laser welding process. Optical contacting requires a sample roughness of 2 nm and a flatness below 125 nm. Alternatively, the samples can be pressed together as shown by Tamaki et al. [24]. However, this induces a large amount of stress and reduces the stability of the bonded samples. The laser pulses were focused with an aspheric lens (NA of 0.5) through the upper sample, as shown in Figure 5.1 (a). The focal spot was placed slightly below the interface. By using a positioning system the samples were translated with respect to the laser focus to inscribe continuous welding seams.

Figure 5.1 (b) shows an image of two laser bonded samples. The white circular lines are the weldings seams, separated by a distance of 10 μm . The existence of the welding seams locally reduce the transparency of the bonded sample. However, the inner region remains unaffected. A side view of the welded interface is shown in Figure 5.1 (c). The large focusing depth results in spherical aberration leading to an enlarged laser focus. Consequently, the induced modifications are elongated and narrower than reported in Chapter 3 at which the focusing depth was about 100 μm below the surface. Here, a pulse energy of 200 nJ and a repetition rate of 9.4 MHz was used, leading to a width of a welding seam of about 6 μm . The dark spots within the welding seams are disruptions (see Section 4.4). The large disruption atop of a modification is much bigger than the smaller ones within the entire

modification, whose size is small in comparison to the width of the molten material. Thus, the interface (white dashed line) has to be located within the welding seams, to minimize the influence of a disruption and maximize the size of the molten material. By varying the distance between the welding seams different fractions of the interface can be molten resulting in different bonding strengths. In the following sections, the achievable breaking strengths with respect to the processing parameters are investigated.

5.2 Measurement of bonding strength

For the analysis of the stability of bonded samples different tests are usually used. To determine the breaking strength of bonded silicon samples, typically a blade test is used [28]. Here, a blade is inserted at the interface and the size of the disjoined area is measured. However, this test is unsuitable for only partially bonded samples. Furthermore, even small variations of the measured size lead to high fluctuations of the results. Some groups use shear [29, 30, 31] or tensile tests [24, 156]. All of these tests are difficult to compare and normally no conversion between the different results is possible [33]. Tamaki et al. conducted a tensile test of laser bonded non-alkali glass measuring a joint strength of ≈ 10 MPa. Wu et al. determined a slightly higher value of ≈ 13 MPa for laser bonded Foturan. However, a comparison to the value of the bulk material was not possible. To overcome this drawback, a three-point bending test was used in this work.

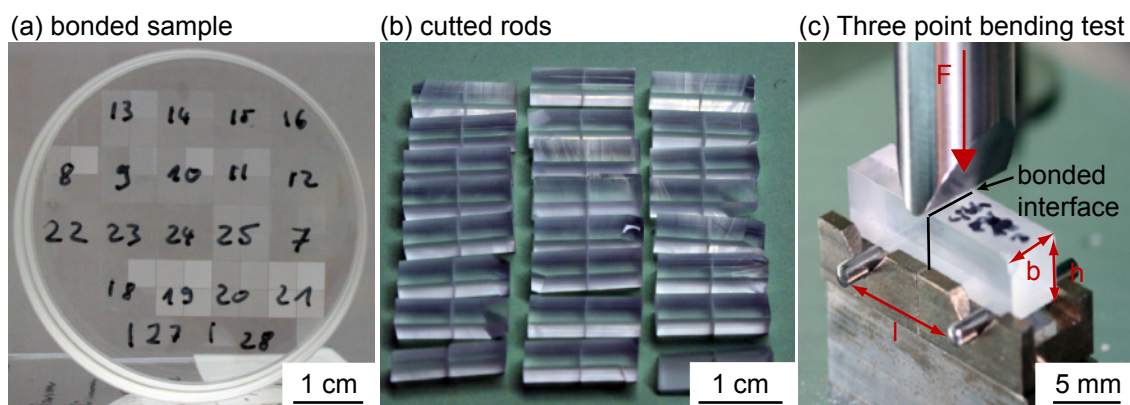


Fig. 5.2: Principle process for the measurement of the bonding strength. At first different areas of the samples were bonded using various processing parameters. (a), afterwards the sample was cut into rectangular rods (b) and finally a three point bending test applied to determine the breaking strength of the samples (c).

After the welding process [see Figure 5.2 (a)], the circular blanks were cut into rectangular rods with defined dimensions [see Figure 5.2 (b)]. In a next step, the bonded interface is placed at the center between two bearings directly below the stress pin applying a defined force F . The influence of a possible displacement ($\pm 0.25 \mu\text{m}$) to the total error is much smaller than the described issues below. However, each set of parameters were used several times (at least five) to estimate mean value and standard deviation. The breaking strength σ can be calculated from the force F required to break the bonded samples apart

$$\sigma = \frac{3 F l}{2 b h^2} \quad (5.1)$$

where b and h refer to the edge lengths of the sample cross section and l is the distance between the two bearings [157]. A picture of this three point bending test is shown in Figure 5.2 (c). For these measurements, the predominant sources of error are defects and scratches along the outer surface of the rod, induced during the cutting process. At these scratches the local stress is increased, leading to a fracture of the sample. Thus, the quality of the sawing blade influences the result of the three point bending test. In general, the quality of the surface can be enhanced by polishing the sample, reducing the amount of cracks on the surface. Accordingly, the measured breaking strength of the sample investigated is increased, see Figure 5.3. Here, fused silica samples were bonded and the breaking strength was measured with and without polishing. In addition, the breaking strength of pristine bulk material was determined. For unpolished samples, laser bonded samples

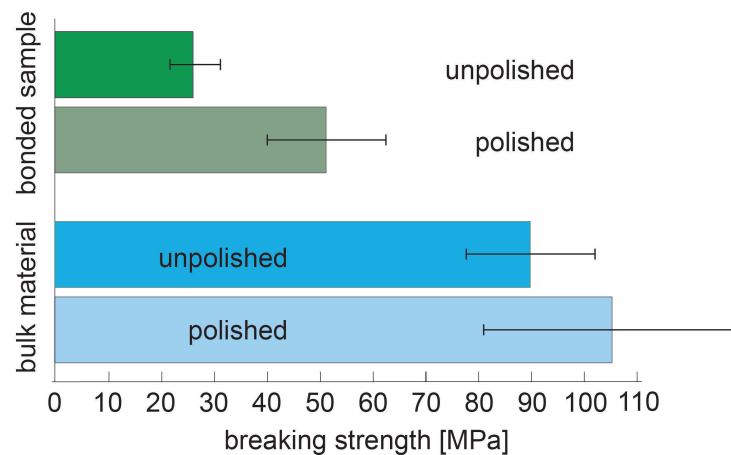


Fig. 5.3: Breaking strength of unpolished and polished samples. At least five samples were used for each set of parameters.

yield a lower relative error (standard deviation) of the measurement, as the original interface act as predetermined fracture zone. In general, the positive effect of the polishing on the breaking strength for laser bonded as well as for bulk material can be seen. For example, the breaking strength increases from 90 MPa without polishing to 106 MPa for the bulk material. Due to its large technical and temporal effort, polishing was applied only exemplary for these few samples. In order to exclude the influence of the quality of the sawing blade, for each experiment the average breaking strength of the bulk material was determined (at least 10 samples were used). The measured average breaking strength for different glasses are given in Table 5.1.

Tab. 5.1: Breaking strength of the pristine bulk glass utilized measured by a three point bending test.

material	bulk breaking strength σ [MPa]
Fused silica	92 \pm 13
Borosilicate	113 \pm 15
BK7	40 \pm 4
ULE	94 \pm 14
Zerodur	164 \pm 30

5.3 Laser Bonding of fused silica

It was already shown in Section 3.2.4 the size of the molten region depends on the laser parameters. In general, the size of the molten material increases with applied laser power. Due to aberrations, the focusing depth also affects the shape of the molten volume [158], leading to an elongation. In the experiments a translation velocity of 200 mm/min was used to reduce the processing time and the amount of disruptions (Section 4.4). At first, the influence of the amount of molten material on the breaking strength was investigated. To this end, multiple samples were laser bonded with varying distances of the welding seams as well as different laser powers.

The measured breaking strength increases with increasing size of the molten area, as shown in Figure 5.4. For continuous welding seams (black curve), at first the breaking strength increases linearly and eventually saturates at a maximal value of 25 MPa. This is about 40 % of the breaking strength of bulk fused silica (in this cycle a breaking strength of 70 MPa was measured for pristine bulk fused silica). On the contrary, single welding spots

offer a much higher value, see the red curve in Figure 5.4. Here, a maximum breaking strength of 54 MPa was reached, which is about 75 % of the bulk material.

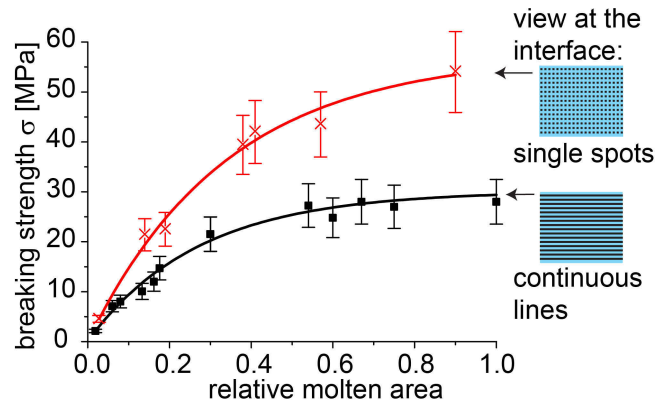


Fig. 5.4: Dependence of the breaking strength on the amount of the molten area using different welding geometries. The molten area was normalized to the interface.

To understand this, one has to consider the crack formation within the fracture plane and the surface energy required for the crack propagation. On the one hand, the molten lines establish strong bonds between the glass samples but on the other hand they act as predetermined fracture points as they induce stress into the material (Section 4.5). If these lines are continuous only a small amount of surface energy has to be provided for an initial crack to propagate along the whole line. While using single welding spots, the interface between molten and non-molten material maximized. Each of these interfaces form a resistance to the crack propagation and thus a higher surface energy to fracture the whole interface is required. The achieved maximal breaking strength is in very good agreement with measurements in which bulk material was structured with the same processing parameters as for the laser bonding. In this case, the breaking strength of the bulk glass is reduced from initially 70 MPa to 58 MPa, almost identical to the maximum value obtained for the bonded samples.

To explain the fact that the breaking strength is limited to approximately 75 % of the bulk material, the fractured surfaces were analyzed. If less than 50 % of the entire interface is molten, a linear dependence between the breaking strength and molten material is observed. Here, the crack propagates directly at the original interface. This can be seen in microscope or SEM images, e.g. see Figure 5.5 (a). Here, the remnants of the molten material which resides at the ripped interface are clearly visible. These segments occur either as bulges or as shallow holes with a height of about 200 nm.

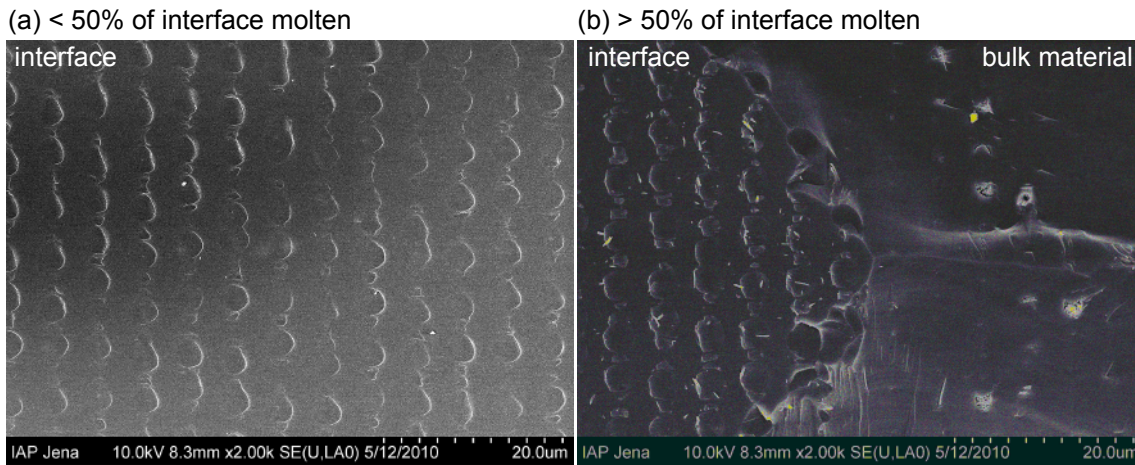


Fig. 5.5: SEM image of the fractured samples for a different fraction of molten interface.

Starting with a surface coverage of about 50 % the crack rather propagates in the surrounding material than along the original interface. The new fracture plane has a distance of several micrometers to the original interface. In Figure 5.5 (b) the change in the fracture plane from the interface into the material can be seen. The different fracture behavior can be explained by the laser induced stress and the degradation of the glass induced by the disruptions. If the distance between the molten zones is small enough the stress fields may overlap and form a predetermined fracture plane. In addition, the disruptions act as non-bonded or material defect, favoring the crack propagation at their position. Due to the laser induced bonds between the samples, the interface is no longer the preferred plane for the crack propagation. Instead of this, a plane along the stress fields acts now as fracture plane, limiting the achievable breaking strength.

In the following, two possibilities to reduce the amount of stress and further increase the breaking stability of bonded fused silica samples are presented.

5.4 Tailored energy deposition

A repetition rate of about 1 MHz is required to achieve sufficient heat accumulation for the melting of fused silica. A further increase of the repetition rate induces a larger molten area but it also involves much higher temperatures, causing larger stress. Thus, a tailored energy deposition is required to achieve a temperature above the softening point while simultaneously minimizing the induced stress. To this end, the high repetition laser source

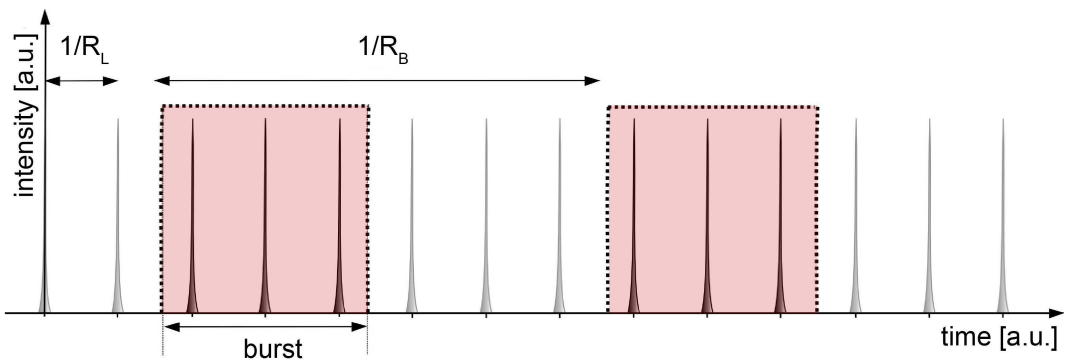


Fig. 5.6: An acousto-optic modulator can be used to pick a defined number of pulses from a continuous pulse train, which has a repetition rate of R_L . This generates bursts of femtosecond laser pulses with a burst repetition rate of R_B .

was combined with an acousto-optic modulator (AOM). The AOM allows to select single or even multiple pulses from a continuous pulse train. Thereby the number of pulses within a so-called burst was varied from 1 to 39 each of them having a temporal separation of ≈ 100 ns according to the 9.4 MHz repetition rate of the laser. The burst repetition rate R_B was adjusted by dividing the laser repetition rate ($R_L=9.4$ MHz) by integer values. Figure 5.6 illustrates the different repetition rates.

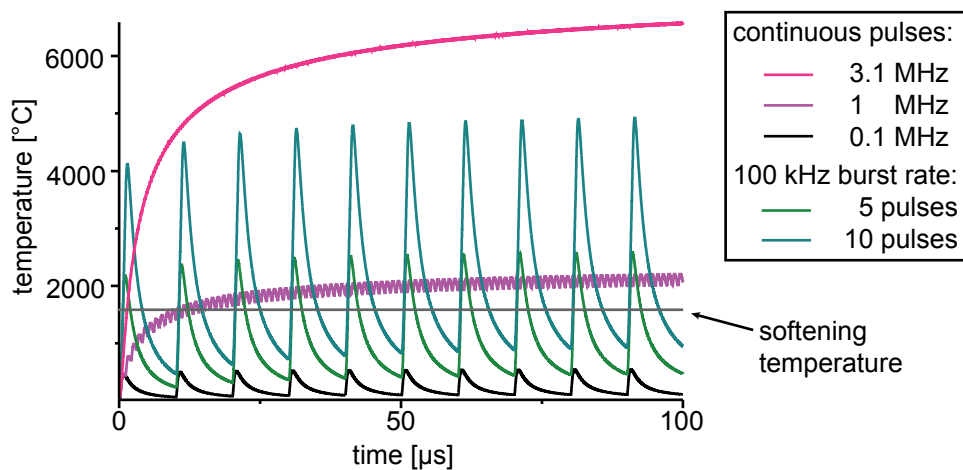


Fig. 5.7: Simulation of laser induced temperature for continuous pulse trains at different repetition rates and for laser bursts with a burst repetition rate of 100 kHz. The single pulse energy was set to 200 nJ.

To analyze the consequence of a modified heating regime a finite difference heat diffusion model analogue to Section 3.1.2 has been used. Again, a temperature dependent thermal conductivity $\kappa(T) = [1/\kappa_0 + bT]^{-1}$ was included in the model with parameters as determined in Section 3.1.2. Figure 5.7 shows the glass temperature $2\ \mu\text{m}$ from the center of absorption (radial distance, $z=0$) for continuous pulse trains as well as for bursts with a burst repetition rate of $R_B = 100\ \text{kHz}$ and various number of pulses within a burst. The laser pulse energy was $200\ \text{nJ}$. For a continuous pulse train, to exceed the softening point (dashed gray line) of fused silica a repetition rates of at least $1\ \text{MHz}$ is required. With increasing repetition rate the temperature increases and the material stays at very high temperatures for almost the complete irradiation time. In comparison to that, the temperature for bursts with five or ten pulses (green curves) drops below the softening point after each laser burst. However, the temperature of the processed material exceeds the softening point for several μs due to the high repetition rate of the pulses within a burst. As the temperature profile indicates, the temporal heat distribution as well as the maximum temperature strongly changes when using bursts instead of continuous pulse trains. This influences the dimensions of heat affected zones as well as the induced stress and consequently the breaking strength of bonded samples.

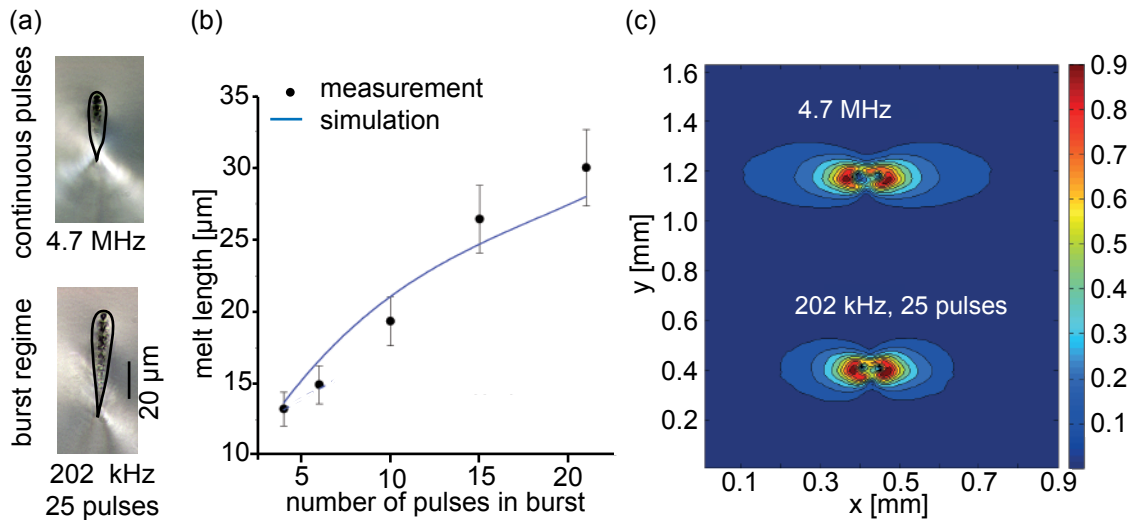


Fig. 5.8: (a) Front view of induced modifications using a constant repetition rate and bursts. (b) Measured and calculated length of the modifications with respect to the number of laser pulses within a burst ($R_B=202\ \text{kHz}$). (c) Micrography of the measured stress fields surrounding the modifications induced by a continuous pulse train and laser bursts. The optical path difference was normalized to its maximal value. For all experiments, the single pulse energy was $200\ \text{nJ}$.

In a next step the size of the molten volume was analyzed while using bursts. The width of the molten material is comparable to the resulting modifications for a continuous pulse train, as can be seen in the micrographs of Figure 5.8 (a). In contrast, the length of a burst induced modification is longer than for continuous pulse trains, while using the same average power, e.g. the length of the modified area induced by bursts with 202 kHz and 25 pulses within a burst, is about 50 % larger than the size induced by a constant repetition rate of 4.7 MHz. In addition, the length of a modification in the burst regime depends on the number of pulses within a burst. Figure 5.8 (b) shows the measured (points) length of a burst induced modification with respect to the number of pulses within a burst. The burst repetition rate was 202 kHz. The measured data is in excellent agreement with the simulations (blue curve) based on Section 3.1.2. The results indicate a growing melt length with increasing number of laser pulses numbers within a burst. This can be explained by increasing heat accumulation with increasing pulse number. By increasing the number of pulses within the bursts the laser repetition rate (9.4 MHz) becomes dominant compared to the burst repetition rate. Hence, the focal region is heated more and subsequently the size of the heat affected zones is increased. However, the width of the molten area remains almost independent of the numbers of pulses within a burst. Here, an increase of the width might be reduced due to the dominant constriction effect of the large aberrations. Thus, the burst induced modifications are mainly elongated.

The application of bursts instead of continuous pulse trains is very interesting with respect to the laser induced stress. As shown in Section 4.5 the applied average power defines the amount of induced stress. Thus, the amount of laser induced stress can be reduced by choosing a burst regime with low average power (e.g. low R_B), whereas the small temporal separation of the pulses within a burst still lead to heat accumulation and melting of the material. In addition, the size of an induced modification determines the distribution of the surrounding stress fields. As shown in Figure 5.8 (b), the burst induced modification yields a much narrower stress distribution than the one obtained with a constant repetition rate, which is most likely caused by the elongation of the modified zone.

Finally, the breaking strength was measured when using bursts of laser pulses. A burst repetition rate of 100 kHz was chosen. Here, still a considerable amount of material is molten while the amount of induced stress is small in comparison to a repetition rate of 4.7 MHz. Different pulse energies, pulse numbers and line distances were chosen to melt different fractions of the interface. After the three point bending test the interfaces of the samples were analyzed to determine the amount of molten material. Figure 5.9 shows the

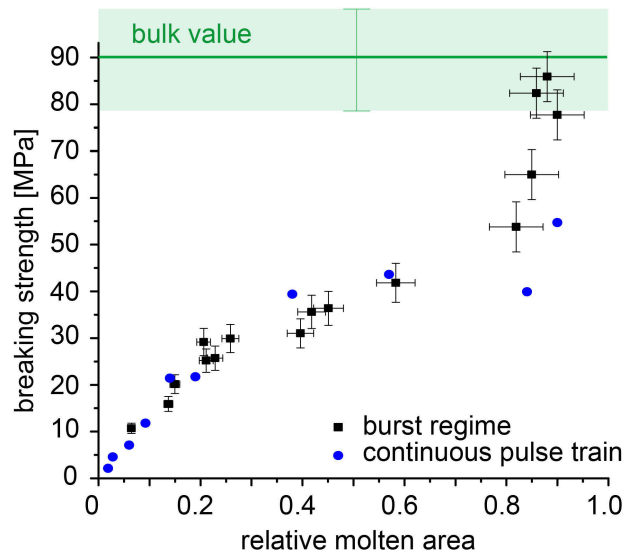


Fig. 5.9: Breaking strength obtained when using continuous pulse trains or bursts of laser pulses with respect to the relative molten area.

measured breaking strength with respect to the relative molten area. For a better clarity of the figure, the error bars are shown only for the burst measurements. The error corresponding to the continuous pulse train measurements is in the range of 15% for each data point. For continuous pulse trains (blue points), a maximal bonding strength of about 50 % of the bulk material was achieved. Here, the best results were obtained, while using a repetition rate of 4.7 MHz (instead of 9.4 MHz). In agreement to Section 5.3, the saturation of the breaking strength for a molten area larger than 0.5 can be seen. In contrast, the application of bursts (black rectangulars) yields a maximal breaking strength of 88 MPa, which is comparable the bulk material. This is the highest value of laser bonded glass reported so far. Here, the best results were obtained while using 35 laser pulses per laser burst. Although there is a lack of data points for a molten area between 0.6 and 0.8, no significant saturation of the breaking strength can be observed. In addition, images of the broken interfaces show that the samples bonded with bursts are fractured mainly along the original interface. These results confirm the stress induced birefringence measurements. An increase of the applied average power leads to a rising stress, reducing the breaking strength of the sample. Consequently, welding with a constant repetition rate of 9.4 MHz yields lower values than at 4.7 MHz. When using bursts, the induced stress is reduced and the width of the stress fields is smaller. Thus, the overlap of the stress fields

is reduced, leaving the original interface as predetermined fracture plane. Therefore, no saturation-effect is obtained and large breaking strengths can be obtained.

5.5 Annealing

Another possibility to reduce the laser induced stress is annealing. As shown in Section 4.5, the induced stress can be reduced to about 66 % of the initial value by annealing for 2 hours at 600 °C. However, a thermal treatment of samples is only possible if the same materials or materials with similar thermal expansion coefficients are bonded. Otherwise, the different expansion of the samples during the annealing induces large stress at their interface, leading to a reduced stability or even fracturing of the samples.

To demonstrate the advantage of a post-processing annealing step, the breaking strength of laser bonded fused silica samples without and with an annealing step was measured. Heating and cooling rate was 100 K/h and the annealing time was 2 hours for each sample. Initially, all the samples were bonded with a repetition rate of 4.7 MHz, a pulse energy of 200 nJ and a translation velocity of 100 mm/min. In this cycle, the bulk material depicts a breaking strength of 90 ± 10 MPa. Without annealing the average breaking strength was 26 MPa. With increasing annealing temperature the breaking strength increases, as can be seen in Figure 5.10. Annealing to 1000 °C (which is the maximal temperature of the furnace used) yield a breaking strength of about 60 MPa, which is more than twice the

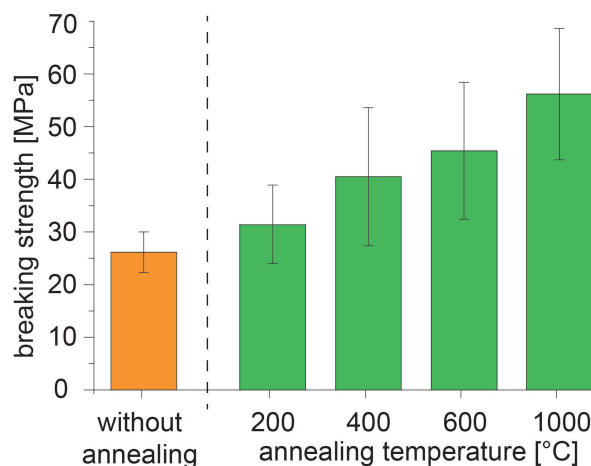


Fig. 5.10: Breaking strength of laser bonded fused silica after an additional annealing step. For comparison, the breaking strength of a only laser bonded and non-annealed sample is shown, too.

initial breaking strength. Since the annealing point of fused silica is 1080 °C annealing at this temperature or an increase of the annealing time can even further increase the breaking strength.

5.6 Chevron Notch Test

The results presented so far were obtained using a three point bending test. With this measurement the breaking strength of the bonded sample can be determined, whereas no information about the material properties as used in material science are obtained. In addition, if the fracturing of the sample occurs in the material and not at the original interface the three point bending test measures rather the stability of the surrounding material than the stability of the bonded interface.

One important material property is the fracture toughness K_{1C} , describing the resistance of a material against the propagation of an already existing crack [159]. Thus, if K_{1C} and the length l_D of a material defect (e.g. a crack) are known, the required stress σ_c to completely fracture the material can be calculated: $\sigma_c = K_{1C} / \sqrt{l_D}$ [160]. The fracture toughness of bulk fused silica is $K_{1C} \approx 0.8 \text{ MPa} \sqrt{\text{m}}$ [159, 161]. In addition, for isotropic materials the fracture surface energy γ_f , indicating the energy required to disrupt the intermolecular bonds of a material to generate a new surface, can be calculated from the fracture toughness [161]:

$$\gamma_f = \frac{K_{1C}^2 (1 - \nu_p^2)}{2 \cdot E} \quad (5.2)$$

with ν_p the Poisson's ratio (0.17 for fused silica) and E the Young's elastic modulus of the material. The fracture surface energy of fused silica was determined to 4.42 J/m^2 [159]. One possibility to measure the fracture toughness of laser bonded glass is the application of a Chevron Notch (CN) test [98, 162]. The design of a Chevron Notch test is shown in Figure 5.11. Instead of completely bonding the samples a chevron pattern with a special designed chevron notch angle is bonded. To perform the test special studs are glued onto the non-bonded edges of the samples. Subsequently a tensile load can be applied until the samples are torn apart.

The advantage of a CN-test is the formation of a sharp crack with a well defined length. The crack starts at the chevron tip, due to its high local stress concentration. With increasing force the crack length and width increases, exhibiting a stable growth. A complete

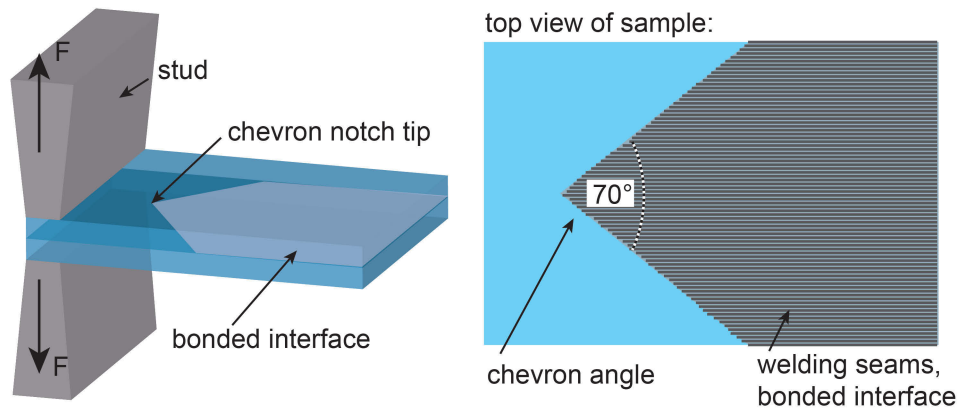


Fig. 5.11: Sketch of Micro-Chevron Test. The bonded interface exhibits a special design with a Chevron angle of 70° .

fracture of the sample is hindered by an increasing bond front, due to the Chevron pattern. After reaching a critical length the crack propagation becomes chaotic, which fractures the samples. The critical length of the crack corresponds to the maximum applied force F_{Max} and depends only on the geometry of the sample and the chevron pattern and is independent on material parameters. Hence, to calculate the fracture toughness only F_{Max} is required [163, 164]:

$$K_{1C} = Y^* F_{Max} \quad (5.3)$$

The factor Y^* is a geometric parameter and can be calculated by FEM simulations [99].

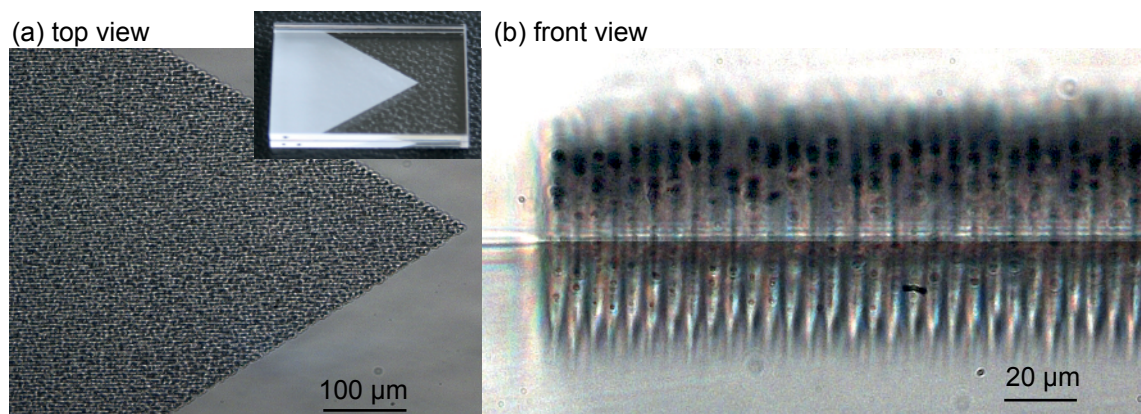


Fig. 5.12: (a) Top view on laser bonded Chevron Notch samples. Here, the Chevron angle is 70° . (b) Front view on the laser inscribed welding seams, exhibiting a distance of $5 \mu\text{m}$. The dark spots within the modifications are disruptions.

To determine the fracture toughness of laser bonded fused silica samples 16 identical samples were tested. The Chevron pattern of the laser bonded samples is shown in Figure 5.12 (a). After preliminary investigations a Chevron angle of 70° was chosen. The sample size was $15 \times 20 \text{ mm}^2$. In order to bond the entire interface [see Figure 5.12 (b)] a line distance of $5 \mu\text{m}$ was chosen. The pulse energy was 200 nJ at a repetition rate of 4.7 MHz. When conducting a three point bending test, these processing parameters yield a breaking strength of about 50 % of the bulk material (see Figure 5.9). However, the focussing depths for these two tests are different and thus the resulting stability values will differ. Figure 5.12 (b) shows that the induced disruptions (black spots) are mainly located in the upper part of the modifications without disturbing the bonded interface. The force F_{Max} measured by the Chevron Notch test ($43.3 \pm 15.6 \text{ N}$) exhibits a large variation, which is non-typically for a CN test.

For brittle materials the maximal load required for a failure may vary due to defects within the samples, at which failure processes originate. Thus, a failure parameter (e.g. the fracture toughness) is best represented by a probability distribution rather than one exact value. Hélie et al. used a Weibull distribution to demonstrate that laser bonded samples exhibit a higher shear strength than samples which were only optically contacted [94, 155]. Especially for brittle materials, the failure probability is commonly described with such a Weibull distribution [155]:

$$F(x) = 1 - \exp\left(\frac{-x}{\eta}\right)^k, \quad (5.4)$$

with the Weibull parameters η (scale parameter) and k (shape parameter). A Weibull distribution expresses the cumulative failure probability of the samples investigated. Thus, the failure probability can be estimated for a required fracture toughness from the Chevron Notch tests. The mean fracture toughness at failure ϕ (corresponding to the expectation value ϕ) can be calculated from a Weibull distribution as:

$$\phi = \eta \Gamma\left(1 + \frac{1}{k}\right), \quad (5.5)$$

where Γ denotes the Gamma function. Figure 5.13 shows the Weibull plot of the Chevron Notch measurements of the laser bonded samples. The mean fracture toughness at failure of $0.912 \text{ MPa } \sqrt{\text{m}}$ is even slightly higher than the bulk material value ($0.8 \text{ MPa } \sqrt{\text{m}}$ [159, 161]). The shape parameter k of the Weibull distribution is 2.27. For technical de-

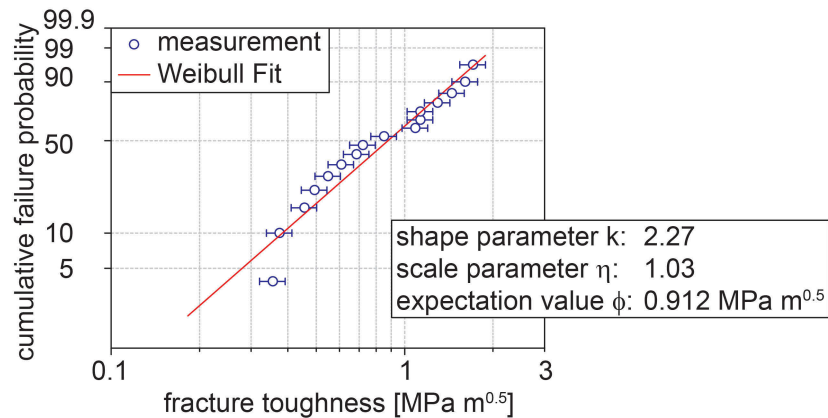


Fig. 5.13: Weibull plot of Chevron Notch measurements of laser bonded fused silica samples.

vices with different failure reasons Weibull distributions with a shape parameter $k \geq 1$ are favored as this indicates a failure characteristic due to exhaustion or aging of the device and a homogeneous distribution of defects within the samples [155, 165]. However, a large variation of the fracture toughness can be seen, too. In addition, within most experiments the entire sample fractured before the interface was torn apart indicating that the bonded interface exhibits a higher surface energy than the surrounding material. This points towards a degradation of the surrounding material during the laser welding process as discussed in Section 5.3. As the fracture occurred always for values close to the critical length, the appropriate fracture toughness can be treated as lowest limit of the bonded interface, explaining the difference of the measurements from an ideal Weibull distribution. Furthermore, the often very high fracture toughness can be attributed to the laser treatment, too. It was shown by Miyamoto et al. [25] that laser treatment of glass can even increase its stability by the induction of compressive stress. Thus, the large variation is a superposition between the induction of defects and stress in the surrounding material and additional internal stress.

The Chevron Notch tests have proven that fracture toughness and fracture surface energy ($\approx 5.57 \text{ J/m}^2$) of laser bonded fused silica are comparable to the values of the pristine bulk material. However, the laser bonding degrades the surrounding material especially by the induction of stress. This limits the overall breaking strength of the bonded samples, although the weakest material is not the welding seam itself but the surrounding material.

6 Bonding of different materials

In this final chapter, the bonding results using different transparent and even opaque materials are presented. At first, homogeneous glass combinations are welded. Due to their different material parameters the required processing parameters for the successful bonding differ from the parameters used for fused silica. The second part deals with the welding of dissimilar glass combinations and the analysis of the resulting molten material. Finally the welding of glass to different materials as silicon is presented, followed by some application examples of the laser bonding technique.

6.1 Homogeneous glass combinations

6.1.1 Borofloat 33

Borosilicate glass has a much lower softening point than fused silica (see Table 2.1). In addition, the thermal conductivity is lower, leading to an increased heat affected zone and accordingly a larger molten volume, while using the same processing parameters as for fused silica. Furthermore, Borosilicate exhibits a viscosity which is about 6 orders of magnitude lower than fused silica (e.g. at 1600 °C fused silica has a viscosity of about $5 \cdot 10^8 \text{ Pa} \cdot \text{s}$ whereas Borosilicate glass has a viscosity of about $10^2 \text{ Pa} \cdot \text{s}$) [145]. Thus, during the resolidification possible distortions (e.g. voids or laser induced disruptions) can be balanced and induced stress can partially relax [166].

A front view on the laser induced welds in Borofloat 33 is shown in Figure 6.1 (a). Here, a repetition rate of 4.7 MHz, pulse energy of 200 nJ (translation velocity of 200 mm/min) and focusing depth of 1 mm was used. The width is more than 50 μm which is much larger than in fused silica (see Figure 2.5). In addition, no dark spots (disruptions) are formed. Cvecek et al. measured the shear strength of laser bonded borosilicate glass which was about 25 % of the bulk material [29]. Figure 6.1 (b) shows the breaking strength measured with a three point bending test with respect to the line separation of the welding seams for

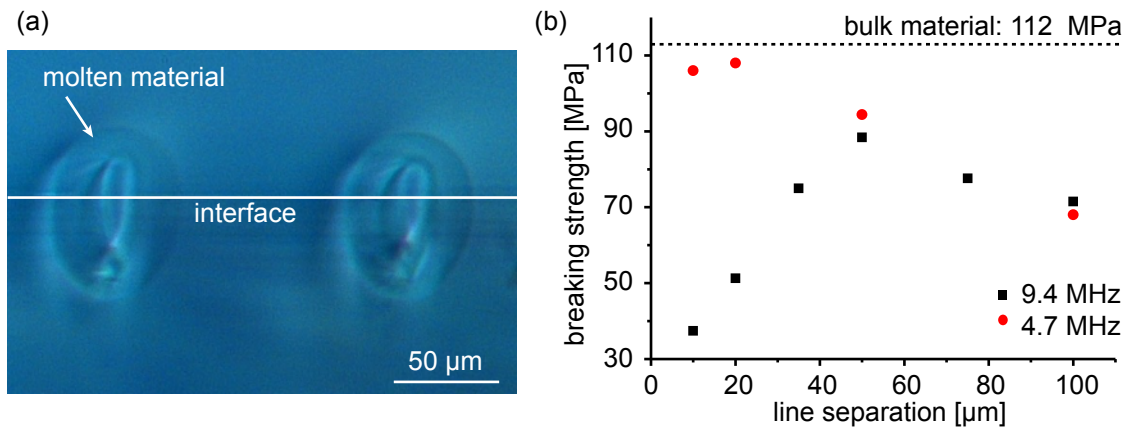


Fig. 6.1: (a) Front view on laser welded Borofloat 33. (b) Breaking strength of Borofloat with respect to the line separation for different repetition rates. The pulse energy was 200 nJ. The error of the measured breaking strength is about 15 %.

two different repetition rates. In general, with decreasing line separation a larger fraction of the interface is molten and the breaking strength of the welded samples increases up to an optimal value yielding the maximal breaking strength. However, for a line separation smaller than the optimal value the breaking strength decreases again. This effect is due to the induced stress fields which overlap if the line separation is small enough reducing the stability of the bonded samples. As the width of the welding seams and the induced stress are determined by the repetition rate of the laser the optimal line separation depends also on the repetition rate, see Figure 6.1 (b). When using a line separation of 20 μm while using a repetition rate of 4.7 MHz the highest breaking strength of 108 MPa is obtained. This is about 95 % of the bulk material (113 MPa) and thus the highest stability value achieved for laser bonded borosilicate glass.

6.1.2 BK7

Another borosilicate glass is BK7 which exhibits a relative large thermal expansion coefficient α of $7.1 \cdot 10^{-6} \text{ K}^{-1}$ (α of Borofloat 33 is $3.25 \cdot 10^{-6} \text{ K}^{-1}$). The high thermal expansion coefficient leads to intense stress within the material if the glass temperature increases locally. Thus, multiple cracks are formed within the glass during the laser welding process. Although it was possible to weld some individual samples exhibiting a breaking strength higher than the solely optically contacted samples, a reliable measurement for the welding of pure BK7 samples was not possible.

6.1.3 ULE

One great advantage of ULE glass is the low thermal expansion coefficient (see Table 2.1). Softening point and thermal conductivity of ULE are comparable to fused silica. However, the welding of ULE shows a completely different dependence of the laser parameters as the glasses presented so far. For all applied laser parameters a darkening of the sample was observed. After the irradiation with ultrashort laser pulses the modified ULE glass exhibits an enhanced absorption over the entire visible spectral range, see Figure 6.2 (a). This darkening increases with the pulse energy applied. For the absorption curves shown in Figure 6.2 (a) a line pattern was structured (see inset) with a repetition rate of 4.7 MHz and a line separation of $10\ \mu\text{m}$ (translation velocity of $1\ \text{mm}/\text{min}$). The darkening of the sample can also be seen in the microscope image of the inset of Figure 6.2 (a).

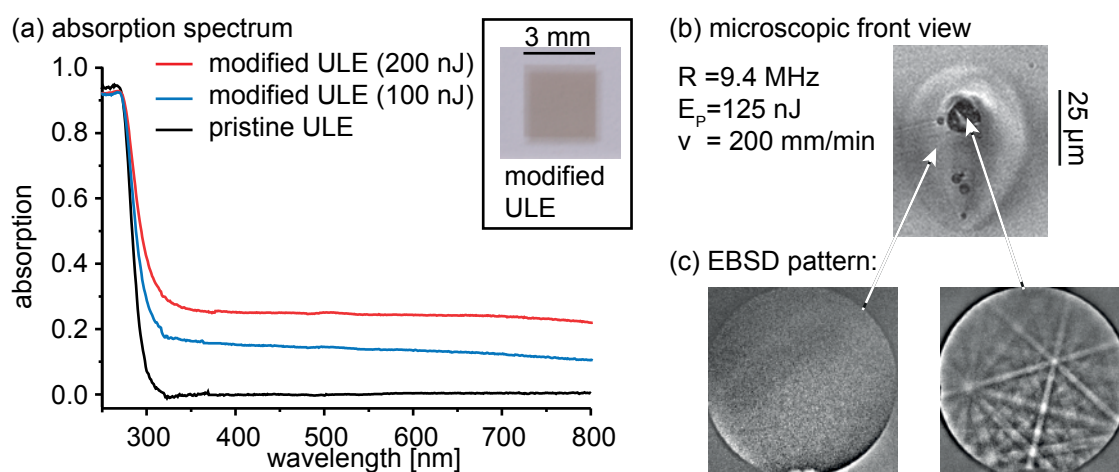


Fig. 6.2: (a) Absorption spectra of modified ULE for different processing pulse energies. As reference, the absorption spectrum of pristine ULE is shown, too. (b) Front view on the laser induced modification. (c) EBSD pattern of the indicated areas within the modified volume.

The darkening of the sample is due to the high TiO_2 concentration of the ULE glass. A change of the oxidation state from Ti^{4+} to Ti^{3+} is well known to induce a darkening, e.g. during the electrochemically induced nucleation of mullite [167] in glass melts or the laser-induced darkening in thermoplastic elastomers with TiO_2 additives [168]. The reduction of TiO_2 occurs at temperatures above $1500\ ^\circ\text{C}$ and thus also during the laser welding process [114]. To confirm the presence of different oxygen-titanium-compounds the laser modified sample was analyzed by Electron Backscattering Diffraction (EBSD)

[169]. The front view of the laser induced welding seam presented in Figure 6.2 (b) shows that the black coloration is actually localized in dots within the heat affected material. These dots seem to be temperature induced pointing towards laser induced crystallization [170, 171]. The EBSD pattern of these dots shows a crystalline pattern, which can be indexed as trigonal Ti_2O_3 , see Figure 6.2 (c). The surrounding material shows no significant EBSD pattern as expected for an amorphous material. Interestingly, not all structures provide an EBSD-pattern allowing distinct indexing. This may be caused by a disturbed crystal lattices (stress, residual glass, partial crystallization) or clusters of nm-scale crystals instead of a single crystal. Independent from the indexing procedure the acquisition of any EBSD-pattern proves the presence of a diffracting lattice and hence confirms laser induced crystallization in these samples. The crystallization is accompanied by a volume contraction leading to the formation of pores and stress around the crystal.

In accordance to that, with increased darkening of the sample a decreasing breaking strength was measured. Thus, stable bonding of ULE samples is only possible using low pulse energies. Figure 6.3 shows the measured breaking strength with respect to the relative fraction of molten interface of laser bonded ULE using different average laser powers. Here, the translation velocity was 200 mm/min. When using a pulse energy of 150 nJ and a repetition rate of 9.4 MHz (not shown) the processed samples were almost completely dark and no bonding was achieved. For a repetition rate of 3.1 MHz (black line Figure 6.3) the breaking strength achieved was about 10 MPa due to the only weak heat accumula-

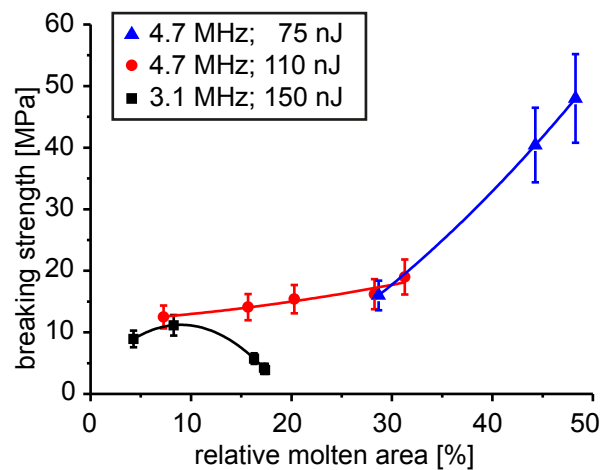


Fig. 6.3: Breaking strength of ULE in dependence on the relative molten area for different laser parameters. The lines are a guide to the eye.

tion. The highest breaking strength was obtained for repetition rates of 4.7 MHz. Using a relatively low pulse energy of 75 nJ a maximal breaking strength of 50 MPa was obtained (see blue curve in Figure 6.3) which is about 55 % of the ULE bulk material (90 MPa). Here, isolated welding spots were used. Darkening of the sample hindered any further increase of the molten area and higher breaking strengths.

6.1.4 Zerodur

Another material with a very low thermal expansion coefficient of below 10^{-9} K^{-1} is the glass-ceramic Zerodur. To achieve the low thermal expansion coefficient the positive thermal expansion of the glassy phase of Zerodur is balanced by a negative thermal expansion of an additional crystalline phase. Although the material properties (softening point, thermal conductivity, etc.) of Zerodur are comparable to the other glasses under investigation, the achieved breaking strengths are below 20 MPa, which is only about 11 % of the bulk material. Here, the translation velocity was a crucial processing parameter. The accessible breaking strength increases with increasing translation velocity and the best results were obtained for a translation velocity of 1000 mm/min. A possible explanation for the low breaking strength is the large Young's modulus of Zerodur. Hence Zerodur is stiffer than the other glasses and the laser induced heating leads to multiple cracks reducing the stability of the laser processed material.

6.2 Bonding of dissimilar glasses

In a next step, various glass combinations were joined. Most common bonding techniques are not able to bond different materials, due to their dissimilar thermal expansion coefficients. This is especially true for techniques working with an additional annealing step. In contrast, the localized heating induced by ultrashort laser pulses offers a great advantage as the induced thermal load is minimal. However, the processing parameters with respect to the material properties determine the size of the molten material. Consequently, the dimensions of the laser induced modification can change directly at the interface. This can be seen in Figure 6.4 showing the front view of welded glass combinations. For all the experiments, the laser focus was placed underneath the interface of the samples as the initial position of the laser focus always poses the lowest point of the molten volume.

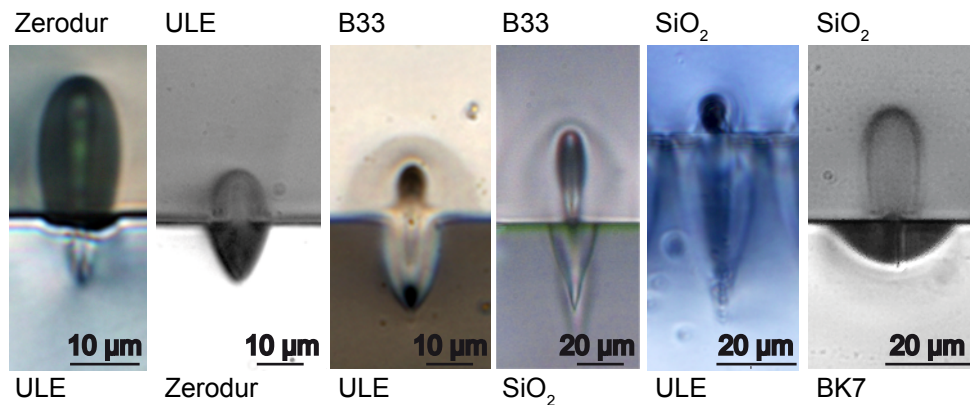


Fig. 6.4: Welding of different glass combinations. Due to the different thermal coefficients the size of the heat affected zones changes at the interface. For all experiments, the focus was placed underneath the interface of the samples. Various processing parameters have been applied.

As the thermal coefficients of ULE and Zerodur are comparable, the widths of the molten material are nearly the same. On the other hand, the welding of the other material combinations shown in Figure 6.4 [e.g. Borofloat 33 (B33) on ULE or Borofloat 33 on fused silica (SiO₂)] shows a huge difference in their melt widths. Fused silica on ULE are both silica glasses with comparable thermal properties. Hence the only difference in their molten material is the formation of a large disruption in the fused silica glass. Fused silica and BK7 exhibit a large difference in thermal conductivity and especially softening point. Consequently, the width of the molten material within BK7 is much larger than in fused silica. Interestingly, this combination shows no hints of a formed disruption within the molten fused silica glass. This might be due to the formation of a new glass structure within the modified area, consisting of both glasses. Bonding of BK7 on fused silica was also demonstrated by Hélie et al. while using filaments of ultrashort laser pulses [94].

The challenge for the successful bonding of dissimilar glasses is to choose processing parameters which are adapted to both materials. Figure 6.5 shows the dependence of the breaking strength on the line separation for different material combinations. In accordance to the results obtained for homogeneous material combinations an optimal value of the line separation exists. This optimal line separation is determined by the amount of molten material versus the induction of stress. For all experiments, the optimal line separation was between 5 μm and 20 μm. For most material combinations (colored triangles in Figure 6.5) the optimal repetition rate was 4.7 MHz. In most cases, the application of a higher repetition rate results in the formation of cracks within the samples and lower

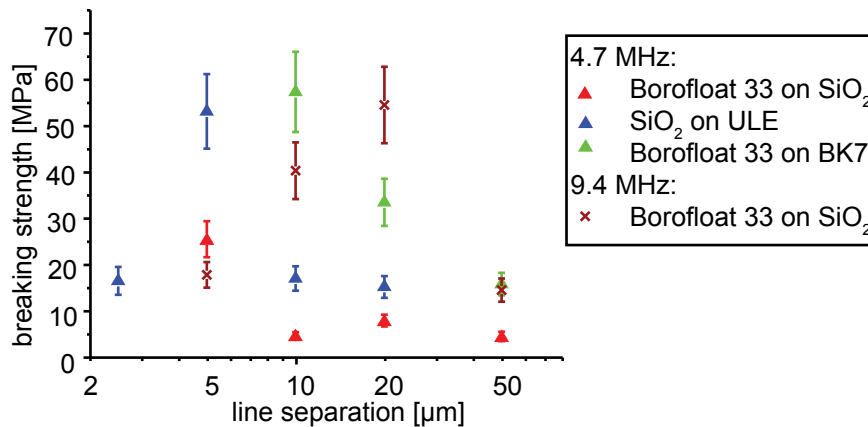


Fig. 6.5: Breaking strength with respect to the line separation for different material combinations.

repetition rates yield only a small amount of molten material.

Figure 6.6 summarizes the obtained bonding results for different glasses and glass combinations. The gray bars indicate the measured breaking strength of the bulk material. The blue bars in front of them show the maximal achieved breaking strength for homogeneous material combinations and the orange ones reflect the maximal breaking strength after welding the respective glass combinations. The results obtained for the bonding of different glasses are comparable to the results of the homogeneous material combinations. For

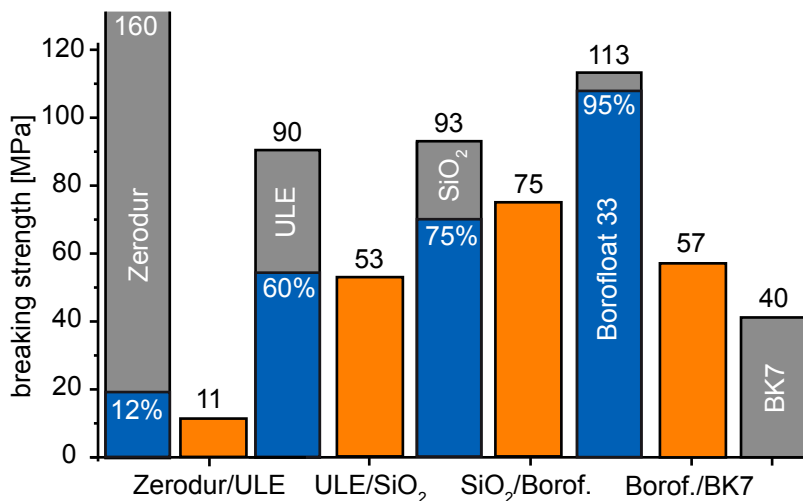


Fig. 6.6: Bonding results of the glasses and glass combinations investigated. The gray bars indicate the breaking strength of the unmodified bulk materials. The blue bars represent the maximal breaking results of homogeneous material combinations. The orange bars show the maximal bonding results of different material combinations.

example, the combination of fused silica with ULE yields a breaking strength of 53 MPa which is almost the same value achieved for the bonding of ULE samples (54 MPa). Interestingly, it was possible to bond Borofloat 33 on BK7. The combination of these glasses results in a higher breaking strength (up to 57 MPa) than the breaking strength of the BK7 bulk material (40 MPa). A microscopic inspection of the fractured samples showed that the initial crack propagation started within the original interface of Borosilicate and BK7 but continued within the BK7 bulk material. This indicates that solely the molten interface exhibits higher breaking strength as the pristine BK7. This might be due to the new composition of the solidified material containing both glasses, BK7 and Borofloat 33.

6.2.1 Structural analysis

In the following, the composition of a laser bonded region is analyzed by Raman spectroscopy. To this end, the bond interface of ULE and Zerodur was investigated as both glasses exhibit different Raman features. The Raman spectra of pristine and modified ULE (blue lines) and Zerodur (red lines) are shown in Figure 6.7. For the laser modification of Zerodur and ULE the same laser parameters as for the laser bonding were used but only the individual bulk material was modified. In addition, a Raman spectrum of the

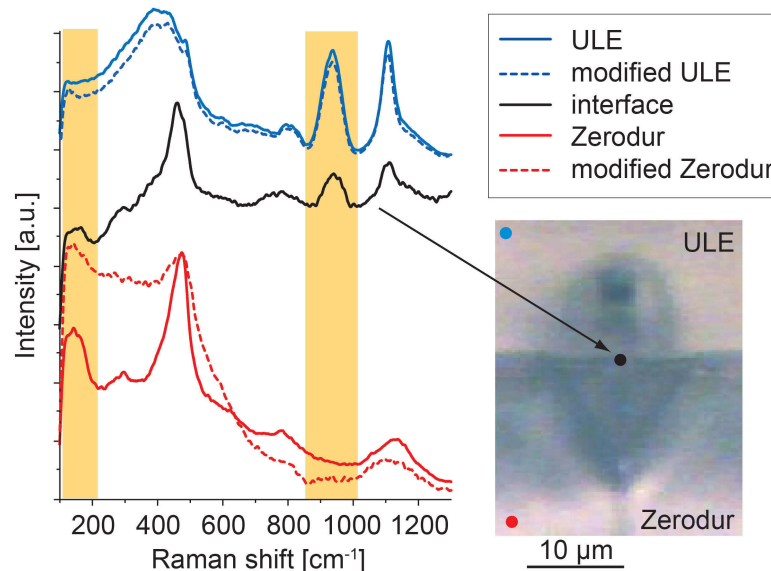


Fig. 6.7: Raman spectra of pristine and laser modified Zerodur and ULE. In addition, a spectrum originating from the welding seam is shown. The microscope image illustrate the different origins of the spectra.

welded interface (black line) is shown. The origin of the Raman spectra of the unmodified glass and the weld can be seen in the microscope image on the right of Figure 6.7. The spectra are shifted against each other to highlight their differences. Some characteristic silica features - due to bending and stretching modes of the fundamental Si-O-Si linkage [83, 84] - appear also in the Raman spectra of ULE and Zerodur. The spectral ranges at which the glasses exhibit individual features are highlighted by yellow color. ULE shows a distinct peak at 934 cm^{-1} due to an asymmetric Ti-O-Si stretching mode [172, 173]. The second prominent peak at 1110 cm^{-1} is assigned to an Si-O⁻ stretching mode (Q³ silicon tetraheda) [83, 174]. The spectrum of Zerodur shows individual features at 143 cm^{-1} and 297 cm^{-1} induced by the AlO₃ content and a disordered crystalline phase of anatase and solid solution of TiO₂-Al₂O₃ with anosovite structure [166, 175]. The laser treatment of Zerodur increases its Raman signal between 100 cm^{-1} and 500 cm^{-1} whereas laser treated ULE depicts only marginal changes. However, the characteristic features of ULE and Zerodur still exist and no additional Raman peaks were induced by the laser treatment. The Raman spectrum originating from the welding seams shows distinct features of both glasses. Within this spectrum a low peak at 143 cm^{-1} appears and additionally a peak at 934 cm^{-1} can be found indicating a new glass composition as a result of the melting and subsequent diffusion of the glasses.

To investigate the composition of the entire weld, the whole front view of the modification [Figure 6.8 (a)] was mapped and the Raman signal recorded. Afterwards, the Raman signal was analyzed considering only the characteristic features (yellow colored spectral

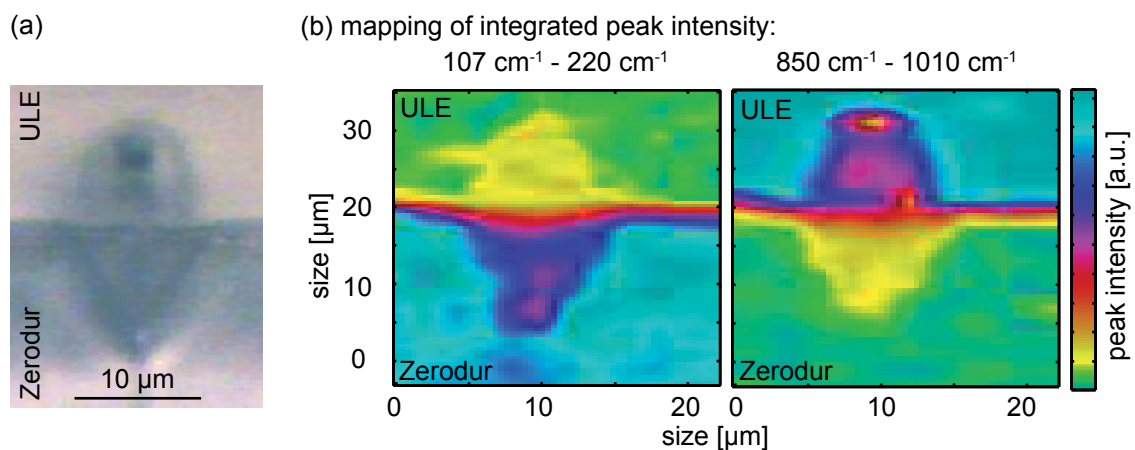


Fig. 6.8: (a) Microscope image of laser welded Zerodur /ULE combination. (b) mapping of the integrated Raman spectra within the glass specific ranges, as indicated in 6.7.

ranges of Figure 6.7) of ULE and Zerodur, respectively. For the left part of Figure 6.8 (b) the baseline subtracted spectra between 107 cm^{-1} and 220 cm^{-1} were integrated. Within this spectral area Zerodur shows a large Raman response while pure ULE exhibits no Raman signal (see Figure 6.7). Thus, unmodified Zerodur yields the highest intensity (cyan) whereas unmodified ULE shows almost no intensity (green). The shape of the laser induced modification can be clearly identified and agrees to the shape of the microscope image. The modified material depicts a reduction of the integrated peak intensity from the Zerodur towards ULE showing a transition of the Zerodur into the ULE glass during the melting of the material. The same analysis was done for the characteristic ULE peak between 850 cm^{-1} and 1010 cm^{-1} . Here, ULE shows the highest intensity whereas Zerodur is devoid of any signal. Again the entire modified area shows a transition from a low signal (within Zerodur) to a high signal (within ULE). The laser modified ULE area shows a lower Raman signal than the pure ULE due to a reduction of the Raman band at $\sim 850\text{ cm}^{-1}$ under heat treatment, as reported by Dymshits et al. [173]. In addition, a drop of the peak intensity can be seen at the upper part of ULE. The microscope image [Figure 6.8 (a)] shows also a faint dark spot within this area which is most likely a disruption. This distorts and reduces the Raman signal.

The results of the Raman analysis have shown that the bonding of different glasses using ultrashort laser pulses induces new compositions of the parent materials. By the generation of new material compositions breaking stabilities are achieved comparable to the individual welded glasses. Thus, localized laser bonding is a powerful technique to bond even different materials.

6.2.2 Annealing

The stability of laser bonded glasses can be enhanced by annealing. However, annealing is only possible for materials with almost the same thermal expansion coefficient. Fused silica and ULE exhibit each a very low thermal expansion coefficient (see Table 2.1). Thus, the annealing of laser bonded fused silica/ULE is possible. Figure 6.9 shows the breaking strengths obtained for different annealing temperatures. Each annealing temperature was kept for 2 hours, whereas heating and cooling rate was 100 K/h .

Here, processing parameters were chosen at which the laser bonded (non-annealed) material exhibits a breaking strength of only 20 MPa . However, the breaking strength increases with increasing annealing temperature. Annealing to $800\text{ }^{\circ}\text{C}$ yields a breaking strength of

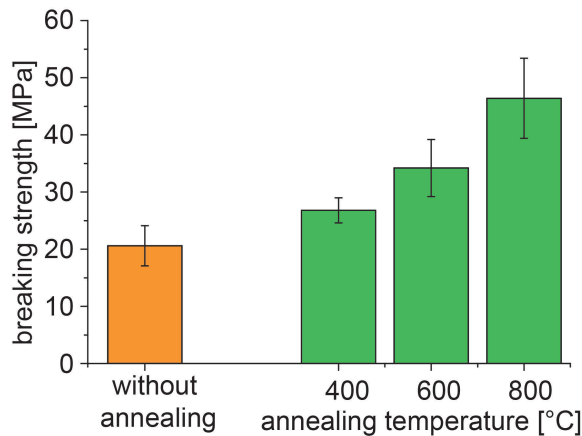


Fig. 6.9: Breaking strength of laser welded ULE/fused silica without and with an post-processing annealing step.

46 MPa which is more than twice the value of the non-annealed samples. Thus, it is possible to strengthen the laser induced welds, even for inhomogeneous material combinations, if the mismatch between the thermal expansion coefficients of the bonded materials is small. The possibility to strengthen the stability of already laser welded samples is especially important if processing parameters were chosen which yield not the maximal accessible breaking strength, e.g. only a few welding seams were inscribed to enhance the transparency of the welded sample.

6.3 Bonding of opaque materials

Finally the technique of laser induced heat accumulation was used to demonstrate the bonding of transparent on opaque materials. To this end, BK7 was bonded on silicon. A first study of the processing parameters has shown that the laser focus has to be placed directly at the interface of the two optically contacted samples. Using a repetition rate of 9.4 MHz always induced cracks in BK7. In addition, pulse energies of above 150 nJ lead to damage, too. Thus, the final samples were bonded at a repetition rate of 3.1 MHz and a pulse energy of 130 nJ (450 fs, 515 nm, 0.5 NA). For the processing wavelength of 515 nm silicon is opaque, i. e. linear absorption dominates. However, also a large amount of BK7 is modified as can be seen in the microscope image of Figure 6.10. The dashed line retraces the molten material in BK7 showing the typical shape of laser induced mod-

ification in glass. In addition, the surface of silicon was molten and is extended into the BK7 glass.

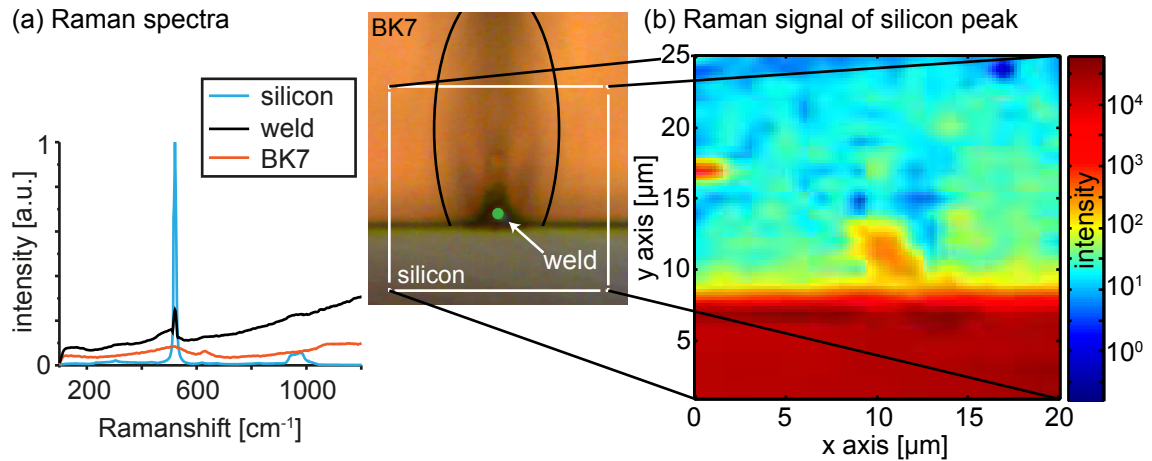


Fig. 6.10: (a) Raman spectra of pure silicon and BK7. The Raman signal of the molten region is shown, too. The microscope image shows the bonding area between silicon and BK7. The dashed line retraces the heat affected zone in BK7. (b) Map of the Raman signal of the silicon peak (at 520 cm^{-1}) of the entire modified area.

To illustrate this, Raman mapping of the welded interface was conducted. Figure 6.10 (a) shows the Raman spectra of BK7 (red line) and silicon (blue line). The typical silicon Raman peak at 520 cm^{-1} - due to the Si-Si bonds - and the second order of the silicon peak between 920 cm^{-1} and 1000 cm^{-1} can be seen. For the Raman spectrum of BK7 the signal was accumulated 10 times. Here, the typical features of borosilicate glass were observed [83]. The spectrum recorded within the dark modified area (indicated by a green point in the microscope image) shows the silicon Raman peak, too. The increasing Raman signal for higher wavenumbers is due to fluorescence of the material. Figure 6.10 (b) shows a mapping of the silicon Raman peak over the entire modified area. It can be seen that solely the silicon diffuses into the laser treated BK7 glass. No evidence was found that some glassy material is embedded within the silicon. Thus, the bonding mechanism is different from the bonding of two transparent materials where the melts of the materials are mixed.

Figure 6.11 shows the surface of a BK7 sample which was bonded to silicon and subsequently ripped off. In addition, the intensity of the silicon Raman peak is plotted, too. The remnants of the welding seams can be seen in both images. The Raman measurement (right image) shows that the welding seams consist mainly of silicon whereas no mate-

rial was ripped off the BK7 sample. From Figure 6.10 and Figure 6.11 one can conclude that the silicon serves as adhesive between the two samples. Due to the linear absorption of silicon at first the silicon is molten followed by a diffusion of the molten silicon into the BK7. The heat treatment of silicon distorts the crystal structure reducing its stability. Thus, a fracture of the sample destroys the welding seams which consist of silicon.

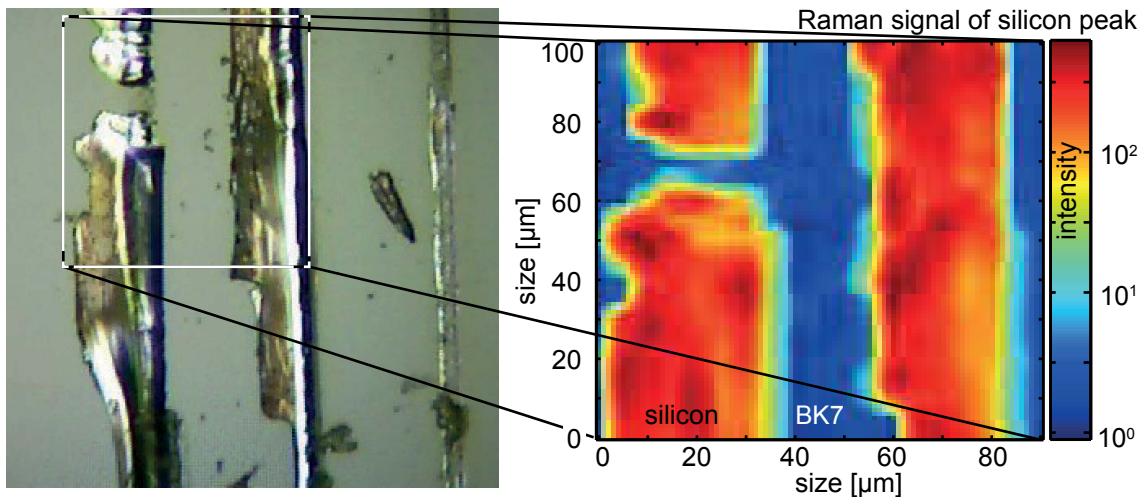


Fig. 6.11: Remnants of silicon atop a BK7 sample. After the laser bonding the samples were ripped apart. The Raman mapping of the silicon peak (right image) shows that the welds consist mainly of silicon.

Ultrashort laser pulses can also be used to bond metals on glasses. Ozeki et al. and Utsumi et al. bonded successfully copper on glass, whereas with the application of fs pulses the required pulse energy could be reduced by two orders of magnitude compared to ns pulses [95, 103]. In addition, a precisely control of the welded region was possible while using fs pulses [95].

6.4 Application examples

As shown in the previous chapters laser bonding of transparent materials is a powerful tool to realize stable bonds between different materials. The potential applications are numerous. In this section few applications of laser bonding are briefly highlighted. Laser induced welds are continuous lines of molten material. Thus, these welds are gas and especially water proof. This can be used to encapsulate optical devices. Figure 6.12 (a) shows an optical grating. Here a thin glass-coverplate was bonded to the substrate to avoid

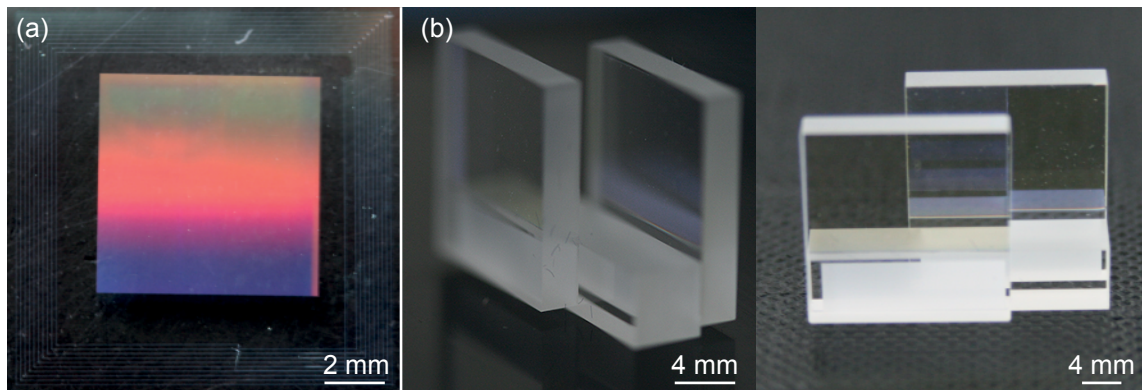


Fig. 6.12: (a) Encapsulation of a grating for Surface Enhanced Raman Spectroscopy. (b) Bonding in a distinct area of fused silica samples to realize a high quality Fabry-Perot Etalon.

contamination of the grating.

The device presented in Figure 6.12 (b) is a Fabry-Parrot Etalon. For the bonding of the samples an adhesive can not be used as it would change the distance between the glass plates and thus distort the resonance frequency of the Etalon. Other bonding methods as annealing or surface activation are not suited as only the lower part of the samples has to be joined. Annealing of the entire sample would distort the coating of the sample. Instead laser induced bonding can be used to bond the lower part of the samples and realize strong bonds.

One disadvantage of laser induced bonding is the local reduction of the transmission of the glass at the position of the welding seams. Experiments showed that the transmission through the welding seams can slightly improved by a post processing annealing step. However, the laser welding itself can solve this problem. With a position system only some parts of an optical device (e. g. a lens) can be bonded while leaving the rest of the device unattached. Thus, optical devices can be joined at their outer edges whereas the central part remains unchanged and its transmission is unaffected of the entire bonding process.

Laser induced bonding can also be utilized in combination with conventional bonding techniques to strengthen the bonds or to protect former non bonded parts. Figure 6.13 (a) shows two large plasma bonded fused silica samples. The interface is not completely bonded as indicated by the interference pattern. This is a serious problem for large samples and due to the imperfections at the edge of the samples. Such a non-bonded part allows the fracture of the entire bonded sample as liquids and dirt can impinge into the

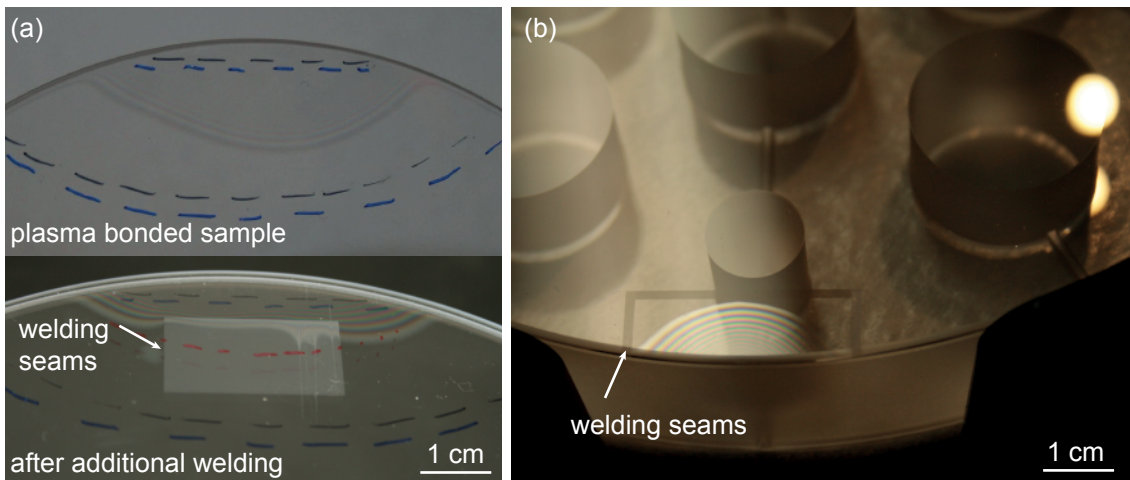


Fig. 6.13: (a) Plasma bonded samples with a non-bonded part. After the inscription of additional welds the interference fringes are reduced and a fracture of the entire sample prevented. (b) Welding seams seal the non-bonded part of plasma bonded ULE samples.

interface. In the lower picture of Figure 6.13 (a) a homogeneous pattern of welding lines was inscribed in the same sample. These welds serve as additional bonds and protect the entire sample. In addition, the non-bonded area is reduced as the welds pull the samples slightly together. Consequently, the number of interference rings is reduced. The red dashed line indicates the theoretical envelope of the interference rings without additional welding seams. In addition, non-bonded parts can directly be encircled by the inscription of additional welding seams. This prevents a fracture of the entire sample. Figure 6.13 (b) shows plasma bonded ULE samples. Defects at the lower edge lead to a non-bonded area (interference pattern), which was additionally protected by laser induced welding seams. These brief descriptions of potential applications are just some first examples of the universal application potential of laser bonding using ultrashort laser pulses at high repetition rates. Due to the high accessible breaking strength strong and reliable bonds are obtained between the samples giving the opportunity to bond only a certain fraction of the samples or even dissimilar materials.

7 Conclusion and Outlook

The development of novel ultrashort pulse laser systems revolutionized the processing of transparent materials in the last years. Numerous techniques were designed to structure transparent materials (e. g. glasses) even directly within the pristine bulk material. In contrast, the stable and reliable bonding of different transparent materials is still a demanding problem [1, 2]. Numerous techniques were copied by silicon wafer techniques, whereas none of them were designed for transparent materials leading to multiple disadvantages. Thus, new methods are required to achieve high bonding strengths and to bond even different materials. To reduce the amount of induced stress the processing should be at room temperature and no interface layer should be used to avoid possible aging of the bond. In principle, ultrashort laser pulses are capable to solve all these issues [30]. Their extremely short pulse duration facilitates non-linear absorption processes leading to extremely non-equilibrium states in the processed region [5, 6]. If the time between the laser pulses is shorter than the heat diffusion time within the material, the temperature of the processed area increases stepwise and so-called heat accumulation occurs [21]. Under these circumstances the laser acts as thermal point source allowing to locally melt the material within a well defined vicinity of the laser focus [21, 22]. With a positioning system the thermal point source can be moved arbitrary enabling the possibility to bond two transparent samples by the local melting of their interface [30].

The principle capability to induce local melting by ultrashort laser pulses at high repetition rates was shown by Schaffer et al. [21]. In addition, the welding of transparent materials using ultrashort laser pulses was first presented in 2005 [23]. However, the fundamental physical properties of the laser bonding mechanism were not analyzed. Furthermore, there are no comprehensive investigations about the achievable bonding stabilities. In addition, the testing setups used so far were not suited to compare the stability of laser bonded samples with values of the pristine bulk material.

Within the frame of this thesis, the physical principles of the briefly described laser bonding technique were investigated. The results presented here, give new insights in the fun-

damental interaction process of transparent materials with ultrashort laser pulses at high repetition rates. At first the absorption process of ultrashort laser pulses at high repetition rates was analyzed. It was shown that the cumulative action of laser pulses is mediated by different mechanisms. Within several hundred picoseconds after the laser excitation, Self Trapped Excitations (STEs) enhance the absorption of the subsequent pulse. The STEs decay within several hundred picoseconds amongst others into dangling-bond-type defects increasing the absorption within the modified area. In general, the permanent defects are an integral part of the laser induced modification as they correspond to a densification of the irradiated material. Raman measurements of the heat treated zone yield an increase of the 3- and 4-fold silicon-oxygen rings leading to a decreasing overall bond angle and a densification of the glass. An exact analysis of the respective peak positions and widths indicate that predominantly planar 3-fold rings are formed. In addition, IR-reflection measurements show an increase of the fictive temperature of the modified glass of ≈ 700 K induced by the laser heating and the subsequent rapid quenching of the glass which is much faster than in any conventional glass production process.

Absorption of multiple laser pulses lead to heating of the material. Although several theoretical approaches exist to simulate the laser induced temperature distribution [22, 176] no reliable experimental measurements of the ultrashort pulse induced heat accumulation and subsequent heat diffusion were obtained so far. Within this work, the spatial and temporal temperature distribution induced by ultrashort pulse at high repetition rates was measured directly, for the first time. To this end, an *in-situ* micro Raman setup was developed. The results indicate a critical influence of the pulse energy on the induced temperature. In borosilicate glass, the maximal temperature directly after the excitation (pulse energy $1.1 \mu\text{J}$, repetition rate of 1 MHz) is about 7000 K and rapidly cools down within several hundreds of ns. A theoretical model developed confirms the experimental results and predicts the size of the molten material. While assuming an elliptical heat source and a temperature depending diffusivity the simulations are in very good accordance to the experimental results.

In addition, the formation of disruptions occurring in molten fused silica could be explained here. The internal structure of these disruptions were imaged for the first time. These disruptions consist of a foam-like inner structure with cavities ranging from a few hundreds of nm up to $2 \mu\text{m}$. The formation of a disruption can be explained as a result of an interruption of the laser heating process leading to a rapid quenching of the material. For continuous irradiation this interruption is caused by aberrations induced by the re-

fractive index change of the molten material. These aberrations reduce the energy density within the laser focus until the absorption stops. Simulations of the intensity in the laser focus after passing a temperature induced index modification confirm this model. Disruptions appear periodically for focusing close to the surface and high pulse energies. The largest distance between periodic disruptions is obtained when using high pulse energies and high repetition rates.

Another issue were the induced stress fields surrounding the laser induced welds. These stress fields increase with increasing applied laser power while an entire relaxation of the stress field is prevented by the quenching of the material. With an additional annealing step the induced stress could be significantly reduced. A complete relaxation of the laser induced stress in borosilicate glass was obtained after annealing to 600 °C, whereas at this temperature the stress in fused silica was reduced by only 50 %. This difference can be explained by the different annealing points of the glasses.

The implementation of the results obtained allowed the successful bonding of various glasses. The stability of the laser induced bonds were determined with a three point bending test as well as with a Chevron Notch test. Both testing setups were applied for the first time at laser bonded glass samples and indicated that the laser welding technique alter the surrounding material reducing its stability. Thus, the laser induced welding seams exhibit higher breaking strengths than the surrounding material. In fused silica a breaking strength of up to 75 % of the pristine bulk material was obtained while inscribing isolated welding spots. This high value is in good agreement with the breaking strength of the bulk material after the same modifications were induced. One way to increase the stability of laser bonded glass is thermal annealing. However, annealing of the entire sample poses a high thermal load for the sample and complicates prospective applications. Thus, another approach was chosen using a tailored energy deposition and reducing the induced stress to increase the breaking strength. As shown here, with bursts of ultrashort laser pulses very high breaking strengths can be achieved. The application of laser bursts instead of temporally equally distributed pulses lead to elongated modifications changing the shape of the induced stress distribution. In addition, when using laser bursts a bonding regime with relatively low average power can be chosen reducing the overall induced stress. Using these two advantages, up to 96 % of the breaking strength of the bulk material was obtained. This is the highest value of laser bonded transparent materials reported so far. With direct laser bonding numerous glasses and even glass combinations can be joined, whereas the achieved breaking strength depends on the glass. For example, for borosili-

cate glass a breaking strength of up to 95 % of the bulk material was obtained. In contrast, the bonding of the zero expansion glass ceramic ULE is accompanied with a crystallization process giving rise to the formation of Ti_2O_3 microcrystals within the processed material. The breaking strengths when bonding different glass combinations are comparable to the results of homogeneous material combinations. Raman spectroscopy was used to prove, that the bonding of different glasses result in novel kinds of glasses. With ultra-short laser pulses it is also possible to bond transparent to opaque materials as shown in this thesis for BK7 and silicon. Here, predominantly silicon acts as welding seam establishing strong bonds between the materials.

Due to the accessible high breaking strengths direct laser bonding is a powerful technique for multiple applications. Some are demonstrated in this thesis, e. g. the encapsulation of optical devices. In addition, laser induced bonding can also be utilized in combination with conventional bonding techniques to strengthen the bonds or to encase defects.

To date, the main limitation of laser bonding is the required optical contacting. Thus, the next principle challenge is to bond samples without optical contacting or pressing them together. To this end, a scanner system could be used to melt the non-contacted surfaces simultaneously. Another demanding issue is the bonding of crystals. Their high thermal conductivities and melting points complicate laser induced heat accumulation. However, the bonding to a glass substrate should be possible. Thus, crystals could be bonded to glass substrates providing the welding material.

Taking a broader perspective, research in the ultrashort pulse - matter interaction will also influence other fields of research. Due to the extremely non equilibrium states of the processed material high temperatures and large pressures are accessible resulting in local modifications which could not be realized so far. The possibility to induce a defined temperature within a volume of only a few μm^3 results in highly excited material states. Thus, the investigation of localized plasma states becomes feasible.

In addition, by tailoring the energy deposition of multiple laser pulses even graded structures with large dimensions can be realized. As it was shown here, for certain glasses laser induced heat accumulation can induce crystallization within the processed material resulting in very small crystals embedded in an amorphous material. Local modifications within a pristine host material exhibit outstanding properties for numerous applications. Thus, novel photonics or data storage devices on a micrometer scale or even smaller can be realized by the same technique as presented in this thesis.

Bibliography

- [1] U. Gösele and Q.-Y. Tong. Semiconductor wafer bonding. *Annu. Rev. Mater. Sci.*, 28(1):215–241, 1998.
- [2] J. Haisma and G. A. C. M. Spierings. Contact bonding, including direct-bonding in a historical and recent context of materials science and technology, physics and chemistry: historical review in a broader scope and comparative outlook. *Mater. Sci. Eng., R*, 37(1):1–60, 2002.
- [3] A. Berthold, L. Nicola, P. M. Sarro, and M. J. Vellekoop. Glass-to-glass anodic bonding with standard IC technology thin films as intermediate layers. *Sens. Actuators, A*, 82(1):224–228, 2000.
- [4] B. Goss. Bonding glass and other substrates with UV curing adhesives. *Int. J. Adhes. Adhes.*, 22(5):405–408, 2002.
- [5] K. Itoh, W. Watanabe, S. Nolte, and C. B. Schaffer. Ultrafast processes for bulk modification of transparent materials. *MRS Bull.*, 31(08):620–625, 2006.
- [6] R. R. Gattass and E. Mazur. Femtosecond laser micromachining in transparent materials. *Nature Photonics*, 2(4):219–225, 2008.
- [7] M. Ams, G. D. Marshall, and M. J. Withford. Study of the influence of femtosecond laser polarisation on direct writing of waveguides. *Opt. Express*, 14(26):13158–13163, 2006.
- [8] K. M. Davis, K. Miura, N. Sugimoto, and K. Hirao. Writing waveguides in glass with a femtosecond laser. *Opt. Lett.*, 21(21):1729–1731, 1996.
- [9] P. G. Kazansky, H. Inouye, T. Mitsuyu, K. Miura, J. Qiu, K. Hirao, and F. Starrost. Anomalous anisotropic light scattering in ge-doped silica glass. *Phys. Rev. Lett.*, 82(10):2199–2202, 1999.
- [10] Y. Shimotsuma, P. G. Kazansky, J. Qiu, and K. Hirao. Self-organized nanogratings in glass irradiated by ultrashort light pulses. *Phys. Rev. Lett.*, 91(24):247405, 2003.
- [11] R. R. Gattass, L. R. Cerami, and E. Mazur. Micromachining of bulk glass with bursts of femtosecond laser pulses at variable repetition rates. *Opt. Express*, 14(12):5279–5284, 2006.

- [12] S. Juodkazis, H. Misawa, T. Hashimoto, E. G. Gamaly, and B. Luther-Davies. Laser-induced microexplosion confined in a bulk of silica: Formation of nanovoids. *Appl. Phys. Lett.*, 88(20):201909–201909, 2006.
- [13] R. Keil, M. Heinrich, F. Dreisow, T. Pertsch, A. Tünnermann, S. Nolte, D. N. Christodoulides, and A. Szameit. All-optical routing and switching for three-dimensional photonic circuitry. *Scientific reports*, 1:1–6, 2011.
- [14] A. Szameit and S. Nolte. Discrete optics in femtosecond-laser-written photonic structures. *J. Phys. B: At., Mol. Opt. Phys.*, 43(16):163001, 2010.
- [15] M. Heinrich, R. Keil, F. Dreisow, A. Tünnermann, A. Szameit, and S. Nolte. Non-linear discrete optics in femtosecond laser-written photonic lattices. *Appl. Phys. B*, 104(3):469–480, 2011.
- [16] J. R. Grenier, L. A. Fernandes, and P. R. Herman. Femtosecond laser writing of optical edge filters in fused silica optical waveguides. *Opt. Express*, 21(4):4493–4502, 2013.
- [17] L. P. R. Ramirez, M. Heinrich, S. Richter, F. Dreisow, R. Keil, A. V. Korovin, U. Peschel, S. Nolte, and A. Tünnermann. Tuning the structural properties of femtosecond-laser-induced nanogratings. *Appl. Phys. A*, 100(1):1–6, 2010.
- [18] M. Beresna, M. Gecevicius, P. G. Kazansky, and T. Gertus. Radially polarized optical vortex converter created by femtosecond laser nanostructuring of glass. *Appl. Phys. Lett.*, 98(20):201101–201101, 2011.
- [19] C. Hnatovsky, R. S. Taylor, E. Simova, V. R. Bhardwaj, D. M. Rayner, and P. B. Corkum. Polarization-selective etching in femtosecond laser-assisted microfluidic channel fabrication in fused silica. *Opt. Lett.*, 30(14):1867–1869, 2005.
- [20] W. Watanabe, T. Toma, K. Yamada, J. Nishii, K.-I. Hayashi, and K. Itoh. Optical seizing and merging of voids in silica glass with infrared femtosecond laser pulses. *Opt. Lett.*, 25(22):1669–1671, 2000.
- [21] C. B. Schaffer, J. F. García, and E. Mazur. Bulk heating of transparent materials using a high-repetition-rate femtosecond laser. *Appl. Phys. A*, 76(3):351–354, 2003.
- [22] S. M. Eaton, H. Zhang, M. L. Ng, J. Li, W.-J. Chen, S. Ho, and P. R. Herman. Transition from thermal diffusion to heat accumulation in high repetition rate femtosecond laser writing of buried optical waveguides. *Opt. Express*, 16(13):9443–9458, 2008.
- [23] T. Tamaki, W. Watanabe, J. Nishii, and K. Itoh. Welding of transparent materials using femtosecond laser pulses. *J. J. Appl. Phys.*, 44(20/23):687–689, 2005.

- [24] T. Tamaki, W. Watanabe, and K. Itoh. Laser micro-welding of transparent materials by a localized heat accumulation effect using a femtosecond fiber laser at 1558 nm. *Opt. Express*, 14(22):10460–10468, 2006.
- [25] I. Miyamoto, K. Cvecek, and M. Schmidt. Evaluation of nonlinear absorptivity in internal modification of bulk glass by ultrashort laser pulses. *Opt. Express*, 19(11):10714–10727, 2011.
- [26] M. Sakakura, M. Shimizu, Y. Shimotsuma, K. Miura, and K. Hirao. Temperature distribution and modification mechanism inside glass with heat accumulation during 250 kHz irradiation of femtosecond laser pulses. *Appl. Phys. Lett.*, 93(23):231112–231112, 2008.
- [27] M. Shimizu, M. Sakakura, M. Ohnishi, M. Yamaji, Y. Shimotsuma, K. Hirao, and K. Miura. Three-dimensional temperature distribution and modification mechanism in glass during ultrafast laser irradiation at high repetition rates. *Opt. Express*, 20(2):934–940, 2012.
- [28] W. P. Maszara, G. Goetz, A. Caviglia, and J. B. McKitterick. Bonding of silicon wafers for silicon-on-insulator. *J. Appl. Phys.*, 64:4943, 1988.
- [29] K. Cvecek, I. Miyamoto, J. Strauss, V. Bui, S. Scharfenberg, T. Frick, and M. Schmidt. Strength of joining seams in glass welded by ultra-fast lasers depending on focus height. *J. Laser Micro/Nanoeng.*, 7(1):68–72, 2012.
- [30] K. Itoh and T. Tamaki. Ultrafast laser microwelding for transparent and heterogeneous materials. In *Lasers and Applications in Science and Engineering*, page 68810V. International Society for Optics and Photonics, 2008.
- [31] I. Miyamoto, A. Horn, J. Gottmann, D. Wortmann, and F. Yoshino. Fusion welding of glass using femtosecond laser pulses with high-repetition rates. *J. Laser Micro/Nanoeng.*, 60(3-4):59–66, 2011.
- [32] K. Eda, A. Kanaboshi, T. Ogura, and Y. Taguchi. Direct bonding of quartz crystal onto silicon. *J. Appl. Phys.*, 74(7):4801–4802, 1993.
- [33] Y. Okamoto, I. Miyamoto, K. Cvecek, A. Okada, K. Takahashi, and M. Schmidt. Evaluation of molten zone in micro-welding of glass by picosecond pulsed laser. *J. Laser Micro/Nanoeng.*, 8:65–69, 2013.
- [34] A. Horn, I. Mingareev, A. Werth, M. Kachel, and U. Brenk. Investigations on ultrafast welding of glass–glass and glass–silicon. *Appl. Phys. A*, 93(1):171–175, 2008.
- [35] L. Skuja, M. Hirano, H. Hosono, and K. Kajihara. Defects in oxide glasses. *phys. status solidi (c)*, 2(1):15–24, 2005.

- [36] W. H. Zachariasen. The atomic arrangement in glass. *J. Am. Chem. Soc.*, 54(10):3841–3851, 1932.
- [37] A. Pasquarello and R. Car. Identification of raman defect lines as signatures of ring structures in vitreous silica. *Phys. Rev. Lett.*, 80(23):5145, 1998.
- [38] J.W. Chan, T.R. Huser, S.H. Risbud, and D.M. Krol. Modification of the fused silica glass network associated with waveguide fabrication using femtosecond laser pulses. *Appl. Phys. A*, 76(3):367–372, 2003.
- [39] H. Nishikawa, E. Watanabe, D. Ito, and Y. Ohki. Decay kinetics of the 4.4-eV photoluminescence associated with the two states of oxygen-deficient-type defect in amorphous SiO₂. *Phys. Rev. Lett.*, 72(13):2101, 1994.
- [40] K. Kajihara, L. Skuja, M. Hirano, and H. Hosono. Formation and decay of non-bridging oxygen hole centers in SiO₂ glasses induced by F2 laser irradiation: In situ observation using a pump and probe technique. *Appl. Phys. Lett.*, 79:1757, 2001.
- [41] J. E. Shelby. *Introduction to glass science and technology*. Royal Society of Chemistry, 2005.
- [42] A. Q. Tool. Relation between inelastic deformability and thermal expansion of glass in its annealing range. *J. Am. Ceram. Soc.*, 29(9):240–253, 1946.
- [43] A. E. Geissberger and F. L. Galeener. Raman studies of vitreous SiO₂ versus fictive temperature. *Physical Review B*, 28(6):3266, 1983.
- [44] F. L. Galeener. Raman and ESR studies of the thermal history of amorphous SiO₂. *J. Non-Cryst. Solids*, 71(1):373–386, 1985.
- [45] J. W. Chan, T. R. Huser, S. H. Risbud, J. S. Hayden, and D. M. Krol. Waveguide fabrication in phosphate glasses using femtosecond laser pulses. *Appl. Phys. Lett.*, 82(15):2371–2373, 2003.
- [46] H. W. Hoeness, R. Mueller, E. W. Rodeck, and F. B. Siebers. Spin-cast zerodur mirror substrates of the 8 m class and lightweight substrates for secondary mirrors. *Astrophysics and Space Science*, 160(1-2):193–197, 1989.
- [47] S. T. Gulati and M. J. Edwards. ULE(TM)-Zero Expansion, low density, and dimensionally stable material for lightweight optical systems. In *Proceedings of Advanced Materials for Optics and Precision Structures*, pages 107–136, 1997.
- [48] <http://www.corning.com>. access on 20.03.2013.
- [49] <http://www.schott.com>. access on 20.08.2012.

-
- [50] I. Mingareev. *Ultrafast dynamics of melting and ablation at large laser intensities*. PhD thesis, Universitätsbibliothek, 2009.
- [51] N. W. Ashcroft and N. D. Mermin. *Solid State Physics*. Harcourt College Publishers, 1976.
- [52] C. B Schaffer, A. Brodeur, and E. Mazur. Laser-induced breakdown and damage in bulk transparent materials induced by tightly focused femtosecond laser pulses. *Meas. Sci. Technol.*, 12(11):1784, 2001.
- [53] B. C. Stuart, M. D. Feit, S. Herman, A. M. Rubenchik, B.W. Shore, and M. D. Perry. Nanosecond-to-femtosecond laser-induced breakdown in dielectrics. *Physical Review B*, 53(4):1749, 1996.
- [54] M. Lenzner, J. Krüger, S. Sartania, Z. Cheng, C. Spielmann, G. Mourou, W. Kautek, and F. Krausz. Femtosecond optical breakdown in dielectrics. *Phys. Rev. Lett.*, 80(18):4076, 1998.
- [55] L. V. Keldysh. Diagram technique for nonequilibrium processes. *Sov. Phys. JETP*, 20(4):1018–1026, 1965.
- [56] A. Kaiser, B. Rethfeld, M. Vicanek, and G. Simon. Microscopic processes in dielectrics under irradiation by subpicosecond laser pulses. *Physical Review B*, 61(17):11437, 2000.
- [57] D. Du, X. Liu, G. Korn, J. Squier, and G. Mourou. Laser-induced breakdown by impact ionization in SiO₂ with pulse widths from 7 ns to 150 fs. *Appl. Phys. Lett.*, 64(23):3071–3073, 1994.
- [58] C. Hnatovsky, R.S. Taylor, P.P. Rajeev, E. Simova, V.R. Bhardwaj, D.M. Rayner, and P.B. Corkum. Pulse duration dependence of femtosecond-laser-fabricated nanogratings in fused silica. *Appl. Phys. Lett.*, 87(1):014104–014104, 2005.
- [59] B. Poumellec, M. Lancry, A. Chahid-Erraji, and P. G. Kazansky. Modification thresholds in femtosecond laser processing of pure silica: review of dependencies on laser parameters. *Opt. Mater. Express*, 1(4):766–782, 2011.
- [60] F. L. Galeener. Planar rings in vitreous silica. *J. Non-Cryst. Solids*, 49(1):53–62, 1982.
- [61] R Brückner. Properties and structure of vitreous silica. i. *J. Non-Cryst. Solids*, 5(2):123–175, 1970.
- [62] R. Brückner. Properties and structure of vitreous silica. ii. *J. Non-Cryst. Solids*, 5(3):177–216, 1971.

- [63] M. Will, S. Nolte, B. N. Chichkov, and A. Tünnermann. Optical properties of waveguides fabricated in fused silica by femtosecond laser pulses. *Appl. Opt.*, 41(21):4360–4364, 2002.
- [64] D. M. Krol. Femtosecond laser modification of glass. *J. Non-Cryst. Solids*, 354(2):416–424, 2008.
- [65] L. Sudrie, M. Franco, B. Prade, and A. Mysyrowicz. Study of damage in fused silica induced by ultra-short IR laser pulses. *Opt. Commun.*, 191(3):333–339, 2001.
- [66] J. D. Mills, P. G. Kazansky, E. Bricchi, and J. J. Baumberg. Embedded anisotropic microreflectors by femtosecond-laser nanomachining. *Appl. Phys. Lett.*, 81(2):196–198, 2002.
- [67] E. Bricchi, J. D. Mills, P. G. Kazansky, B. G. Klappauf, and J. J. Baumberg. Birefringent fresnel zone plates in silica fabricated by femtosecond laser machining. *Opt. Lett.*, 27(24):2200–2202, 2002.
- [68] R. Taylor, C. Hnatovsky, and E. Simova. Applications of femtosecond laser induced self-organized planar nanocracks inside fused silica glass. *Laser & Photonics Reviews*, 2(1-2):26–46, 2008.
- [69] C. Hnatovsky, R. S. Taylor, E. Simova, P. P. Rajeev, D. M. Rayner, V. R. Bhardwaj, and P. B. Corkum. Fabrication of microchannels in glass using focused femtosecond laser radiation and selective chemical etching. *Appl. Phys. A*, 84(1-2):47–61, 2006.
- [70] W. Cai, A. R. Libertun, and R. Piestun. Polarization selective computer-generated holograms realized in glass by femtosecond laser induced nanogratings. *Opt. Express*, 14(9):3785–3791, 2006.
- [71] W. Yang, E. Bricchi, P. G. Kazansky, J. Bovatsek, and A. Y. Arai. Self-assembled periodic sub-wavelength structures by femtosecond laser direct writing. *Opt. Express*, 14(21):10117–10124, 2006.
- [72] V. R. Bhardwaj, E. Simova, P. P. Rajeev, C. Hnatovsky, R. S. Taylor, D. M. Rayner, and P. B. Corkum. Optically produced arrays of planar nanostructures inside fused silica. *Phys. Rev. Lett.*, 96(5):057404, 2006.
- [73] P. G. Kazansky and Y. Shimotsuma. Self-assembled sub-wavelength structures and form birefringence created by femtosecond laser writing in glass: properties and applications. *J. Ceram. Soc. Jpn.*, 116(1358):1052–1062, 2008.
- [74] G. Petite, P. Daguzan, S. Guizard, and P. Martin. Conduction electrons in wide-bandgap oxides: a subpicosecond time-resolved optical study. *Nucl. Instrum. Methods Phys. Res., Sect. B*, 107(1):97–101, 1996.

-
- [75] P. Martin, S. Guizard, P. Daguzan, G. Petite, P. d'Oliveira, P. Meynadier, and M. Perdrix. Subpicosecond study of carrier trapping dynamics in wide-band-gap crystals. *Physical Review B*, 55(9):5799, 1997.
- [76] S. Richter, M. Heinrich, S. Döring, A. Tünnermann, and S. Nolte. Formation of femtosecond laser-induced nanogratings at high repetition rates. *Appl. Phys. A*, 104(2):503–507, 2011.
- [77] D. Grojo, M. Gertsvolf, H. Jean-Ruel, S. Lei, L. Ramunno, D. M. Rayner, and P. B. Corkum. Self-controlled formation of microlenses by optical breakdown inside wide-band-gap materials. *Appl. Phys. Lett.*, 93(24):243118–243118, 2008.
- [78] C. Hnatovsky, E. Simova, P. P. Rajeev, D. M. Rayner, P. B. Corkum, and R. S. Taylor. Femtosecond laser writing of porous capillaries inside fused silica glass. *Opt. Lett.*, 32(11):1459–1461, 2007.
- [79] E. N. Glezer, M. Milosavljevic, M. Huang, R. J. Finlay, T.-H. Her, J. P. Callan, and E. Mazur. Three-dimensional optical storage inside transparent materials. *Opt. Lett.*, 21(24):2023–2025, 1996.
- [80] E. N. Glezer and E. Mazur. Ultrafast-laser driven micro-explosions in transparent materials. *Appl. Phys. Lett.*, 71(7):882–884, 1997.
- [81] C. B. Schaffer, A. O. Jamison, and E. Mazur. Morphology of femtosecond laser-induced structural changes in bulk transparent materials. *Appl. Phys. Lett.*, 84(9):1441–1443, 2004.
- [82] E. G. Gamaly, S. Juodkazis, K. Nishimura, H. Misawa, B. Luther-Davies, L. Hallo, P. Nicolai, and V. T. Tikhonchuk. Laser-matter interaction in the bulk of a transparent solid: Confined microexplosion and void formation. *Physical Review B*, 73(21):214101, 2006.
- [83] D. J. Little, M. Ams, S. Gross, P. Dekker, C. T. Miese, A. Fuerbach, and M. J. Withford. Structural changes in BK7 glass upon exposure to femtosecond laser pulses. *J. Raman Spectrosc.*, 42(4):715–718, 2011.
- [84] P. Colomban, A. Tournie, and L. Bellot-Gurlet. Raman identification of glassy silicates used in ceramics, glass and jewellery: a tentative differentiation guide. *J. Raman Spectrosc.*, 37(8):841–852, 2006.
- [85] S. K. Sharma, J. F. Mammone, and M. F. Nicol. Raman investigation of ring configurations in vitreous silica. *Nature*, 292:140–141, 1981.
- [86] J. W. Chan, T. Huser, S. Risbud, and D. M. Krol. Structural changes in fused silica after exposure to focused femtosecond laser pulses. *Opt. Lett.*, 26(21):1726–1728, 2001.

- [87] W. Reichman, J. W. Chan, and D. M. Krol. Confocal fluorescence and raman microscopy of femtosecond laser-modified fused silica. *J. Phys.: Condens. Matter*, 15(31):S2447, 2003.
- [88] J. H. Stathis and M. A. Kastner. Time-resolved photoluminescence in amorphous silicon dioxide. *Physical Review B*, 35(6):2972, 1987.
- [89] H. S. Carslaw, J. C. Jaeger, and H. Feshbach. Conduction of heat in solids. *Physics Today*, 15:74, 1962.
- [90] S. Eaton, H. Zhang, P. Herman, F. Yoshino, L. Shah, J. Bovatsek, and A. Arai. Heat accumulation effects in femtosecond laser-written waveguides with variable repetition rate. *Opt. Express*, 13(12):4708–4716, 2005.
- [91] S. Nolte, M. Will, J. Burghoff, and A. Tünnermann. Ultrafast laser processing: New options for three-dimensional photonic structures. *J. Mod. Opt.*, 51(16):2533–2542, 2004.
- [92] W. Watanabe, S. Onda, T. Tamaki, K. Itoh, and J. Nishii. Space-selective laser joining of dissimilar transparent materials using femtosecond laser pulses. *Appl. Phys. Lett.*, 89:021106, 2006.
- [93] S. Richter, S. Döring, A. Tünnermann, and S. Nolte. Bonding of glass with femtosecond laser pulses at high repetition rates. *Appl. Phys. A*, 103(2):257–261, 2011.
- [94] D. Hélie, M. Bégin, F. Lacroix, and R. Vallée. Reinforced direct bonding of optical materials by femtosecond laser welding. *Appl. Opt.*, 51(12):2098–2106, 2012.
- [95] Y. Ozeki, T. Inoue, T. Tamaki, H. Yamaguchi, S. Onda, W. Watanabe, T. Sano, S. Nishiuchi, A. Hirose, and K. Itoh. Direct welding between copper and glass substrates with femtosecond laser pulses. *Appl. Phys. Express*, 1(8):082601, 2008.
- [96] M. Shimbo, K. Furukawa, K. Fukuda, and K. Tanzawa. Silicon-to-silicon direct bonding method. *J. Appl. Phys.*, 60(8):2987–2989, 1986.
- [97] E. M. Liston. Plasma treatment for improved bonding: a review. *The Journal of Adhesion*, 30(1-4):199–218, 1989.
- [98] M. Petzold, H. Knoll, and J. Bagdahn. Strength assessment of wafer-bonded micromechanical components using the micro-chevron test. In *Micromachining and Microfabrication*, pages 133–142. International Society for Optics and Photonics, 2001.
- [99] C. Dresbach, A. Krombholz, M. Ebert, and J. Bagdahn. Mechanical properties of glass frit bonded micro packages. *Microsystem Tech.*, 12(5):473–480, 2006.

-
- [100] H. Y. Wang, R. S. Foote, S. C. Jacobson, J. H. Schneibel, and J. M. Ramsey. Low temperature bonding for microfabrication of chemical analysis devices. *Sens. Actuators, B*, 45(3):199–207, 1997.
- [101] G. Kalkowski, M. Rohde, S. Risse, R. Eberhardt, and A. Tünnermann. Direct bonding of glass substrates. *ECS Transactions*, 33(4):349–355, 2010.
- [102] S. Richter, S. Döring, F. Zimmermann, L. Lescieux, R. Eberhardt, S. Nolte, and A. Tünnermann. Welding of transparent materials with ultrashort laser pulses. In *Proc. SPIE*, volume 8244, page 824402, 2012.
- [103] A. Utsumi, T. Ooie, T. Yano, and M. Katsumura. Direct bonding of glass and metal using short pulsed laser. *J. Laser Micro/Nanoeng.*, 2(2):133–136, 2007.
- [104] C. Luo and L. Lin. The application of nanosecond-pulsed laser welding technology in MEMS packaging with a shadow mask. *Sens. Actuators, A*, 97:398–404, 2002.
- [105] F. Sari, M. Wiemer, M. Bernasch, and J. Bagdahn. Laser transmission bonding of silicon-to-silicon and silicon-to-glass for wafer level packaging and microsystems. *ECS Transactions*, 16(8):561–568, 2008.
- [106] A. Wissinger, A. Olowinsky, A. Gillner, and R. Poprawe. Laser transmission bonding of silicon to silicon with metallic interlayers for wafer-level packaging. *Microsystem Tech.*, 19:1–5, 2013.
- [107] C. W. Carr, H. B. Radousky, A. M. Rubenchik, M. D. Feit, and S. G. Demos. Localized dynamics during laser-induced damage in optical materials. *Phys. Rev. Lett.*, 92(8):087401, 2004.
- [108] M. Sakakura, M. Terazima, Y. Shimotsuma, K. Miura, and K. Hirao. Heating and rapid cooling of bulk glass after photoexcitation by a focused femtosecond laser pulse. *Opt. Express*, 15(25):16800–16807, 2007.
- [109] C. H. Lin, Z. H. Rao, L. Jiang, W. J. Tsai, P. H. Wu, C. W. Chien, and H. L. Tsai. Enhancement of ablation efficiency by a femto/nano-second dual-beam micromachining system. In *LASE*, pages 75850I–75850I. International Society for Optics and Photonics, 2010.
- [110] A. P. Kanavin, I. V. Smetanin, V. A. Isakov, Y. V. Afanasiev, B. N. Chichkov, B. Wellegehausen, S. Nolte, C. Momma, and A. Tünnermann. Heat transport in metals irradiated by ultrashort laser pulses. *Physical Review B*, 57(23):14698, 1998.
- [111] H. D. Baehr and K. Stephan. *Wärme-und Stoffübertragung*. Springer DE, 2008.

- [112] VDI Gesellschaft Verfahrenstechnik und Chemieingenieurwesen (GVC). Wärmearbeitsatlas, VDI. Springer, 2006. 10. Auflage.
- [113] S. Eaton. *Contrast in thermal diffusion and heat accumulation effects in the fabrication of waveguides in glasses using variable repetition rate Femtosecond laser*. PhD thesis, University of Toronto, 2008.
- [114] T. Yoshino, Y. Ozeki, M. Matsumoto, and K. Itoh. In situ micro-Raman investigation of spatio-temporal evolution of heat in ultrafast laser microprocessing of glass. *J. Appl. Phys.*, 51(10):2403, 2012.
- [115] I. Miyamoto, A. Horn, and J. Gottmann. Local melting of glass material and its application to direct fusion welding by ps-laser pulses. *J. Laser Micro/Nanoeng.*, 2(7):7–14, 2007.
- [116] J. M. Branlund and A. M. Hofmeister. Factors affecting heat transfer in natural SiO₂ solids. *Am. Mineral.*, 93(10):1620–1629, 2008.
- [117] K. Cvecek, I. Miyamoto, J. Strauss, M. Wolf, T. Frick, and M. Schmidt. Sample preparation method for glass welding by ultrashort laser pulses yields higher seam strength. *Appl. Opt.*, 50(13):1941–1944, 2011.
- [118] M. Sakakura, M. Terazima, Y. Shimotsuma, K. Miura, and K. Hirao. Observation of pressure wave generated by focusing a femtosecond laser pulse inside a glass. *Opt. Express*, 15(9):5674–5686, 2007.
- [119] T. Yoshino, M. Matsumoto, Y. Ozeki, and K. Itoh. Energy-dependent temperature dynamics in femtosecond laser microprocessing clarified by Raman temperature measurement. In *SPIE MOEMS-MEMS*, page 82491D. International Society for Optics and Photonics, 2012.
- [120] D. A. Long. *The Raman Effect: A unified treatment of the theory of Raman Scattering by molecules*. Wiley Online Library, 2002.
- [121] N. B. Colthup, L. H. Daly, and S. E. Wiberley. *Introduction to infrared and Raman spectroscopy*. Academic press, 1990.
- [122] A. Hertwig, S. Martin, J. Krüger, and W. Kautek. Surface damage and color centers generated by femtosecond pulses in borosilicate glass and silica. *Appl. Phys. A*, 79(4-6):1075–1077, 2004.
- [123] J. Du, J. Wu, L. Zhao, and L. Song. Color centers of a borosilicate glass induced by 10 MeV proton, 1.85 MeV electron and ⁶⁰Co- γ ray. *Radiat. Phys. Chem.*, 86:59–63, 2013.

- [124] W. J. Reichman, D. M. Krol, L. Shah, F. Yoshino, A. Arai, S. M. Eaton, and P. R. Herman. A spectroscopic comparison of femtosecond-laser-modified fused silica using kilohertz and megahertz laser systems. *J. Appl. Phys.*, 99(12):123112–123112, 2006.
- [125] J. J. Witcher, W. J. Reichman, L. B. Fletcher, N. W. Troy, and D. M. Krol. Thermal annealing of femtosecond laser written structures in silica glass. *Opt. Mater. Express*, 3(4):502–510, 2013.
- [126] M. Shimizu, M. Sakakura, M. Ohnishi, Y. Shimotsuma, T. Nakaya, K. Miura, and K. Hirao. Mechanism of heat-modification inside a glass after irradiation with high-repetition rate femtosecond laser pulses. *J. Appl. Phys.*, 108(7):073533–073533, 2010.
- [127] F. Hashimoto, S. Richter, S. Nolte, Y. Ozeki, and K. Itoh. Time-resolved micro-Raman measurement of temperature dynamics during high-repetition-rate ultrafast laser microprocessing. In *Proceedings of LAMP 2013*, 2013.
- [128] P. P. Rajeev, M. Gertsvolf, E. Simova, C. Hnatovsky, R. S. Taylor, V. R. Bhardwaj, D. M. Rayner, and P. B. Corkum. Memory in nonlinear ionization of transparent solids. *Phys. Rev. Lett.*, 97(25):253001, 2006.
- [129] S. Richter, C. Miese, S. Döring, F. Zimmermann, M. J. Withford, A. Tünnermann, and S. Nolte. Laser induced nanogratings beyond fused silica-periodic nanostructures in borosilicate glasses and ULE. *Opt. Mater. Express*, 3(8):1161–1166, 2013.
- [130] P. Yang, G. R. Burns, J. Guo, T. S. Luk, and G. A. Vawter. Femtosecond laser-pulse-induced birefringence in optically isotropic glass. *J. Appl. Phys.*, 95(10):5280–5283, 2004.
- [131] S. Richter, F. Jia, M. Heinrich, S. Döring, U. Peschel, A. Tünnermann, and S. Nolte. The role of self-trapped excitons and defects in the formation of nanogratings in fused silica. *Opt. Lett.*, 37(4):482–484, 2012.
- [132] D. Wortmann, M. Ramme, and J. Gottmann. Refractive index modification using fs-laser double pulses. *Opt. Express*, 15(16):10149–10153, 2007.
- [133] R. T. Williams and K. S. Song. The self-trapped exciton. *J. Phys. Chem. Solids*, 51(7):679–716, 1990.
- [134] S. S. Mao, F. Quéré, S. Guizard, X. Mao, R. E. Russo, G. Petite, and P. Martin. Dynamics of femtosecond laser interactions with dielectrics. *Appl. Phys. A*, 79(7):1695–1709, 2004.

- [135] N. Itoh, T. Shimizu-Iwayama, and T. Fujita. Excitons in crystalline and amorphous SiO₂ formation, relaxation and conversion to Frenkel pairs. *J. Non-Cryst. Solids*, 179:194–201, 1994.
- [136] T. E. Tsai, D. L. Griscom, and E. J. Friebele. Mechanism of Intrinsic Si E'-Center Photogeneration in High-Purity Silica. *Phys. Rev. Lett.*, 61(4):444, 1988.
- [137] Y. Shimotsuma, M. Sakakura, P. G. Kazansky, M. Beresna, J. Qiu, K. Miura, and K. Hirao. Ultrafast manipulation of self-assembled form birefringence in glass. *Adv. Mater.*, 22(36):4039–4043, 2010.
- [138] J. W. Chan, T. Huser, J. S. Hayden, S. H. Risbud, and D. M. Krol. Fluorescence spectroscopy of color centers generated in phosphate glasses after exposure to femtosecond laser pulses. *J. Am. Ceram. Soc.*, 85(5):1037–1040, 2002.
- [139] A. Agarwal and M. Tomozawa. Correlation of silica glass properties with the infrared spectra. *J. Non-Cryst. Solids*, 209(1):166–174, 1997.
- [140] Y. Bellouard and M. O. Hongler. Femtosecond-laser generation of self-organized bubble patterns in fused silica. *Opt. Express*, 19(7):6807–6821, 2011.
- [141] R. Graf, A. Fernandez, M. Dubov, H. J. Brueckner, B. N. Chichkov, and A. Apolonski. Pearl-chain waveguides written at megahertz repetition rate. *Appl. Phys. B*, 87(1):21–27, 2007.
- [142] S. Richter, S. Döring, F. Burmeister, F. Zimmermann, A. Tünnermann, and S. Nolte. Formation of periodic disruptions induced by heat accumulation of femtosecond laser pulses. *Opt. Express*, 21(13):15452–15463, 2013.
- [143] S. Spinner and R. M. Waxler. Relation between refractive index and density of glasses resulting from annealing compared with corresponding relation resulting from compression. *Appl. Opt.*, 5(12):1887–1889, 1966.
- [144] B. Pommellec, L. Sudrie, M. Franco, B. Prade, and A. Mysyrowicz. Femtosecond laser irradiation stress induced in pure silica. *Opt. Express*, 11(9):1070–1079, 2003.
- [145] E. B. Shand. *Engineering Glass, Modern Materials, Vol. 6*. Academic Press, New York, 1968.
- [146] Y. Hayasaki, M. Isaka, A. Takita, and S. Juodkazis. Time-resolved interferometry of femtosecond-laser-induced processes under tight focusing and close-to-optical breakdown inside borosilicate glass. *Opt. Express*, 19(7):5725–5734, 2011.
- [147] U. Fuchs, U. Zeitner, and A. Tünnermann. Ultra-short pulse propagation in complex optical systems. *Opt. Express*, 13(10):3852–3861, 2005.

- [148] J. J. Stamnes. *Waves in focal regions: propagation, diffraction, and focusing of light, sound, and water waves*. CRC Press, 1986.
- [149] <http://assets.newport.com/webdocuments-en/images/16000.pdf>. access on 20.01.2013.
- [150] J. W. Goodman and S. C. Gustafson. Introduction to fourier optics. *Opt. Eng.*, 35(5):1513–1513, 1996.
- [151] G. P. Agrawal. *Nonlinear fiber optics*. Springer, 2000.
- [152] W. Primak and D. Post. Photoelastic constants of vitreous silica and its elastic coefficient of refractive index. *J. Appl. Phys.*, 30(5):779–788, 1959.
- [153] L. A. Fernandes, J. R. Grenier, P. R. Herman, J. S. Aitchison, and P. V. S. Marques. Stress induced birefringence tuning in femtosecond laser fabricated waveguides in fused silica. *Opt. Express*, 20(22):24103–24114, 2012.
- [154] A. C. Ferrari, B. Kleinsorge, N. A. Morrison, A. Hart, V. Stolojan, and J. Robertson. Stress reduction and bond stability during thermal annealing of tetrahedral amorphous carbon. *J. Appl. Phys.*, 85(10):7191–7197, 1999.
- [155] D. Helie, F. Lacroix, and R. Vallée. Reinforcing a direct bond between optical materials by filamentation based femtosecond laser welding. *J. Laser Micro/Nanoeng*, 7(9):284–292, 2012.
- [156] S. Wu, D. Wu, J. Xu, Y. Hanada, R. Sukanuma, H. Wang, T. Makimura, K. Sugioka, and K. Midorikawa. Characterization and mechanism of glass microwelding by double-pulse ultrafast laser irradiation. *Opt. Express*, 20(27):28893–28905, 2012.
- [157] R. Demmig. *Repetitorium Technische Mechanik - Band 2 Festigkeitslehre*. Demmig Verlag, 1991.
- [158] A. Marcinkevičius, V. Mizeikis, S. Juodkazis, S. Matsuo, and H. Misawa. Effect of refractive index-mismatch on laser microfabrication in silica glass. *Appl. Phys. A*, 76(2):257–260, 2003.
- [159] S. M. Wiederhorn. Fracture surface energy of glass. *J. Am. Ceram. Soc.*, 52(2):99–105, 1969.
- [160] M. D. Feit and A. M. Rubenchik. Mechanisms of CO₂ laser mitigation of laser damage growth in fused silica. In *XXXIV Annual Symposium on Optical Materials for High Power Lasers: Boulder Damage Symposium*, pages 91–102. International Society for Optics and Photonics, 2003.

- [161] N. Shinkai, R. C. Bradt, and G. E. Rindone. Fracture toughness of fused SiO₂ and float glass at elevated temperatures. *J. Am. Ceram. Soc.*, 64(7):426–430, 1981.
- [162] F. Naumann, S. Brand, M. Bernasch, S. Tismer, P. Czurratis, D. Wünsch, and M. Petzold. Advanced characterization of glass frit bonded micro-chevron-test samples based on scanning acoustic microscopy. *Microsystem Tech.*, 19:1–7, 2013.
- [163] D. Munz, R. T. Bubsey, and J. E. Srawley. Compliance and stress intensity coefficients for short bar specimens with chevron notches. *Int. J. Fracture*, 16(4):359–374, 1980.
- [164] K. R. Brown and F. I. Baratta. *Chevron-notch fracture test experience: metals and non-metals*. Number 1172. Astm International, 1992.
- [165] C. A. Klein. Characteristic strength, weibull modulus, and failure probability of fused silica glass. *Opt. Eng.*, 48(11):113401–113401, 2009.
- [166] L. I. Berezhinsky, V. P. Maslov, B. K. Serdega, V. V. Tetyorkin, and V. A. Yukhymchuk. Study of chemical interaction at Al–Zerodur interface. *J. Eur. Ceram. Soc.*, 26(16):3825–3830, 2006.
- [167] R. Carl, W. Wisniewski, and C. Rüssel. Reactions during Electrochemically Induced Nucleation of Mullite from a MgO/Al₂O₃/TiO₂/SiO₂/B₂O₃/CaO Melt. *Cryst. Growth Des.*, 10(7):3257–3262, 2010.
- [168] H. Zheng and G. C. Lim. Laser-effected darkening in TPEs with TiO₂ additives. *Opt. Las. Eng.*, 41(5):791–800, 2004.
- [169] W. Wisniewski. *Crystal Orientations in GlassCeramics determined using Electron Backscatter Diffraction*. PhD thesis, Friedrich-Schiller-Universität Jena, 2011.
- [170] T. Honma, Y. Benino, T. Fujiwara, and T. Komatsu. Transition metal atom heat processing for writing of crystal lines in glass. *Appl. Phys. Lett.*, 88(23):231105–231105, 2006.
- [171] A. Müller, M. Lorenz, K. Brachwitz, J. Lenzner, K. Mittwoch, W. Skorupa, M. Grundmann, and T. Höche. Fresnoite thin films grown by pulsed laser deposition: photoluminescence and laser crystallization. *Cryst. Eng. Comm.*, 13(21):6377–6385, 2011.
- [172] D. Y. Smith, C. E. Black, C. C. Homes, and E. Shiles. Optical properties of TiO₂–SiO₂ glass over a wide spectral range. *phys. status solidi (c)*, 4(3):838–842, 2007.
- [173] O. S. Dymshits, A. A. Zhilin, V. I. Petrov, M. Y. Tsenter, T. I. Chuvaeva, A. V. Shashkin, V. V. Golubkov, U. Kang, and K. H. Lee. A raman spectroscopic study of phase transformations in titanium-containing magnesium aluminosilicate glasses. *Glass Phys. Chem.*, 28(2):66–78, 2002.

- [174] W. Hutton and J. S. Thorp. The vibrational spectra of MgO-Al₂O₃-SiO₂ glasses containing TiO₂. *J. Mater. Sci.*, 20(2):542–551, 1985.
- [175] T. I. Chuvaeva, O. S. Dymshits, V. I. Petrov, M. Y. Tsenter, A. A. Zhilin, and V. V. Golubkov. Low-frequency Raman scattering and small-angle X-ray scattering of glasses inclined to phase decomposition. *J. Non-Cryst. Solids*, 243(2):244–250, 1999.
- [176] I. Miyamoto, K. Cvecek, Y. Okamoto, M. Schmidt, and H. Helvajian. Characteristics of laser absorption and welding in foruran glass by ultrashort laser pulses. *Opt. Express*, 19(23):22961–22973, 2011.
- [177] S. Richter, F. Zimmermann, S. Döring, A. Tünnermann, and S. Nolte. Ultrashort high repetition rate exposure of dielectric materials: laser bonding of glasses analyzed by micro-Raman spectroscopy. *Appl. Phys. A*, 110(1):9–15, 2013.
- [178] F. Zimmermann, S. Richter, S. Döring, A. Tünnermann, and S. Nolte. Ultrastable bonding of glass with femtosecond laser bursts. *Appl. Opt.*, 52(6):1149–1154, 2013.

Acknowledgements

I would like to express my sincere gratitude towards the people whose support made this work possible.

First of all I have to thank my supervisor Prof. Dr. Andreas Tünnermann, head of the Institute of Applied Physics and the Fraunhofer IOF, Jena for this wonderful topic and the creation of an ambitious atmosphere at the IAP.

I would like to thank the Hans L. Merkle Stiftung for providing me a well covered scholarship, allowing me to spend my research time focused on my scientific topic.

My deepest and sincerest gratitude goes to Prof. Dr. Stefan Nolte, head of the Ultrafast Optics group at the Institute of Applied Physics. This work would not have been possible without his valuable advice and the highly productive environment for research in his group. His critical and pointed questions were always a big support in finishing my ideas and their presentations.

I am very grateful to the people with whom I had the opportunity to cooperate. At first I would like to thank Prof. Dr. Michael Withford from Macquarie University for giving me the opportunity to get new insights into the ultrashort pulse interaction with matter. In addition, I am deeply indebted to Prof. Dr. Kazuyoshi Itoh, Prof. Dr. Yazuyuki Ozeki and Fumiya Hashimoto from the Graduate School of Engineering, Osaka University in Japan for showing me the capabilities of Raman spectroscopy and hosting me in Osaka. My research stays in Sydney and Osaka were a unique possibility to extend my scientific knowledge and personal perception of life.

My long term office colleague Mr. Sven Döring deserves a very big thank for all the fruitful discussions, his experimental patience and his enthusiasm even for the tiniest details of my work. I also like to spend my gratitude to Mr. Felix Zimmermann who gave me the opportunity to pass on what I have learned and supported me on various tasks.

Another "thank-you" goes to the staff at the Institute of Applied Physics and Fraunhofer IOF, in particular Mrs. Christine Otto and Mr. Gilbert Leibelng for the preparation of all the hundreds of glass samples and Mr. Bodo Martin for the care about all the institute's computers and devices.

Special thanks go to Mr. Robert Kammel, Dr. Robert Keil, Dr. Matthias Heinrich, Mr. Frank Burmeister, Mr. Daniel Richter, Mrs. Ria Krämer and all the other colleagues from the ultrafast optics group of the IAP, for their assistance and the ambitious but pleasant atmosphere at the IAP.

I thank my friends Daniel, Bettina, Martin and all my friends of the PPS for helping me freeing my mind and keeping up my morale.

I am very indebted to my parents who have permanently given me great support, endless patience and always supported joyful and relaxing times at home.

Lastly, but most importantly, I would like to thank my wife Jessica. She kept me away from drowning in the work although she always encouraged all my ideas and activities.

Ehrenwörtliche Erklärung

Ich erkläre hiermit ehrenwörtlich, dass ich die vorliegende Arbeit selbständig, ohne unzulässige Hilfe Dritter und ohne Benutzung anderer als der angegebenen Hilfsmittel und Literatur angefertigt habe. Die aus anderen Quellen direkt oder indirekt übernommenen Daten und Konzepte sind unter Angabe der Quellen gekennzeichnet.

Bei der Auswahl und Auswertung des folgenden Materials haben mir die nachstehend aufgeführten Personen in der jeweils beschriebenen Weise unentgeltlich geholfen:

1. Die Raman-Temperaturmessungen in Kapitel 3.2.4 wurden in Zusammenarbeit mit Fumiya Hashimoto, Osaka University, Japan durchgeführt. Herr Hashimoto hat auch das Programm für den Fit der Raman-Messungen geschrieben.
2. Die Simulationen der Intensitätsverteilung im Laserfokus nach Propagation durch eine thermisch-induzierte Brechzahlveränderung in Kapitel 4.4.3 wurden von Frank Burmeister, Fraunhofer IOF Jena durchgeführt.
3. Die Chevron-Notch-Tests und Berechnung der Strukturfunktion in Kapitel 5.6 wurden von Dipl.-Ing. Falk Naumann, Fraunhofer IWM Halle vorgenommen.
4. Die Aufnahme und Analyse der EBSD-Messungen aus Kapitel 6.1.3 wurden von Dr. Wisniewski am OSIM Jena durchgeführt.

Weitere Personen waren an der inhaltlich-materiellen Erstellung der vorliegenden Arbeit nicht beteiligt. Insbesondere habe ich hierfür nicht die entgeltliche Hilfe von Vermittlungs- bzw. Beratungsdiensten (Promotionsberater oder anderen Personen) in Anspruch genommen. Niemand hat von mir unmittelbar oder mittelbar geldwerte Leistungen für Arbeiten erhalten, die im Zusammenhang mit dem Inhalt der vorgelegten Dissertation stehen.

Teile dieser Arbeit wurden aus Prioritätsgründen bereits veröffentlicht oder zur Veröffentlichung eingereicht [93, 76, 131, 177, 142, 129, 178].

Die Arbeit wurde bisher weder im In- noch im Ausland in gleicher oder ähnlicher Form einer anderen Prüfungsbehörde vorgelegt.

Die geltende Promotionsordnung der Physikalisch-Astronomischen Fakultät ist mir bekannt.

Ich versichere ehrenwörtlich, dass ich nach bestem Wissen die reine Wahrheit gesagt und nichts verschwiegen habe.

Jena, den 1. November 2013

Sören Richter

Lebenslauf

Persönliche Daten

Name Sören Richter
Geburtsdatum, -ort 25.01.1983, Magdeburg

Ausbildung

04/2002 Abitur am Wilhelm-Raabe-Gymnasium Magdeburg
07/2002 – 05/2003 Zivildienst Magdeburg
10/2003 – 09/2005 Studium der Physik an der Otto-von-Guericke Universität Magdeburg
10/2005 – 12/2008 Studium der Physik an der Friedrich-Schiller Universität Jena
12/2008 Abschluss des Jenaer Physikstudiums mit dem Diplom

Wissenschaftlicher Werdegang

07/2003 – 10/2003 Forschungspraktikum an der Otto-von-Guericke Universität Magdeburg
10/2006 – 10/2008 Studentische Forschungsaufgaben an der FSU Jena
10/2008 – 12/2008 Diplomarbeit am Institut für Angewandte Physik, FSU Jena
04/2013 – 06/2013 Forschungsaufenthalt an der Macquarie University Sydney, Australien
10/2013 – 12/2013 Forschungsaufenthalt an der Osaka University, Japan
seit 03/2009 Promotion am Institut für Angewandte Physik